

AD-A013 621

TEMPS (TRANSPORTABLE EMP SIMULATOR) FINAL REPORT.  
VOLUME II. APPENDIXES

H. Aslin, et al

Physics International Company

Prepared for:

Defense Nuclear Agency

August 1973

DISTRIBUTED BY:

**NTIS**

National Technical Information Service  
U. S. DEPARTMENT OF COMMERCE

237104

AD

①

FC

PIFR-372-D  
TEMPS FINAL REPORT

ADA013621

Volume II  
Appendixes

by  
H. Aslin and R. Ryan

August 1973

Prepared for  
Harry Diamond Laboratories  
Washington, D.C. 20438  
Under Contract No. DAAK02-72-C-0059

Reproduced by  
NATIONAL TECHNICAL  
INFORMATION SERVICE  
U.S. Department of Commerce  
Springfield VA 22151

Prepared by  
Physics International Company  
2700 Merced Street  
San Leandro, California 94577

DDC  
REFORMED  
DEC 16 1974  
RECEIVED  
E

APPROVED FOR PUBLIC RELEASE; DISTRIBUTION UNLIMITED.

220

SECURITY CLASSIFICATION OF THIS PAGE (When Data Entered)

REPORT DOCUMENTATION PAGE		READ INSTRUCTIONS BEFORE COMPLETING FORM
1. REPORT NUMBER PIFR-372	2. GOVT ACCESSION NO.	3. RECIPIENT'S CATALOG NUMBER
4. TITLE (and Subtitle) TEMPS FINAL REPORT Volume II Appendixes		5. TYPE OF REPORT & PERIOD COVERED DRAFT FINAL 9-1-71 through 10-16-72
		6. PERFORMING ORG. REPORT NUMBER PIFR-372
7. AUTHOR(s) H. Aslin and R. Ryan		8. CONTRACT OR GRANT NUMBER(s) DAAK02-72-C-0059
9. PERFORMING ORGANIZATION NAME AND ADDRESS Physics International Company 2700 Merced Street San Leandro, California 94577		10. PROGRAM ELEMENT, PROJECT, TASK AREA & WORK UNIT NUMBERS P0007
11. CONTROLLING OFFICE NAME AND ADDRESS Defense Nuclear Agency Washington, D. C. 20305		12. REPORT DATE August 1973
		13. NUMBER OF PAGES 220
14. MONITORING AGENCY NAME & ADDRESS (if different from Controlling Office) Harry Diamond Laboratories Washington, D. C. 20438		15. SECURITY CLASS. (of this report) Unclassified
		15a. DECLASSIFICATION/DOWNGRADING SCHEDULE
16. DISTRIBUTION STATEMENT (of this Report)  APPROVED FOR PUBLIC RELEASE; DISTRIBUTION UNLIMITED.		
17. DISTRIBUTION STATEMENT (of the abstract entered in Block 20, if different from Report)		
18. SUPPLEMENTARY NOTES		
19. KEY WORDS (Continue on reverse side if necessary and identify by block number) Electromagnetic pulse Pulser system Pulse generator		
20. ABSTRACT (Continue on reverse side if necessary and identify by block number)  This report presents a description of the development, design, fabrication, and field testing of the TEMPS (Transportable EMP Simulator), a system conceived and specified by the Harry Diamond Laboratories (HDL), Laboratory 1000,* and funded by the Defense Nuclear Agency (DNA). *At the time that the request for proposal was issued (March 1971) this group reported administratively to the U.S. Army Mobility Equipment Research and Development Center, Fort Belvoir, Va.		

## DD Form 1473: Report Documentation Page

SECURITY CLASSIFICATION OF THIS PAGE (When Data Entered)

The basic system is a simulator with the geometry of a cylinder parallel to the ground surface driven at its center by a high voltage capacitive pulser and terminated resistively at its ends to ground. The pulser and cylindrical antenna are supported by means of a dielectric support structure at elevations of up to 20 meters measured from the antenna/pulser centerline to ground.

Essentially, TEMPS has three individual subsystems: the pulse generator, the cylindrical antenna, and the support structure.

The pulse generated is a bilateral Marx generator-peaking capacitor circuit switched in series with the load impedance (the antenna) by means of a single, near uniform field, pressurized gas output switch. The pulser is contained within a biconical transmission line at the center of the cylindrical antenna. The biconical line guides line guides and launches the EM wave, produced by discharge of the pulser, from the small dimensions associated with the high voltage output switch to the large diameter (30 feet) cylindrical antenna.

A peaking capacitor circuit is employed to produce the fast rising load current that the Marxes cannot supply because of their stray series inductance.

Pulse generator capacity is 2.5 nF and produces a roughly double exponential output voltage pulse into the load impedance. Output pulse amplitude is greater than 6 MV and rises to this value in about 8 nsec (10 to 90 percent). Pulse decay time is approximately 300 nsec (e-fold). System electrical parameters are sufficient to produce a peak radiated electromagnetic field greater than 50 kV/m at a radial distance of 50 meters from the antenna.

The cylindrical antenna is a wire cage structure 30 feet in diameter and 1000 feet long. The antenna guides the lower frequency content of the EM wave from the source region as a rod to plane transmission line to the ends of the antenna, terminated to ground by way of resistors which match the characteristic impedance of the antenna viewed as a transmission line.

The antenna/pulser support structure is designed to be transportable, capable of being rapidly disassembled, transported and reassembled at a new location. The support structure is a free standing guyed system to minimize site preparation and disturbance and it is fabricated from dielectric material as far as practical for high voltage insulation and for minimum disturbance of the EM fields produced by the system.

## ABSTRACT

This report presents a description of the development, design, fabrication, and field testing of the TEMPS (Transportable EMP Simulator), a system conceived and specified by the Harry Diamond Laboratories (HDL), Laboratory 1000,\* and funded by the Defense Nuclear Agency (DNA).

The basic system is a simulator with the geometry of a cylinder parallel to the ground surface driven at its center by a high voltage capacitive pulser and terminated resistively at its ends to ground. The pulser and cylindrical antenna are supported by means of a dielectric support structure at elevations of up to 20 meters measured from the antenna/pulser centerline to ground.

Essentially, TEMPS has three individual subsystems: the pulse generator, the cylindrical antenna, and the support structure.

The pulse generated is a bilateral Marx generator-peaking capacitor circuit switched in series with the load impedance (the antenna) by means of a single, near uniform field, pressurized gas output switch. The pulser is contained within a biconical transmission line at the center of the cylindrical antenna. The biconical line guides line guides and launches the EM wave,

---

\* At the time that the request for proposal was issued (March 1971) this group reported administratively to the U. S. Army Mobility Equipment Research and Development Center, Fort Belvoir, Va.

produced by discharge of the pulser, from the small dimensions associated with the high voltage output switch to the large diameter (30 feet) cylindrical antenna.

A peaking capacitor circuit is employed to produce the fast rising load current that the Marxes cannot supply because of their stray series inductance.

Pulse generator capacity is 2.5 nF and produces a roughly double exponential output voltage pulse into the load impedance. Output pulse amplitude is greater than 6 MV and rises to this value in about 8 nsec (10 to 90 percent). Pulse decay time is approximately 300 nsec (e-fold). System electrical parameters are sufficient to produce a peak radiated electromagnetic field greater than 50 kV/m at a radial distance of 50 meters from the antenna.

The cylindrical antenna is a wire cage structure 30 feet in diameter and 1000 feet long. The antenna guides the lower frequency content of the EM wave from the source region as a rod to plane transmission line to the ends of the antenna, terminated to ground by way of resistors which match the characteristic impedance of the antenna viewed as a transmission line.

The antenna/pulser support structure is designed to be transportable, capable of being rapidly disassembled, transported and reassembled at a new location. The support structure is a free standing guyed system to minimize site preparation and disturbance and it is fabricated from dielectric material as far as practical for high voltage insulation and for minimum disturbance of the EM fields produced by the system.

## CONTENTS

	<u>Page</u>
APPENDIX A     A LABORATORY STUDY OF HORIZONTAL DIPOLES--TEMPS	225
APPENDIX B     CAPACITOR DEVELOPMENT AND TESTING	301
APPENDIX C     PROTOTYPE MARX GENERATOR SWITCH EVALUATION	351
APPENDIX D     SWITCH ACCEPTANCE TESTING	373
APPENDIX E     SOLID RESISTOR DEVELOPMENT	383
APPENDIX F     SOLID-DIELECTRIC GAS-GRADED PEAKING CAPACITOR	391
APPENDIX G     SINGLE-MODULE PEAKING CAPACITOR TESTS	401

## ILLUSTRATIONS

<u>Figure</u>		<u>Page</u>
90	Sketch of Inverse Cone Structure	226
91	Double-Ground-Plane Model Range	228
92	Radial Magnetic Field from an Unterminated Inverse Cone	230
93	Radial Magnetic Field from a Terminated Inverse Cone	231
94	Constant-Impedance Structure	232
95	Radial Magnetic Field from the Constant-Impedance Structure	233
96	Characteristic Impedance of a Rod-Over-Ground Structure	234
97	Radial Magnetic Field from a Resistively Loaded Structure	236
98	TDR Data for a Bicone-Cylinder Structure at 8.5-m Full-Scale Height	239
99	TDR Data for a Bicone-Cylinder Structure at 20-m Full-Scale Height	239
100	Radial Magnetic Field from 50:1 Model at 8.5-m Full-Scale Height	241
101	Radial Magnetic Field from 50:1 Model at 20-m Full-Scale Height	241
102	Radial Magnetic Field with Termination Cone at Close to Optimum Angle for 20-Meter Full-Scale Height	243



## ILLUSTRATIONS (cont.)

<u>Figure</u>		<u>Page</u>
103	Radial Magnetic Field with Termination Cone Close to Optimum Angle for 8.5-m Full-Scale Height	244
104	Radial Magnetic Field from a Capacitively Fed TEMPS at 8.5-m Full-Scale Height	244
105	Effective Cage Radius as a Function of Wire-to-Cage Radius	246
106	TDR Data with 40-Wire Model at 8.5-Meter Full-Scale Height	248
107	TDR Data with 14-Wire Model at 8.5-Meter Full-Scale Height	249
108	TDR Data with 40-Wire Model at 20-Meter Full-Scale Height	250
109	TDR Data with 14-Wire Model at 20-Meter Full-Scale Height	250
110	TDR Data on Terminated TEMPS Model	252
111	Effect of Solid-Metal-to-Wire Transition on Radial Magnetic Field	253
112	Effect of Brass Plates on Radial Magnetic Field of Wire Model	255
113	Effect of Sag on Radial Magnetic Field	257
114	Percentage Change in Waveform as a Function of Wire Sag	258
115	Magnitude of Single-Ground-Rod Impedance	262
116	Skin Depth as a Function of Frequency	271

## ILLUSTRATIONS (cont.)

<u>Figure</u>		<u>Page</u>
117	Radial Magnetic Field Over Real Earth with Incorrect Terminating Impedance	273
118	Radial Magnetic Field Over Real Earth with Correct Terminating Impedance	273
119	Radial Magnetic Field Over Real Earth with 1-m Tip Spacing	275
120	Radial Magnetic Field Over Real Earth with 2-m Tip Spacing	275
121	Radial Magnetic Field Over Real Earth with 3-m Tip Spacing	277
122	Radial Magnetic Field Over Real Earth with no Termination System	277
123	Vertical Electric Field Over Real Earth	278
124	Current Waveforms Down a Transmission Line Over Real Earth	278
125	Comparison of Calculated and Measured Current Waveforms	282
126	Vertical Electric Field from Horizontal TEMPS	284
127	Vertical Electric Field with Termination Cone Attached to Bicone on One Side	284
128	Vertical Electric Field from Tilted-Dipole Made of Termination Cones	286
129	Vertical Electric Field from Tilted Bicone-Cylinder Configuration	286
130	Radial Magnetic Field from Tilted Bicone-Cylinder Configuration	287

## ILLUSTRATIONS (cont.)

<u>Figure</u>		<u>Page</u>
131	Photograph of 150:1 TEMPS Model	289
132	Large and Small Time Approximations to Waveform of a Single-Wire Transmission Line	293
133	Prototype Capacitor Test Circuit	305
134	TEMPS Storage Capacitor Test Bed	307
135	Five Station Capacitor Test Stand	311
136	Pulse Discharge Waveform (Calculated and Actual), Condenser Products Prototype Capacitor	313
137	Prototype Capacitor High Reversal Waveform	316
138	High Reversal Test Equivalent Circuit	317
139	Burst Tube, Station No. 1	319
140	Computed and Measured Pulse Discharge Current, Series Limiting Resistance Installed	321
141	Maxwell Prototype, TEMPS Energy Storage Capacitor	324
142	Energy-Storage Capacitor	325
143	Connector Configurations	326
144	Maxwell Prototype Capacitor--Normal Discharge Waveform	330
145	Maxwell Prototype Capacitor--Fault Waveform	331
146	Equivalent Circuit--Fault Test	332

## ILLUSTRATIONS (cont.)

<u>Figure</u>		<u>Page</u>
147	Equivalent Circuit Representation of Capacitor Showing Internal Parameters	334
148	Tubular Capacitor with End Connections	337
149	Conducting Cylinder Surrounding Tubular Capacitor	337
150	Capacitor Test Configurations	340
151	Capacitor and Load Circuit	341
152	Capacitor Inductance Measurement Monitor Output Waveform	344
153	"Stripline" Capacitor Output Waveform into an Inductive Load	345
154	Stripline Capacitor Equivalent Circuit	346
155	Statistical Curve for a Single Switch	353
156a	Prototype Marx Switch	356
156b	Prototype Siege Switch	357
157	Test Stand	359
158	SIEGE Gap (Used), S194, 15 psig N <sub>2</sub> , ~ 150 Shots	363
159	TEMPS Marx Switch Self-Break Voltage Versus Pressure	364
160	TEMPS Prototype	366
161	TEMPS Prototype	367
162	TEMPS Prototype	368
163	Rail Switch Test Stand Current Waveform	369

## ILLUSTRATIONS (cont.)

<u>Figure</u>		<u>Page</u>
164	TEMPS Prototype	370
165	Sample Log Sheet--Midplane	375
166	Sample Log Sheet--Electrode	376
167	Sample Log Sheet--Switch	377
168	Marx Switch Test Bed	378
169	Switch Acceptance	380
170	Test Setups	384
171	Typical Pulse Current Waveforms	386
172	Test Circuit	392
173	Parallel Plate Capacitor Section	393
174	General Test Configuration for Capacitor Section	396
175	Tin Foil Contour	399
176	Single Module of Peaking Capacitor	403
177	Basic Test Apparatus	404
178	Test Apparatus	407
179	Basic Testing Fixture	408
180	Test Circuit	409
181a	Idealized Charging Waveform when Switch Remains Open	410
181b	Idealized Charging Waveform when Switch Closes at $t = \pi/2\omega$ (Battery Limit)	410

## ILLUSTRATIONS (cont.)

<u>Figure</u>		<u>Page</u>
182	Experimental Waveforms for Various Switching Point	414
183a	Single Sheet Solid Dielectric Test Module Exploded View of Section	416
183b	Polypropylene Ring for Single Sheet Test	416
184	Single Sheet Solid Dielectric Failure	417
185a	Multi-Layer Solid Dielectric Test Module Type "A"-Exploded Section View	419
185b	Multi-Layer Solid Dielectric Test Module Type "B"-Exploded Section View	419
186	Polypropylene Rings and Aluminum Electrodes	420
187	Life Test Dendriting of Polypropylene (20 Sheets; 0.001 in Each)	421
188	Single Module Liquid Dielectric Test Apparatus	423

## TABLES

<u>Table</u>		<u>Page</u>
X	Measured and Calculated Impedances of Cylindrical Structures	252
XI	Terminating System for an Antenna Height of 20 Meters	267
XII	Terminating System for an Antenna Height of 10 Meters	268
XIII	Terminating System for 3-Meter Tip Clearance--All Heights	270
XIV	Circuit Inductance	309
XV	Circuit Inductance, Condenser Products Capacitors	312
XVI	Normal Discharge Shot Summary	312
XVII	Close Spaced Conductor Test Results	327
XVIII	Widely Spaced Stripline Conductors	328
XIX	Maxwell Laboratories Prototype Capacitors Shot Summary--Normal Discharge Mode	329
XX	Test Results	397

APPENDIX A  
A LABORATORY STUDY OF HORIZONTAL DIPOLES--TEMPS

by  
W. E. Scharfman  
Stanford Research Institute



## A.1 INTRODUCTION

The Transportable Electromagnetic Pulse Simulator (TEMPS) was built for the Harry Diamond Laboratories by Physics International. It is used to field test the EMP vulnerability of military electronics equipment to a high-altitude nuclear detonation. It is capable of producing threat-level fields at test sites 50 meters away from the feed points. The pulse generator is a Marx generator that is essentially a capacitive energy source.

The TEMPS wave launcher consists of an early-time structure that is a bicone and a late-time structure that consists of all the structure beyond the bicone. SRI had the task of aiding in the selection of the late-time-antenna concept and of providing engineering design data in order to bring the concept from the design stage to a piece of field equipment. A large portion of the data has been gathered using experimental modeling techniques. These will be described in later sections of the report.

The most important specifications that affect the design of the late-time antenna (LTA) are the following

- Coverage: 100 linear meters broadside, at a range of 50 meters
- Pulse duration: 800 nsec, exponential decay 90 to 10 percent
- Pulse undershoot: 20 percent maximum
- Height: variable from 8.5 to 20 meters (originally 6 to 20 meters)

Maximum overall length: 300 meters

Polarization: Horizontal with up to 15 degree rotation.

Very early in the program it was necessary to determine the generator capacitance requirement. Therefore, several LTA concepts were briefly explored to obtain an estimate of this quantity. The concepts explored at this stage were the following:

Inverse-cone structure

Constant-impedance-terminated structure

Resistively loaded structure

These are discussed in Section A.2.

## A.2 LTA CONCEPTS

A.2.1 Inverse-Cone Structure. This structure starts at the end of the bicone with a diameter equal to the bicone and then linearly decreases in diameter throughout its length. Figure 90 is a sketch of such a structure.

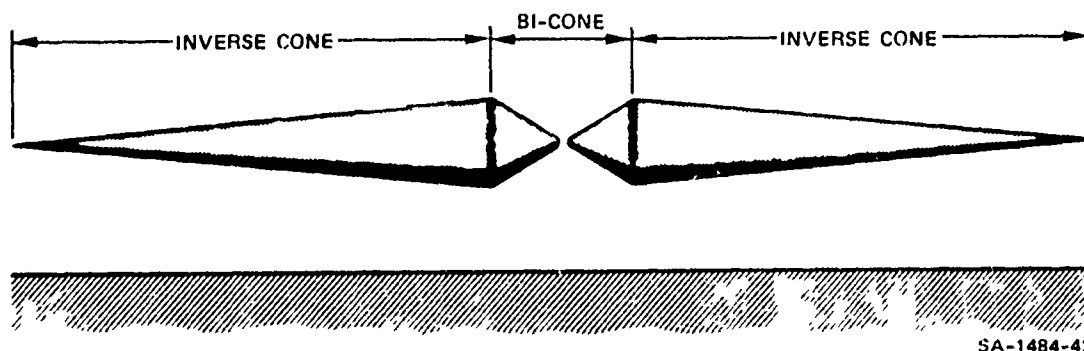


Figure 90 Sketch of inverse cone structure.

At very late times the field produced by this structure, when unterminated, is a function of the generator and antenna capacitance ( $C_g$  and  $C_a$  respectively). The low-frequency content is maximized when  $C_g \gg C_a$ . We have therefore measured  $C_a$  on the scaled model at a frequency of about 100 kHz. When scaled appropriately and taking into account a full dipole, the value of  $C_a$  was about 3100 pF. For  $C_g = 3 C_a$  a generator capacitance of 9.3 nF would be required.

In order to study the radial magnetic field produced by this structure, a 150:1 scale model of the antenna was constructed and used on a double-ground-plane system, as shown in Figure 91. The horizontal ground plane models the earth, and the vertical ground plane is a plane of symmetry that allowed us to use only half the antenna structure. It also allowed us to feed the antenna from a coaxial cable. At this stage of the study almost perfectly conducting ground planes were used. Later modeling was done over real earth.

Magnetic-field sensors were mounted at a scaled distance equal to 50 meters from the axis and at scaled transverse ranges of 5.5, 55, and 105 meters. These sensors were labeled H1, H2, and H3 respectively. The sensors were essentially slots that were shorted. A current transformer around the shorting wire gave a voltage output that was proportional to the magnetic field. The  $1/e$  decay of the sensors at this time was about 14 nsec and was later increased to 40 nsec.\* The sensor decay time thus produced a sag of about 25 percent at the end of 5 nsec for a step-function input. (Five nsec corresponds to 750 nsec full-scale for this model.)

---

\*The data reported in Section A.2 of this report were taken with a 14-nsec decay sensor; the remainder used a 40-nsec decay time sensor.

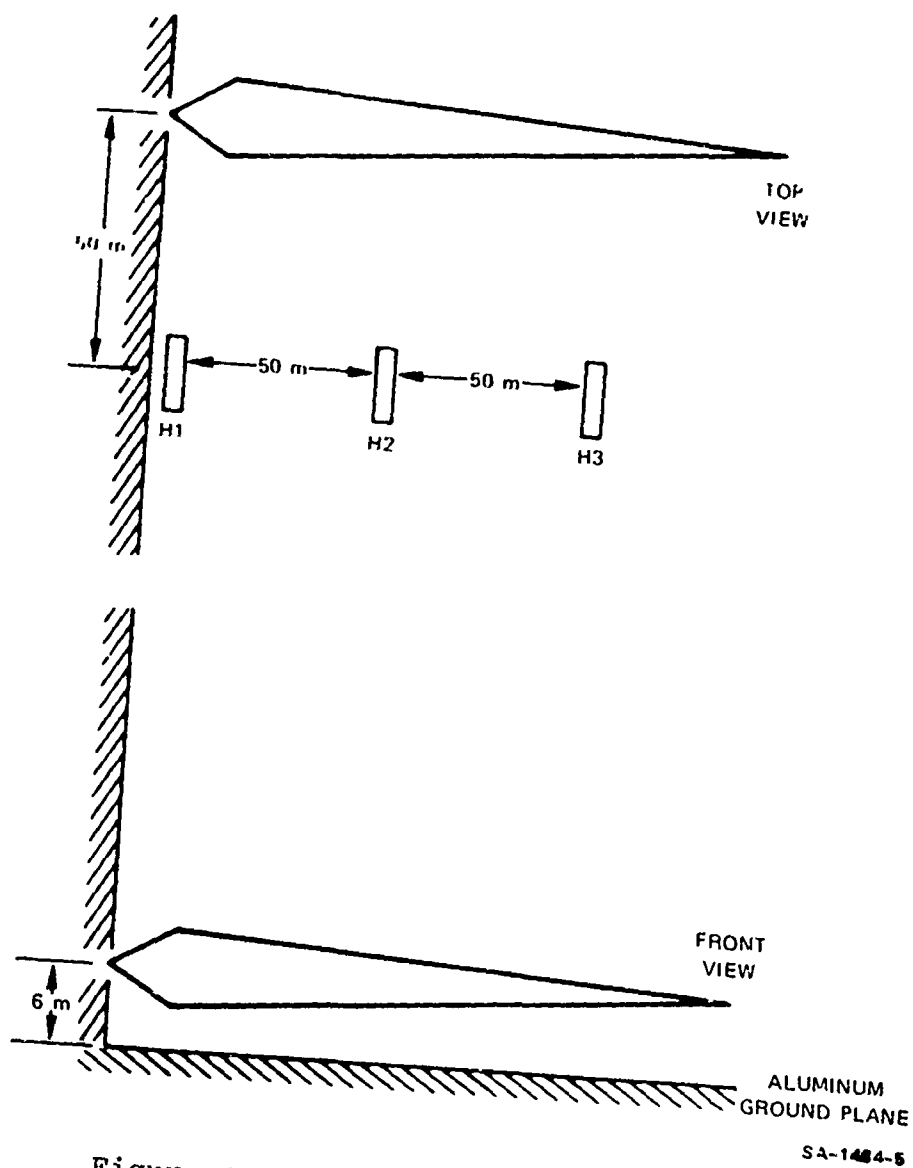


Figure 91 Double-ground-plane model range.

Since the horizontal electric field goes to zero in a perfectly conducting ground plane, the radial magnetic field was measured. This may be related to the incident fields.

Most of the measurements were taken with a rectangular input pulse because distortions in the waveform produced by the wave launcher are most easily seen with this type of pulse. As the antenna design became better defined, exponentially decaying pulses were also used.

The radial magnetic field for a 5-nsec rectangular pulse input is shown in Figure 92. The scaled antenna height above ground is 6 meters. The following are several important features of this figure:

(a) Pulse Duration--The pulse duration decreases as one moves off axis from sensor H1 to sensor H3. This is because the signal reflected from the unterminated structure produces a magnetic field of sign opposite to the original pulse. At H1 this signal arrives at a scaled time of 900 nsec. Therefore the full input-pulse duration is seen at H1. At H2 and H3 it arrives at 750 and 375 nsec producing shortened pulses at H3. The reflected signal arrives at B at H1, and at C at H3.

(b) Large Undershoot--When the reflected signal does arrive at the sensor before the input pulse is over, they buck each other, producing a shortened pulse, as at H3 (Region C to D). When the reflected signal arrives after the input pulse is over, it produces negative signals that are much larger than the 20-percent undershoot that is allowed.

(c) Pulse Droop--Although some of the droop is due to the sensor, there is a considerable droop due to the structure. This is attributed to the fact that the structure looks like a nonuniform transmission line at times longer than the round-trip time to the ground. This nonuniform line produces continuously increasing mismatch, which decreases the magnetic field produced by the structure.

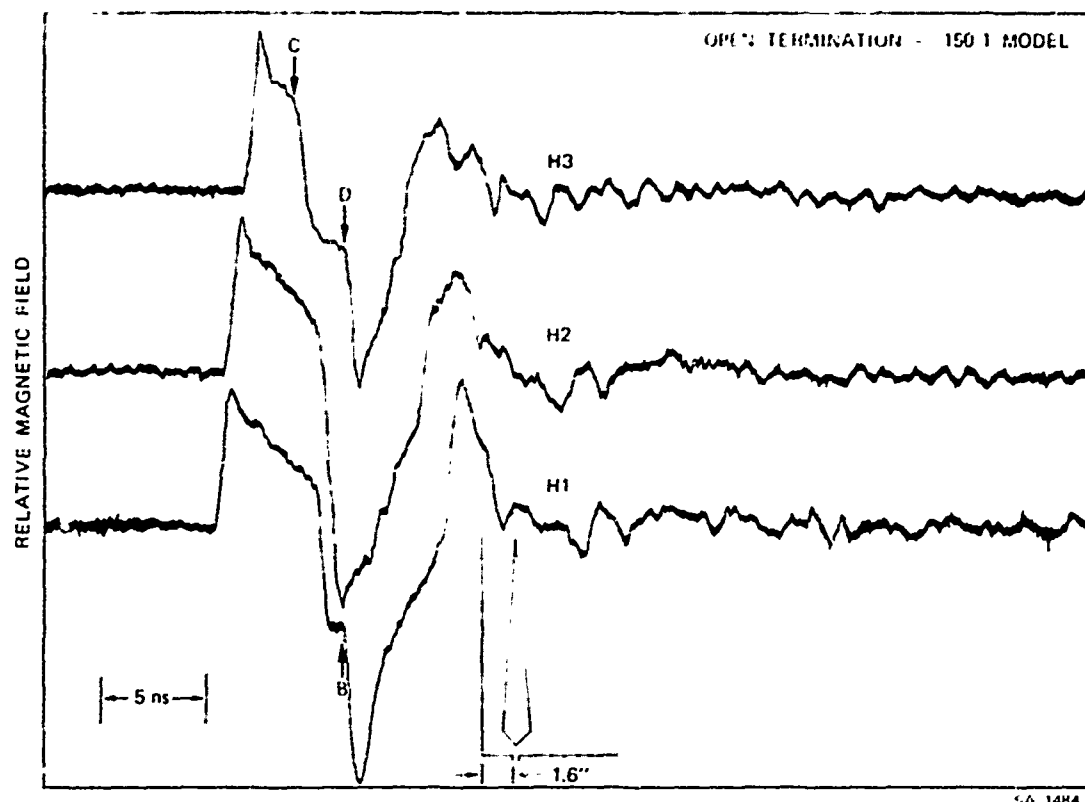


Figure 92 Radial magnetic field from an unterminated inverse cone.

The results of terminating the structure in an impedance equal to its characteristic impedance near the end of this line are shown in Figure 93. Features a and b described above, are considerably improved, but c does not improve. The large negative-going signal at 5 nsec is due to the end of the pulse and would be smaller with an exponentially decaying input pulse. It is not due to end reflection. The termination eliminates the end reflection that produced pulse-duration shortening and large undershoot. The pulse droop is still present and a new feature is present--the spikes at A and B in Figure 93. These are produced by the current that flows through the termination. For a horizontal antenna over ground, this corresponds to the azimuthal magnetic field produced by the currents that flow vertically through the termination to ground. The radial magnetic sensors pick up a component of the field.

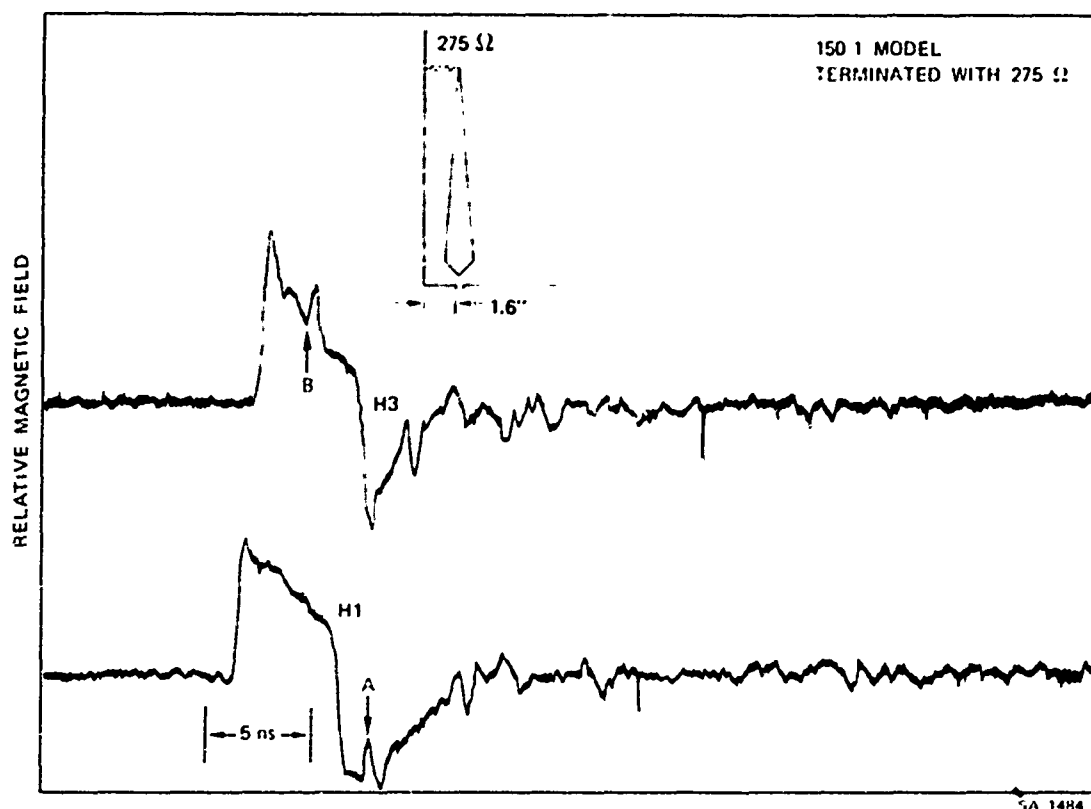


Figure 93 Radial magnetic field from a terminated inverse cone.

A.2.2 Constant-Impedance-Terminated Structure. In order to eliminate the pulse sag, a uniform transmission line was built onto the bicone section and a constant-impedance transition region was added on to bring the transmission line down to ground gradually, with the idea of reducing the spikes produced by the termination shown in Figure 93. The structure was as shown in Figure 94.

The fields are shown in Figure 95. Note that the input pulse of 10 nsec is twice as long as was previously used and corresponds to a 1500-nsec full-scale pulse. The sensor sag over this time (10 nsec) almost exactly matches the measured

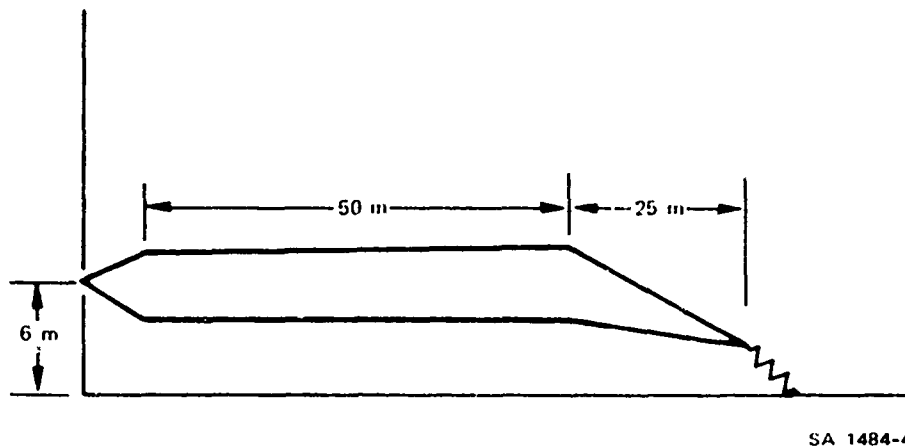


Figure 94 Constant-impedance structure.

response, indicating that a 1500-nsec pulse could be transmitted without distortion from a structure only 90 meters in half-length. The negative-going signals are due to the rectangular-pulse turn-off and would not be present with an exponentially decaying pulse. The spikes are reduced considerably.

Sensor H3 received only very weak signals. It is outside the transverse dimension of the structure. This suggests that the antenna need be only somewhat longer than the site to be tested. Its length is not dictated by pulse-length considerations.

The capacitance required to drive the structure with a required pulse duration can be found by considering the time constant for an RC circuit where  $R$  is the characteristic impedance of the transmission line and  $C$  is the capacitance. For a  $1/e$  time of 350 nsec and a  $Z_0$  of 70 ohms for each side of the antenna considered as a transmission line,  $C = 2.5$  nF. This value of capacitance is consistent with that proposed by PI.



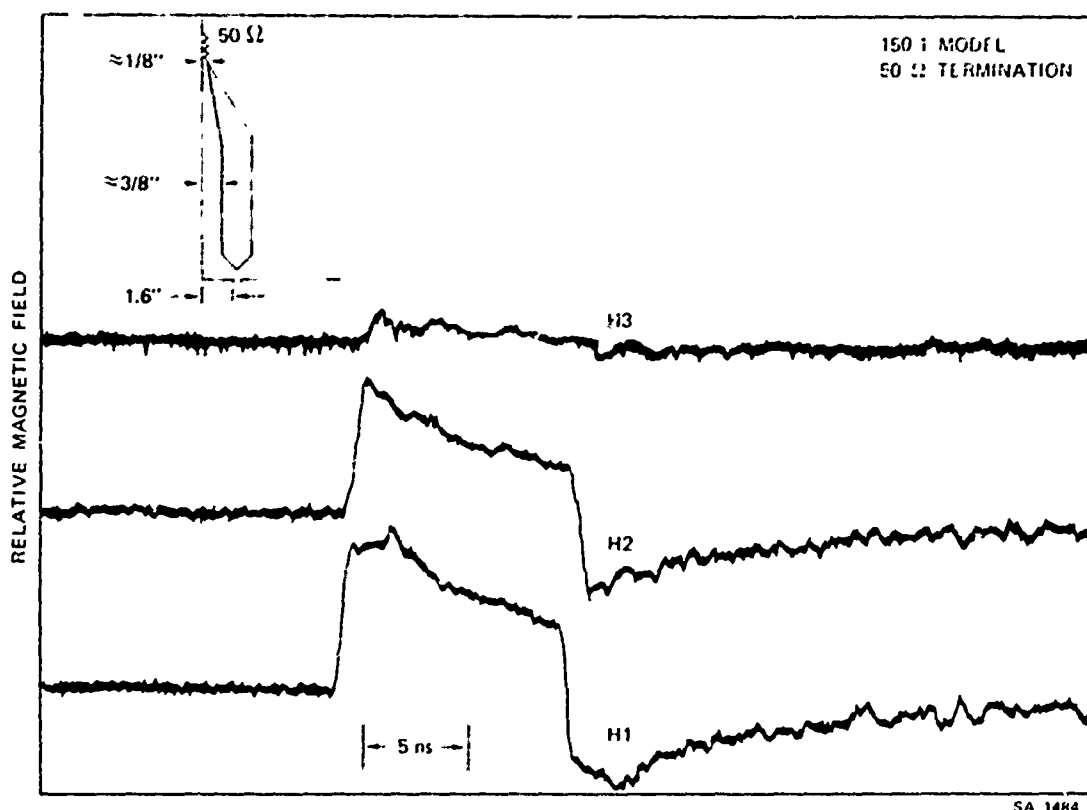
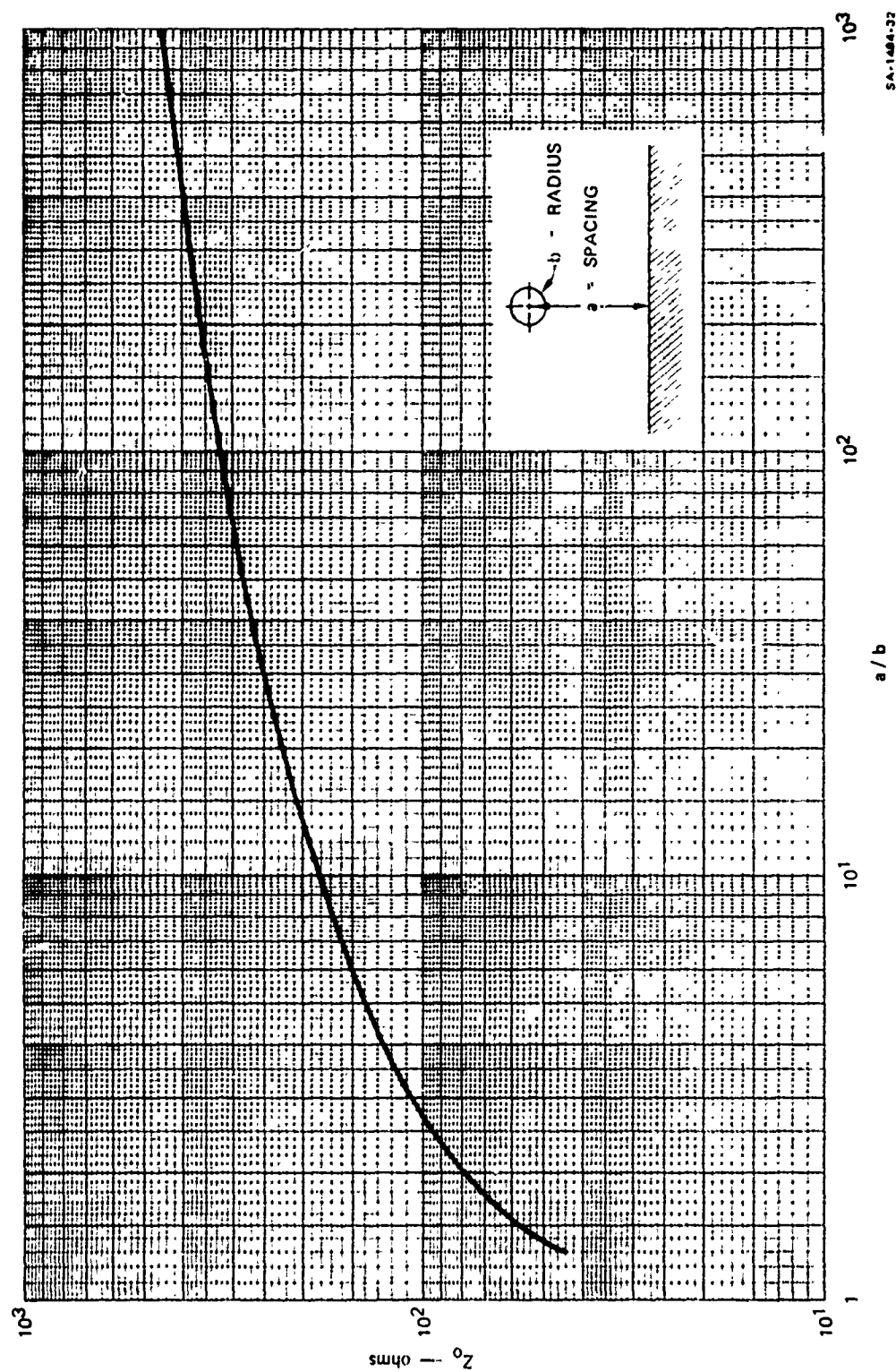


Figure 95 Radial magnetic field from the constant-impedance structure.

For the clear time to be greater than the pulse risetime, the diameter of the bicone where it attaches to the LTA must be 30 feet. Therefore, to minimize the discontinuity at the junction, the diameter of the cylindrical portion of the LTA should be 30 feet. The cylinder height for the characteristic impedance to be 70 ohms may be found from Figure 96, which shows  $Z_0$  as a function of the height-to-radius ratio (Reference A-1). For a 15-foot radius, the height must be about 8 meters for a  $Z_0$  equal to 70 ohms. At greater heights the  $Z_0$  is even greater, so that the decay time will be longer. At a height of 20 meters,  $Z_0 = 130$  ohms.



SA-1484-32

Figure 96 Characteristic impedance of a rod-over-ground structure.

With the approval of the sponsors at the Harry Diamond Laboratories the range of heights was fixed at 8.5 to 20 meters.

Although the increase in minimum height would improve the performance of the inverse-cone antenna, it still would have significant pulse sag. Tests with a capacitive pulser near the feed point showed a pulse duration somewhat less than required and a pulse shape that decreased more nearly linearly than exponentially. In addition, a transition section to ground would still be required to minimize the spikes discussed earlier.

The constant- $Z_0$  LTA provides the required pulse duration with an exponential decay and minimizes the waveform distortion due to termination of the antenna. In addition, with the cylindrical section made of several modules, great flexibility is available to the user. For testing small sites the entire cylindrical length may not be needed, so that the antenna length may be only 200 meters instead of 300 meters.

A.2.3 Resistively Loaded Structure. Resistively loaded antennas were briefly investigated. With this type of antenna, series resistors are added along the antenna length so that the current is very small when it reaches the end. No termination to ground would be needed with such a system. However, analyses of resistively loaded cylindrical antennas in free space indicated that the antenna length must be sufficiently long compared to the pulse duration (defined as the time for the decaying pulse to cross the zero-amplitude axis) so that the resistance loading is gradual even for the longest wavelengths (Reference A-2). Otherwise large undershoot will occur. For an antenna

half-length equal to 1.25 times the pulse length, the undershoot is about 25 percent. This is still larger than the specifications allow. For an 800-nsec pulse duration the antenna half-length would have to be 1000 feet or 305 meters. Since the TEMPS maximum overall length was 300 meters the undershoot with a resistively loaded, unterminated antenna would be excessive.

The results for one type of loading are shown in Figure 97. The antenna was made up of 4-inch lengths of 1/4-inch-diameter rods with resistors connecting the sections. The input pulse was an 11-nsec rectangular pulse. The undershoot is about 35 percent. The pulsewidth at the zero points was only about 5.5 nsec even for an 11-nsec input pulse. Thus, for a capacitive pulser with a decaying input voltage, the zero crossing will occur even earlier. Thus the pulse duration of 800 nsec full scale would not be met.

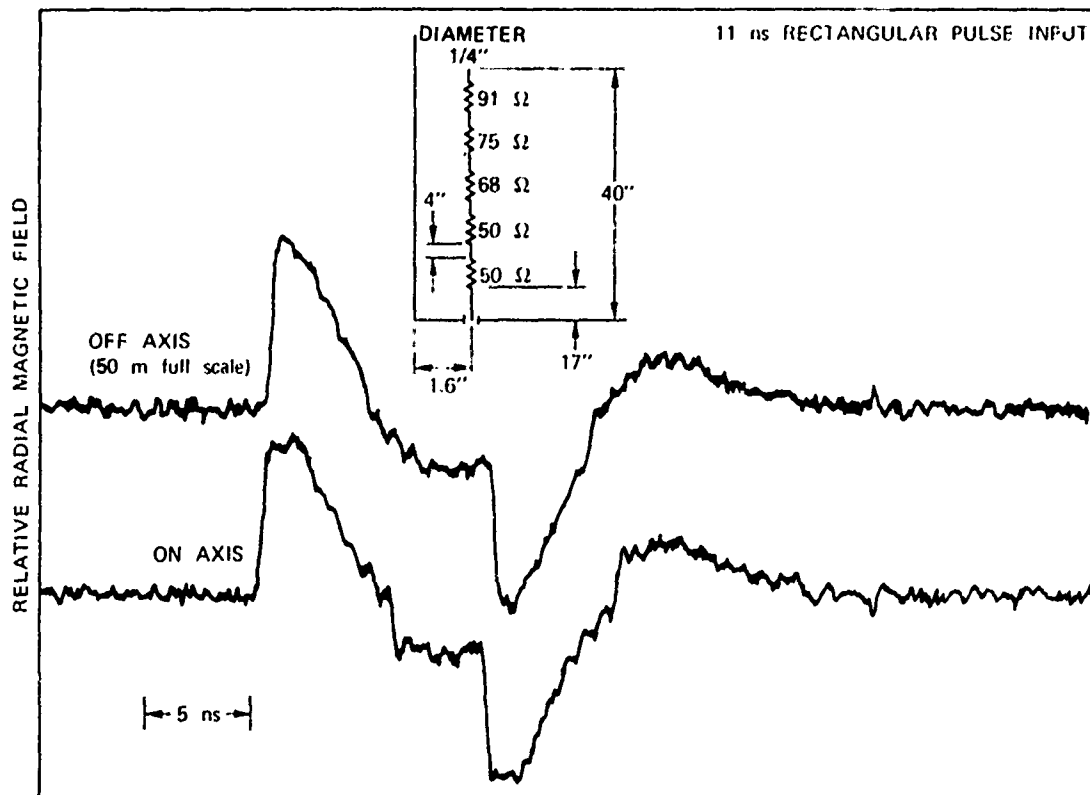


Figure 97 Radial magnetic field from a resistively loaded structure.

Although no careful attempt was made to optimize the loading, several experiments with different loading showed that, with the pulse duration longer than the antenna half-length, the undershoot was excessive or the duration was too short.

The undershoot could be reduced by terminating the structure, but if the termination was brought straight down to ground, spikes appeared in the magnetic field.

Since the constant- $Z_0$  terminated structure looked satisfactory and did not require the complication of series resistors, further studies of resistively loaded antennas were not pursued.

### A.3 STUDIES OF CONSTANT-IMPEDANCE LTA

The remainder of this appendix is concerned with design problems of the constant- $Z_0$  LTA.

A.3.1 Transition from Free-Space Dipole to Transmission Line. At times before the fields from the dipole have reached the ground and reflected back to the antenna, the antenna operates as a dipole in free space. Since, at the minimum height of 8.5 meters the minimum round-trip time for a ground reflection to arrive back at the feed point is about 56 nsec, the input pulse will have traveled along the bicone and onto the cylinder before ground interaction starts. Thus the early-time portion of the pulse will not be affected by the presence of the ground.

At times longer than the round-trip time to the ground, the LTA will look more and more like a transmission line with characteristic impedance that is a function of the cylinder height and radius. This is plotted in Figure 96 and is calculated from a formula in Reference A-1.

Time-Domain-Reflectometer (TDR) plots showing the response to the 50:1 model of a 60-ohm monocone joined to a cylinder with a scaled diameter of 30 feet are shown in Figures 98 and 99. Figure 98 is for a scaled height of 8.5 meters and Figure 99 corresponds to a scaled height of 20 meters. The values of  $Z_0$  for these heights are 70 and 130 ohms, respectively. Since the double-ground-plane system was used, only one-half the antenna was required. The impedance of a 40.4-degree half-angle cone over ground is 60 ohms. The measured value is about 64 ohms.

For both figures the impedance is within about 10 percent of the transmission-line impedance in one round-trip time. The increase in impedance as the wave passes the junction of the cone and cylinder is clearly discernible. Also, a marked decrease in the slope of the reflected signal occurs at a time corresponding to one round-trip time.

These figures give a measure of the driving-point impedance as a function of time. However, the radiated magnetic field is not simply related to this quantity. The TDR plots show the integrated effect of reflections back at the feed point. The radiated magnetic field depends on the current distributions as a function of time along the antenna.

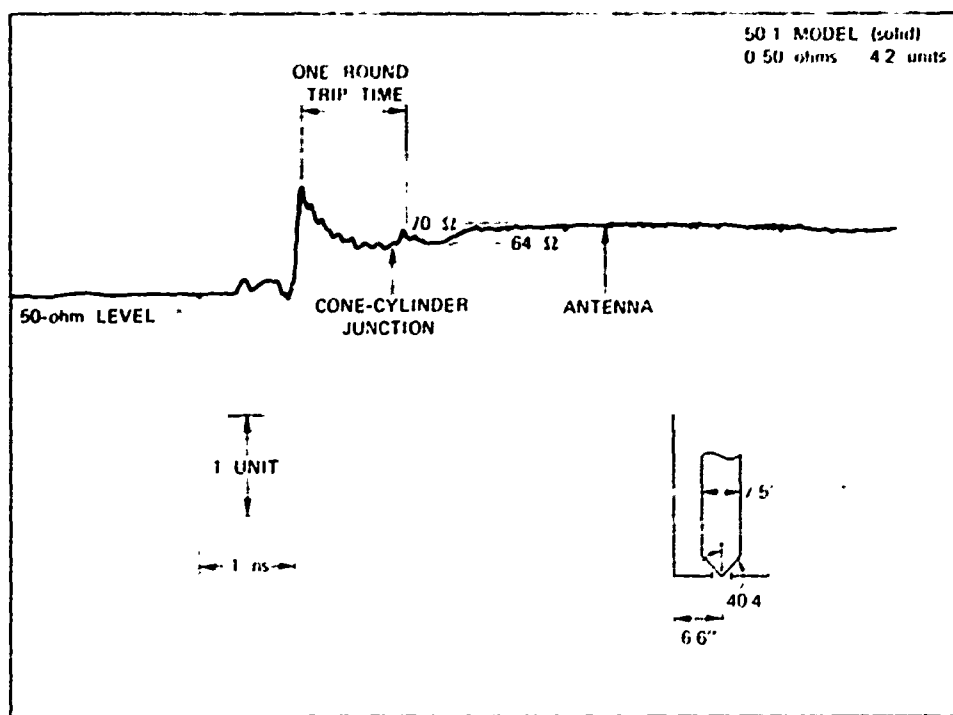


Figure 98 TDR data for a bicone-cylinder structure at 8.5-m full-scale height.

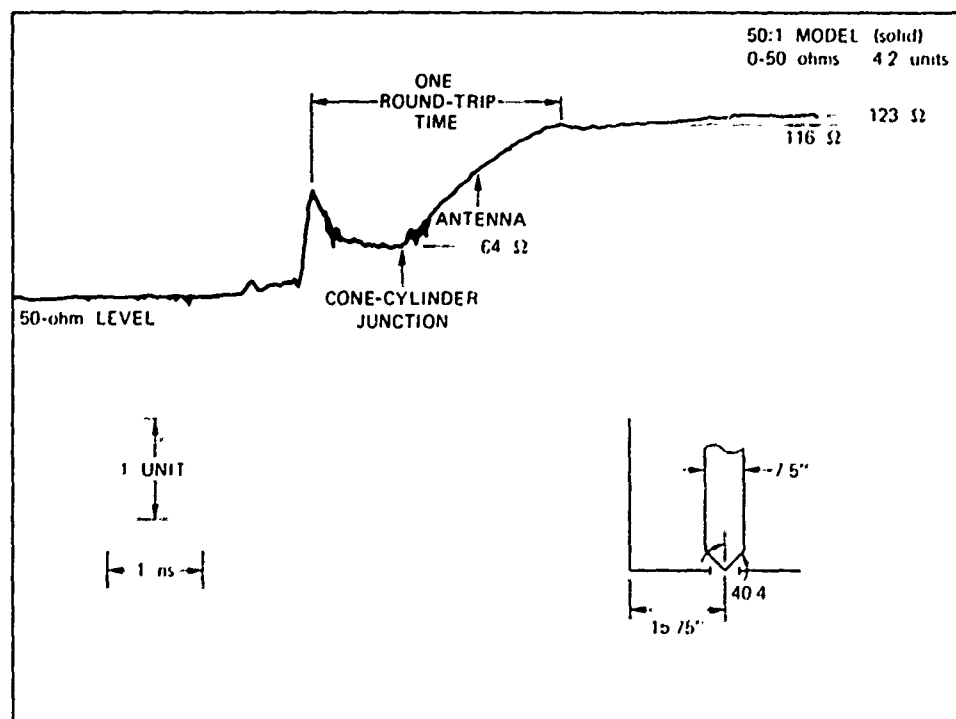


Figure 99 TDR data for a bicone-cylinder structure at 20-m full-scale height.

The radiated radial magnetic field on-axis at a scaled distance of 50 meters for the 50:1 model at a height of 8.5 meters is shown in Figure 100. This is the same antenna configuration as for the TDR in Figure 98. For the moment, ignore times greater than 5 nsec. The clear time is slightly less than the risetime, so that the peak is clipped. After the peak field is radiated, the discontinuity at the cone-cylinder junction produces a reflected signal that decreases the radial magnetic field. After about 0.7 nsec the radial magnetic field increases to almost the peak field level.

As reflected signal from the ground returns to the antenna structure, it allows more current to flow, increasing the magnetic field. Another way of describing this is that the ground-reflected signal scatters off the structure, producing a magnetic field of the same sign as the originally radiated field. Thus, the transition to a transmission-line mode increases the magnetic field after a time of the order of the round-trip time to ground and back to the structure. The effect is most pronounced at a scaled height of 8.5 meters and decreases with increasing height. Figure 101 shows a plot of radial magnetic field for a scaled antenna height of 20 meters. The increase in signal at 2.25 nsec is due to the ground interaction. Note that the level does not return to the peak field in this case.

A.3.2 Terminating Cone. In order to prevent spikes in the waveform, a long terminating cone of approximately constant local  $Z_0$  (constant height-to-radius ratio) is used. Figure 101 shows what happens for one value of the angle between the cylinder axis and the cone axis.



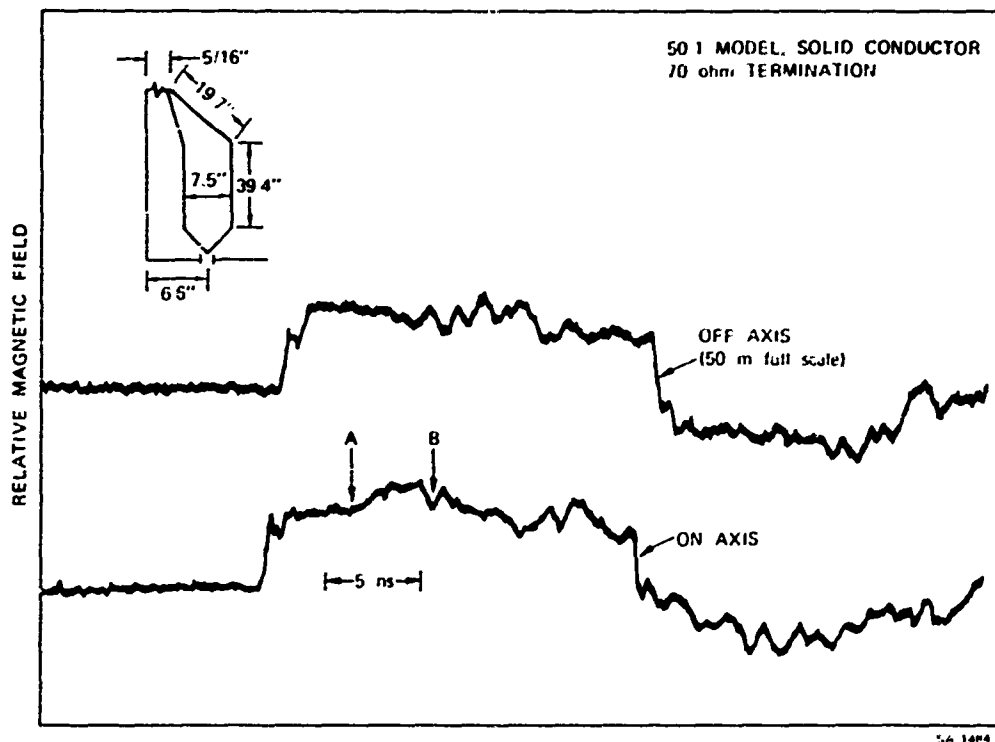


Figure 100 Radial magnetic field from 50:1 model at 8.5-m full-scale height.

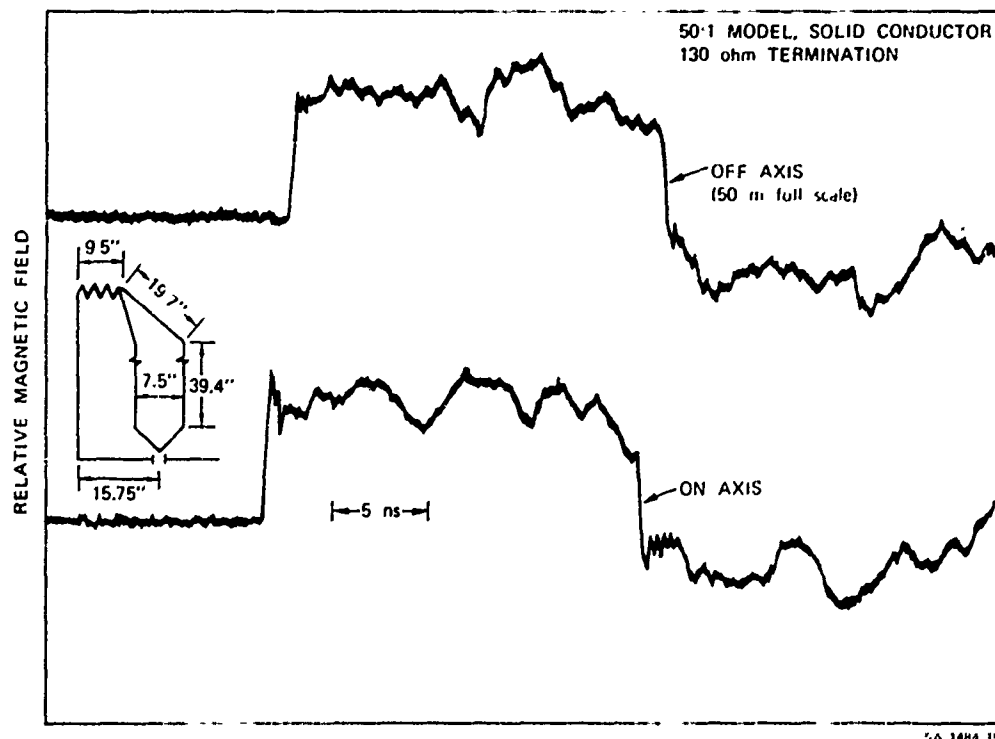


Figure 101 Radial magnetic field from 50:1 model at 20-m full-scale height.

Consider Figure 101. After the ground interaction has occurred, the magnetic field is constant until about 4.5 nsec. This is the time at which the signal passes from the cylinder onto the terminating cone. At this point, the radial magnetic field increases for a time and then decreases markedly. The termination is reached at 8.5 nsec.

The increase is due to the introduction of a component of current flow vertically as the current flows onto the cone. The vertical current produces an azimuthal magnetic field that adds to the radial field from the rest of the structure. However, for the angle shown, the value of  $Z_0$  is increasing as the cone approaches ground. This is produced by the increasing value of local-height-to-radius ratio. Eventually the negative field due to mismatch is larger than the increase due to vertical current, and the resultant field decreases. For the particular terminating resistors,  $Z_{load} < Z_0$  and the reflected current increases the magnetic field.

A more optimum angle for the terminating cone is shown in Figure 102. These data were taken with the 150:1 model. The lower trace shows the on-axis magnetic field at a range of 50 meters, while the upper trace shows the field at 50 meters off axis. The uniform cylinder is 100 meters long full-scale, and the terminating cone is 50 meters long full-scale. The start of the terminating cone produces a small ( $\sim 10$  percent) increase in magnetic field, and arrival at the termination produces an even smaller dip. This is a reasonable compromise. The angle from the dipole axis is 22.5 degrees for this case (antenna height 20 meters full scale) and about 9.3 degrees for an antenna height of 8.5 meters full-scale. Figure 103 shows the magnetic field

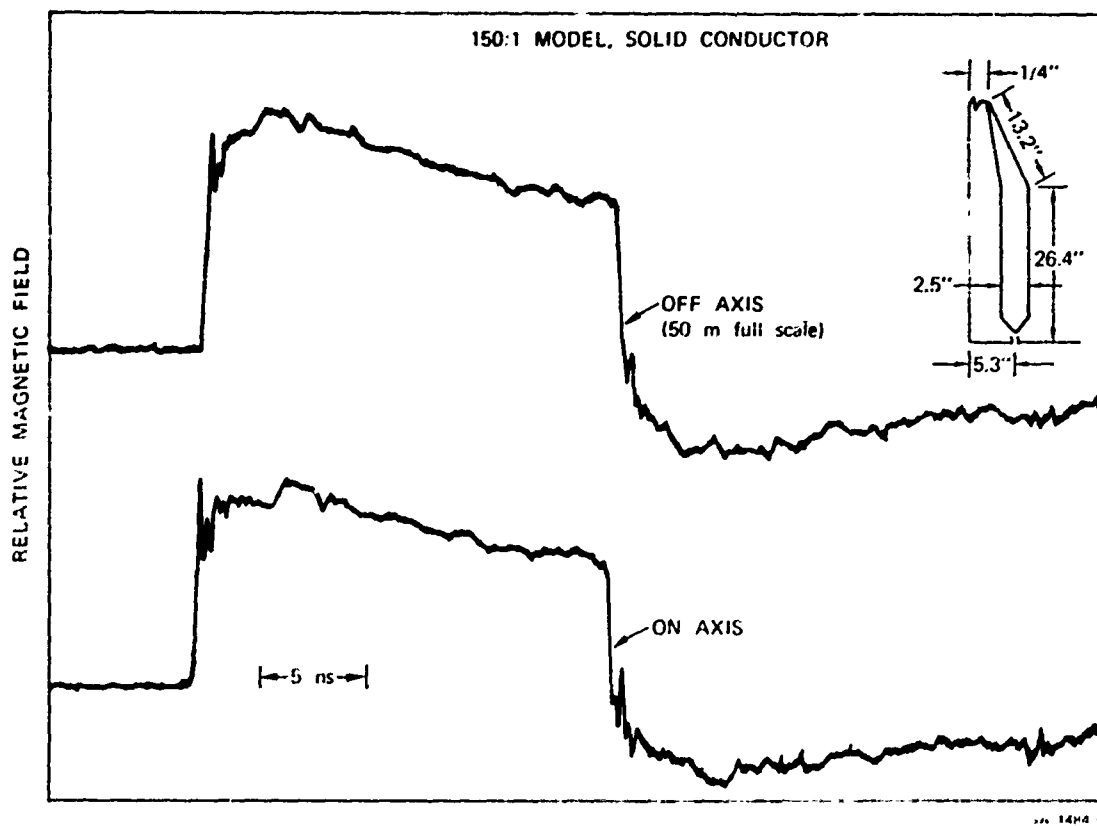


Figure 102 Radial magnetic field with termination cone at close to optimum angle for 20-meter full-scale height.

produced at 8.5-meters height and with a rectangular input pulse. When the antenna was fed with a capacitive pulser with a capacitance scaled to the 2.5-nF full-scale capacitance, the fields of Figure 104 resulted. The waveform is a reasonably good double exponential, with small deviations starting at the time the current reaches the beginning of the terminating cone. The full-scale time to the zero crossing is greater than 1000 nsec. Some provisions should be made in the field so that the cone angle may be varied slightly at each height to optimize performance.

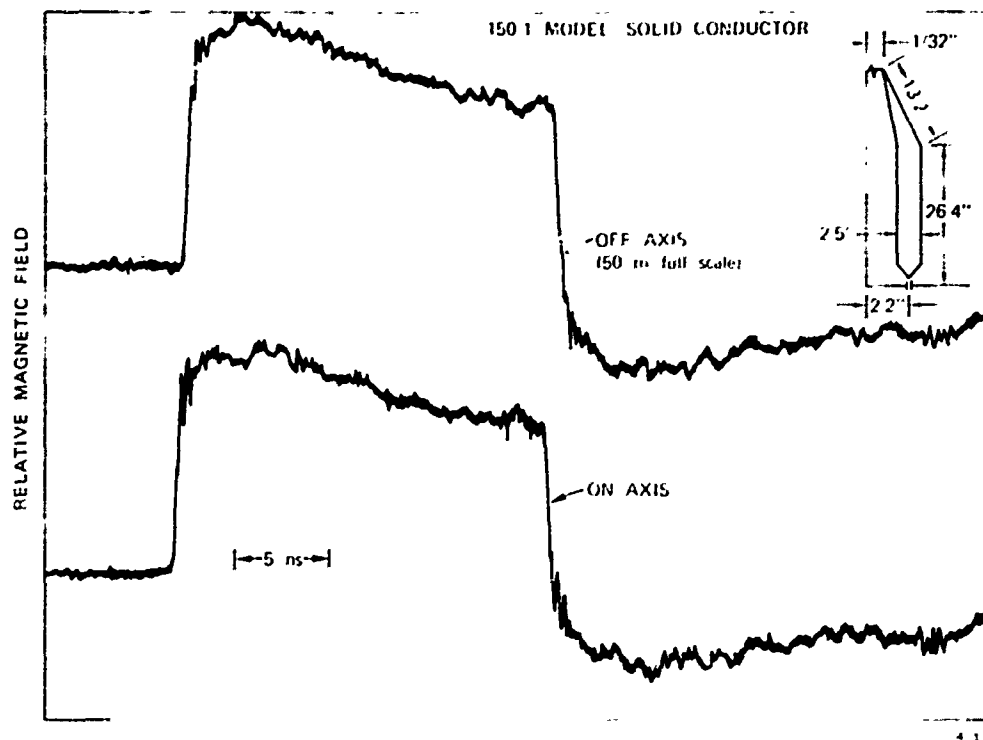


Figure 103 Radial magnetic field with termination cone close to optimum angle for 8.5-m full-scale height.

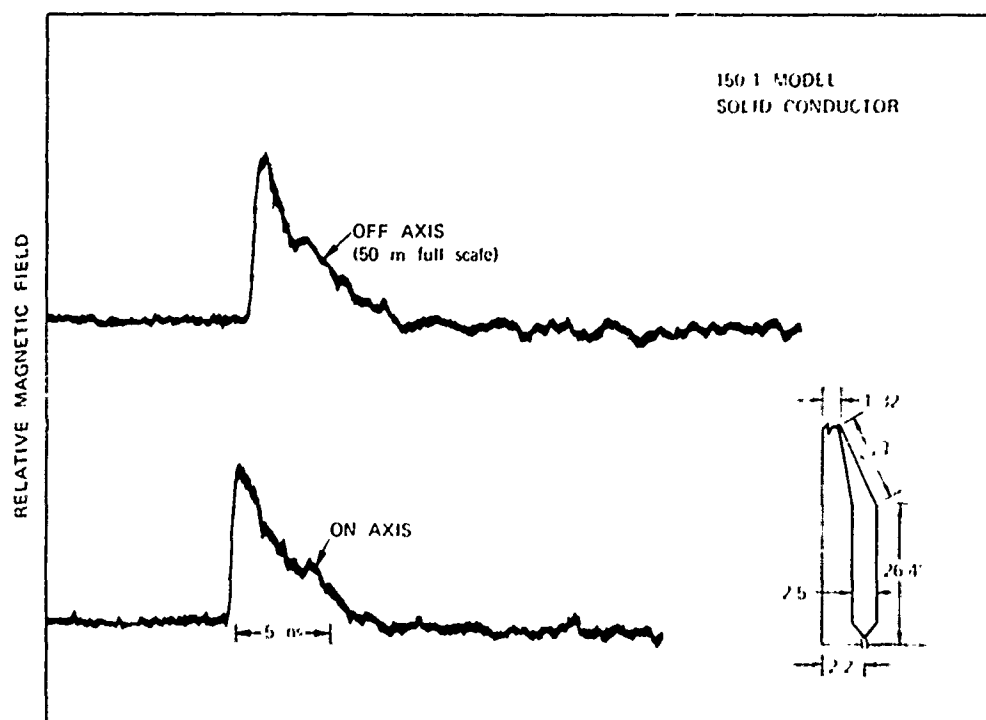


Figure 104 Radial magnetic field from a capacitively fed TEMPS at 8.5-m full-scale height.

A.3.3 Wire-Cage Studies. Since it is impractical, because of weight and other considerations, to make the LTA out of sheet metal, the conducting material will be a cage of wires. There are three major questions that then need to be answered from the electrical point of view:

- (a) How is performance affected by the number and diameter of the wires?
- (b) Do the hoops that support the wire need to be made of dielectric?
- (c) How is performance affected by the fact that the wires are not all parallel to each other and to the ground. That is, what is the effect of wire sag?

Effect of Wire Number and Diameter. The number of wires that are required to make a cage of wires appear as a solid tube of given radius can be estimated from an equation given by Schelkunoff and Friis (Reference A-3)

$$r_{\text{eff}} = r_c \left[ \frac{nr_w}{r_c} \right]^{1/n}$$

where

$r_{\text{eff}}$  = effective radius of the cage

$r_c$  = radius of cage

$r_w$  = radius of wire

$n$  = number of wires

This approximation was derived from a formulation for biconical antennas made of conical wires. The above equation is the asymptotic solution when the wires are thin and the bicone angle is small. It should give a fair estimate of effective radius for cylindrical structures with cylindrical wires.

The above equation has been plotted by B. Gaston of Physics International in a manner useful for estimating performance. This is shown in Figure 105.

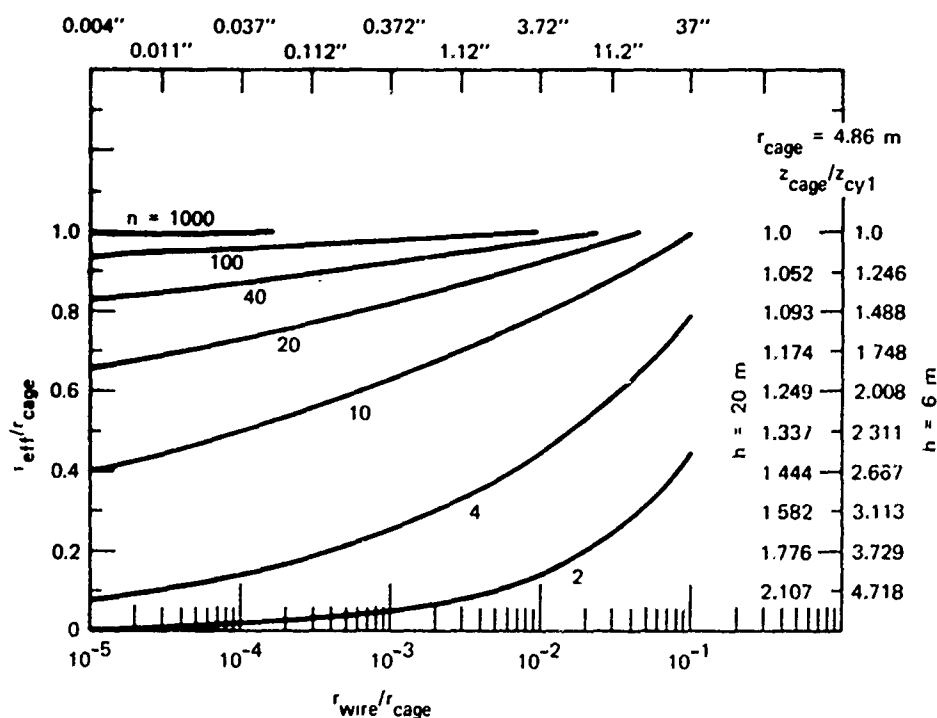


Figure 105 Effective cage radius as a function of wire-to-cage radius.

The abscissa shows the ratio of the wire radius to cage radius. It also shows the wire diameter for a 31-foot-diameter cage, which is approximately the TEMPS LTA diameter. The left-hand ordinate shows the ratio of effective radius to cage

radius. The parameter on the curves is the number of wires. The right-hand ordinate shows the ratio of the characteristic impedance of a cage of wires to the characteristic impedances for a solid conductor at two heights above a perfect ground--20 and 6 meters.

The use of this figure can be illustrated as follows. For a wire diameter of 0.112 inch and 40 wires in the cage, the left-hand ordinate indicates that the effective radius is 0.89 of the cage radius. According to the right-hand ordinate, this would increase  $Z_0$  by 1.055 at a height of 20 meters and by 1.25 at 6 meters.

Since the magnetic field is inversely proportional to the characteristic impedance, an increase of  $Z_0$  because of a small number of wires will produce a decrease in magnetic field. Using about 40 wires will keep the change in  $Z_0$  reasonably small. Increasing the number significantly above 40 improves performance only marginally, while using fewer wires (say, 10) degrades performance markedly.

The effect of wire diameter is rather weak when  $n \approx 40$ . For  $n \approx 40$  and a wire diameter of 0.037 inch,  $r_{\text{eff}}/r_{\text{cage}} = 0.82$ , while increasing the wire diameter to 0.37 inch only increases  $r_{\text{eff}}/r_{\text{cage}}$  to 0.92.

Based on considerations of this sort a wire diameter of about 1/8 inch and a wire number equal to 36 was chosen as satisfactory for the LTA.

These calculations were checked by several measurements on a 50:1 wire-cage model. TDR data were taken on models made of 14 wires, 40 wires, and sheet metal (solid cage). The wire diameter was 5 mils (1/4-inch full-scale). The data for a 40-wire model at a height of 6.6 inches (8.5 meters full-scale) are shown in Figure 106. The spike at about 3 nsec from the start of the trace marks the time when the pulse moved from the feed cable onto the bicone. The lead inductance gives us inductive reactance that is negligible in about 0.5 nsec. The monocone impedance was measured at about 64 ohms and remains at that level for about 1 nsec which is the time corresponding to

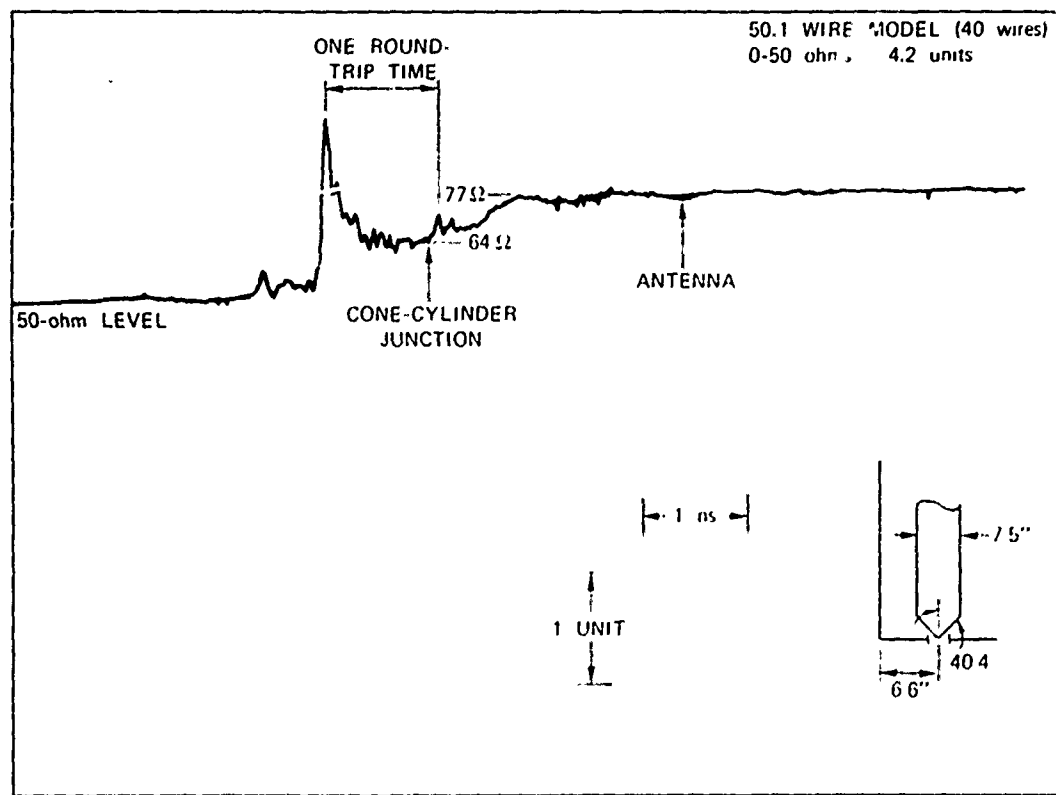


Figure 106 TDR data with 40-wire model at 8.5-meter full-scale height.



the round-trip slant distance along the cone. At about 1.1 nsec a small increase in reflection coefficient occurs. This is the time at which the pulse reflection from the cone-cylinder transition occurs and also the time at which ground interaction occurs. There is a leveling off in the reflection coefficient after about 1.8 nsec after the pulse entered the moncone. The impedance inferred from the TDR at this time is about 77 ohms. This may be compared to 70 ohms for the solid cylinder. A 40-wire cylinder increased the impedance by 10 percent. The results for the other spacings and numbers of wires are shown in Figures 107 through 109.

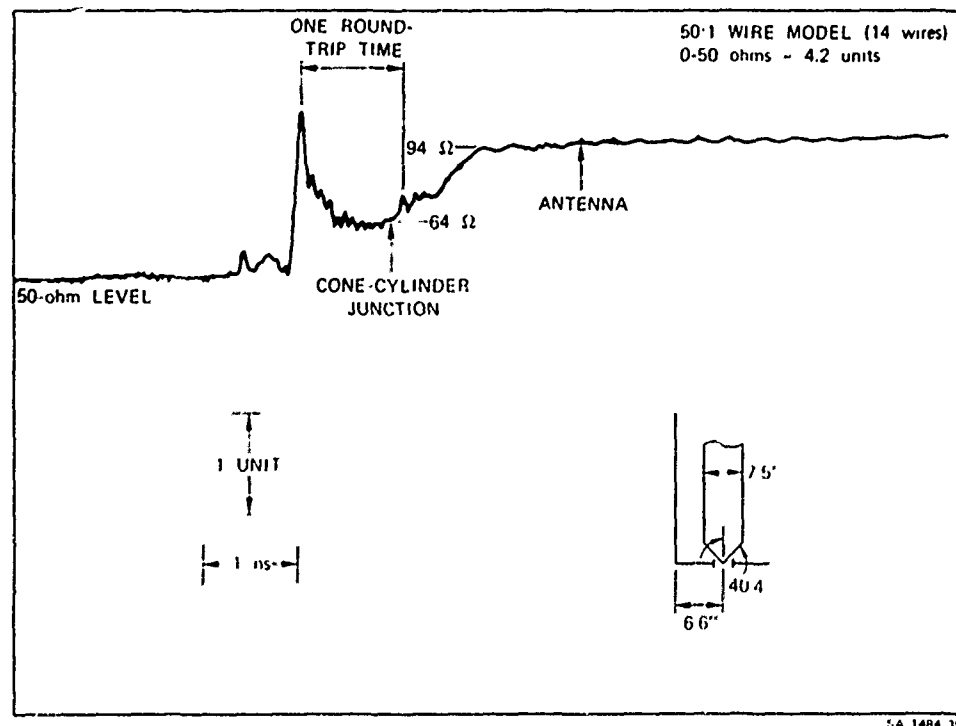


Figure 107 TDR data with 14-wire model at 8.5-meter full-scale height.

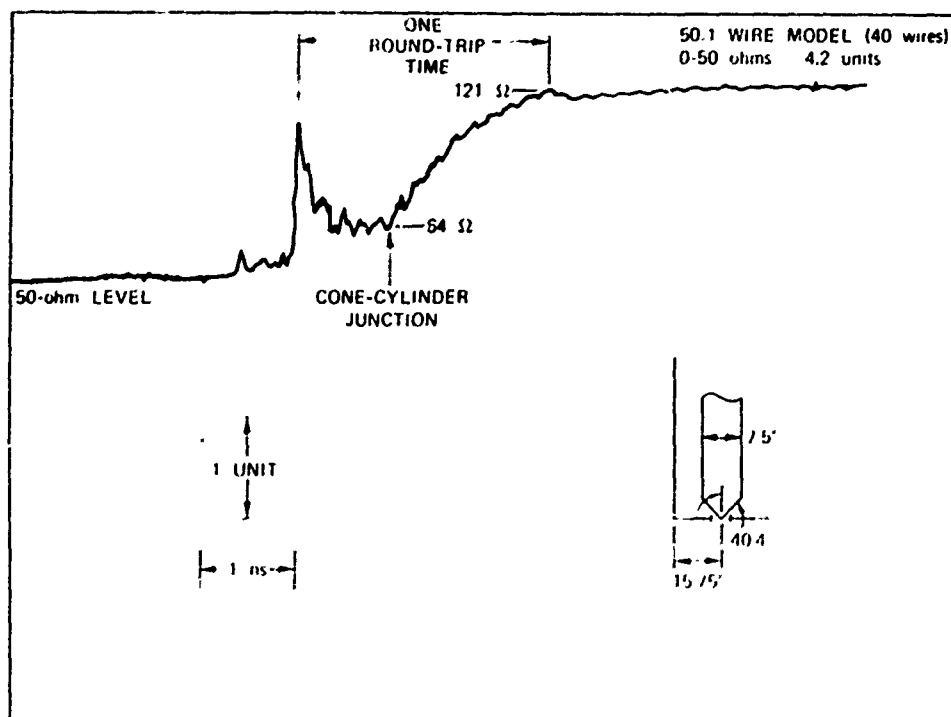


Figure 108 TDR data with 40-wire model at 20-meter full-scale height.

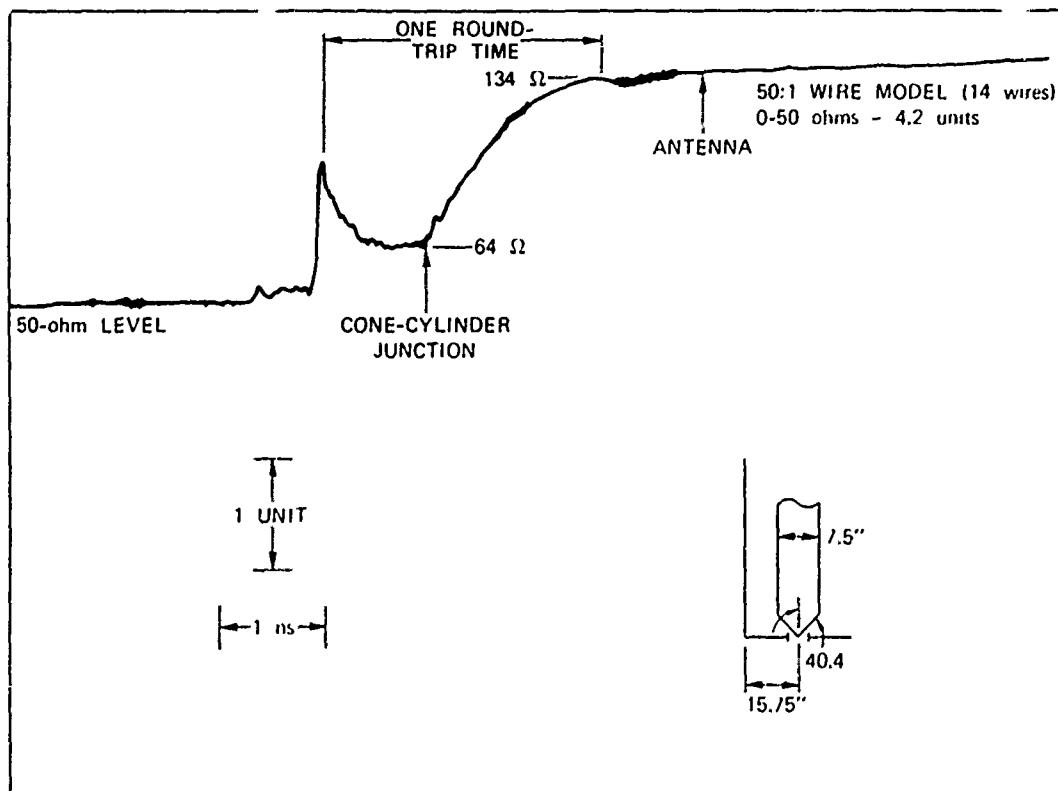


Figure 109 TDR data with 14-wire model at 20-meter full-scale height.

The measured impedances are summarized in Table X and are from data after 7 nsec. The calculated and measured impedances agree to within  $\pm 4$  percent.

At the knee of the TDR data, which is at about one round-trip time after the pulse flows onto the cone, the impedance is within about 10 percent of the late-time impedance.

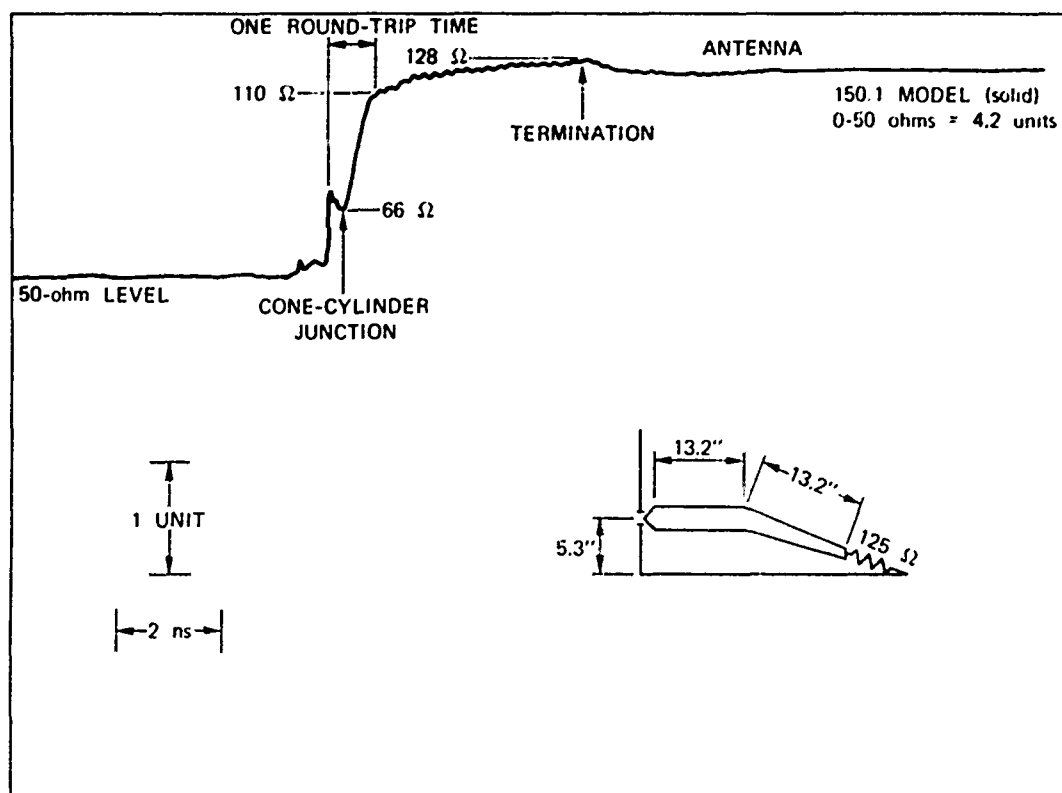
Figure 110 illustrates TDR data from a terminated 150:1 model.

The effect of a wire-cage structure as compared to a solid-metal structure on the radial magnetic field was also studied. In order to separate the discontinuity at the cone-cylinder transition from the effect of the wire-cage structure, a solid structure was made with 2 feet of solid conductor extending beyond the cone-cylinder transition. At this point the wire cage was added. The sketch in Figure 111 illustrates the geometry. This figure also shows the radial magnetic field off-axis at a full-scale distance of 50 meters from the feed point. At about 0.8 nsec after the peak signal, the ground-reflected signal increases the current on the structure. For a uniform solid cylinder this level would continue indefinitely. However, at about 3.5 nsec after the peak the signal from the junction of solid metal and wire cage arrives at the sensor. The magnetic field smoothly decreases to a level about 30 percent below the solid-metal level. The increase in impedance is about 25 percent. No terminating cone was used in this experiment. The end of the wire cage is noted.

TABLE X

## MEASURED AND CALCULATED IMPEDANCES OF CYLINDRICAL STRUCTURES

Spacing (inches)	Number of Conductors	% <sub>meas</sub>	% <sub>calc</sub>	$\frac{\%_{meas}}{\%_{calc}}$	$\left(\frac{\%}{\%_{solid}}\right)_{meas}$
6.6	Solid	69.5	70	0.99	1.0
6.6	40	79.5	76.4	1.04	1.15
6.6	20	86	85	1.01	1.24
6.6	14	96	92.9	1.03	1.38
15.75	Solid	124	127	0.98	1.0
15.75	40	128	132.4	0.97	1.03
15.75	14	146	150	0.97	1.17



SA 1484 J4

Figure 110 TDR data on terminated TEMPS model.

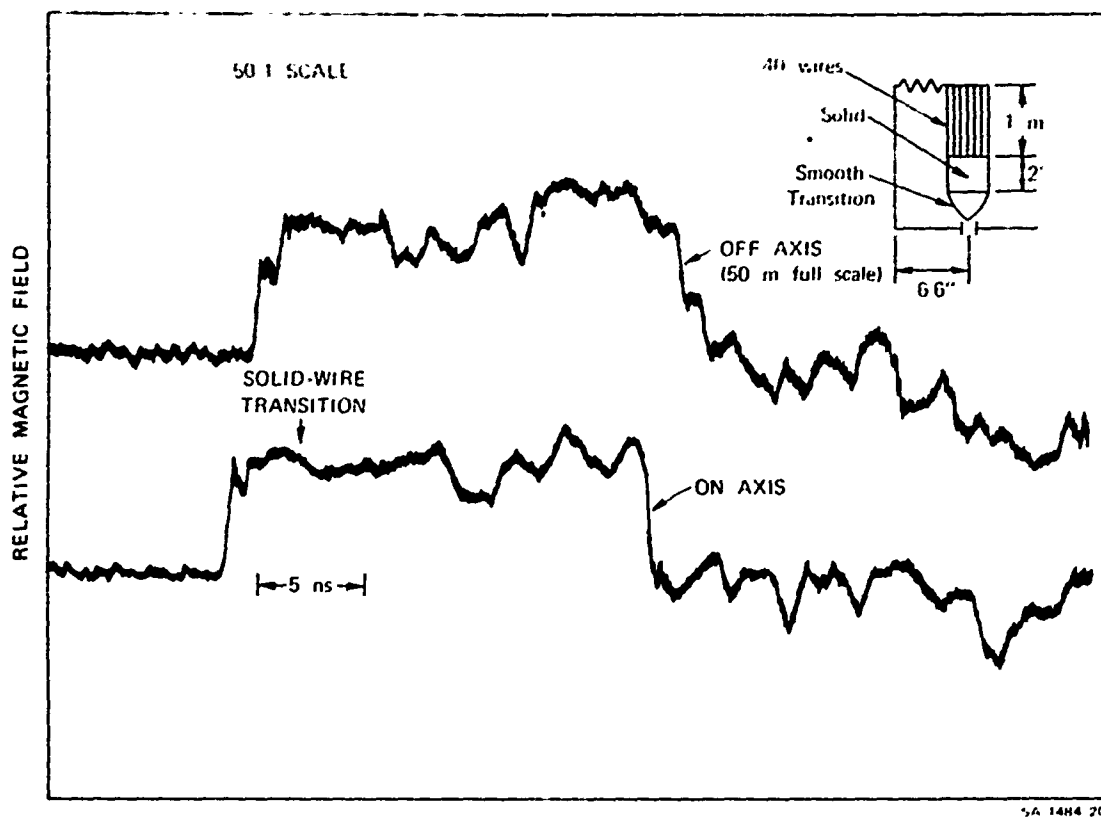


Figure 111 Effect of solid-metal-to-wire transition on radial magnetic field.

Similar data with different numbers of wires and spacings showed similar results. The decrease in magnetic field was approximately equal to the increase in impedance.

Effect of Wire Rings. The wire-cage structure is supported on hoops. If the hoops could be made of metal they would be much lighter and simpler to fabricate than if they were made of dielectric. Modeling studies were carried out to determine if a metal hoop produced significant changes in the radial magnetic field.

Fields were measured when the 40-wire cage sections were pulsed, both with no metal hoop and with a metal wire modeling the hoop attached around the circumference of the cage half-way along its length. No differences were discernible that were above the noise level of the system (differences less than  $\sim 5$  percent could not be detected).

To further emphasize any possible effect, the wire modeling the hoop was inclined at a 45-degree angle to the cylinder axis and wrapped around the wires at that angle. Once again, no differences were detectable.

As a final check, data were taken with two wire cages butted together. Each cage was constructed of solid brass end plates between which the wires were strung. Thus, at the junction of the two sections, two solid plates were present.

The geometry is shown in Figure 112, as well as the radial magnetic field on axis at a full-scale range and height of 50 meters and 8.5 meters, respectively. The time at which signals from the junction of the brass plates occur is noted. At this time there is a variation of about 5 percent. At much later times ( $\sim 10$  nsec after peak) the signal fluctuates somewhat more, but these fluctuations have been traced to reflections from the edges of the ground plane and are not connected with the junction effect.

Also shown are the data at a full-scale height of 20 meters. The effect of the junction is not discernible. It is thus concluded that metallic hoops greater than 6 inches in cross section can be used to support the wire without significantly affecting the performance.

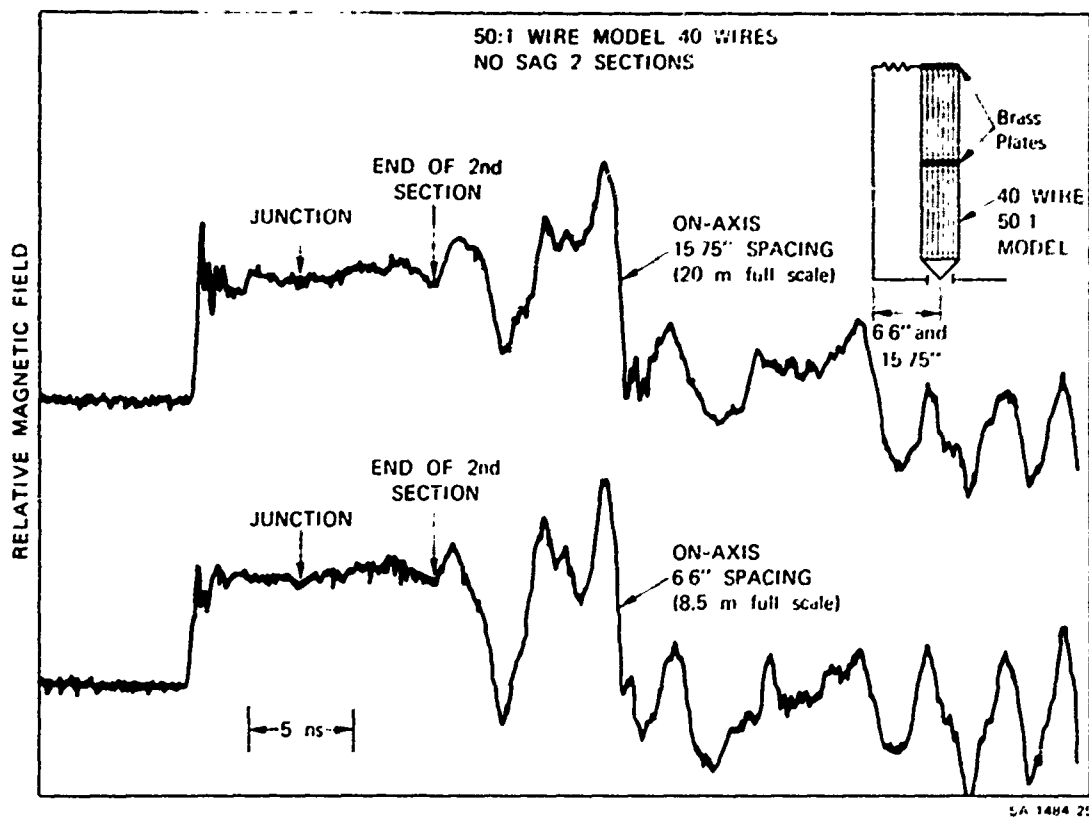


Figure 112 Effect of brass plates on radial magnetic field of wire model.

Effect of Wire Sag. In any field installation the wires will not all run parallel to the ground, but will sag between the supports so that the distance of the cage to ground will vary, being a minimum at the midpoint between supports. This has several effects. Lowering the antenna-to-ground spacing lowers the impedance, increasing the current and magnetic field. Changing the impedance produces reflections that will reduce the magnetic field. Lowering the center of radiation (local height above ground) reduces the radial magnetic field at the ground. Sloping the antenna with respect to ground introduces a vertical component of current that produces azimuthal magnetic fields that will in general be detected at radial magnetic-field sensors.

Between two supports the variation of impedance is quite smooth, decreasing as the midpoint is approached and increasing as the second support is approached. However, at the second support a cusp is formed by the incoming and outgoing wires. This produces a sharp change in the field distribution, which produces a sharp change in magnetic field.

These effects have been studied using the 50:1 model with 40 wires. Sag was simulated by tying the 40 wires to a polyfoam spacer (same diameter as cage) with a nylon string at the midpoint, and then displacing the spacer toward the ground plane. Measurements were made with displacements up to 2 inches (8.3 feet full scale). The distortion of the waveform due to the many effects can be seen most clearly by comparing Figure 112 (no sag) with Figure 113(2-inch sag).

After about 1-1/2 nsec from the peak signal, the magnetic field of the sagging model increases. After another nanosecond the signal begins to decrease monotonically to a level below the original level. This continues until the wave reaches the junction between the two wire-cage sections. At this time there is a rapid increase in the signal to about the original level.

A plausible account of the above behavior would be as follows. The increase at 1.5 nsec is due to the lower impedance and vertical current component. After the wave passes the midpoint, the impedance increases and the vertical component of current flows in the opposite direction. This decreases the field. It appears that the vertical component of current is the dominating effect since the other effects (varying impedance and changing height) almost cancel each other. Finally, the discontinuity of the conductors at the junction produces a new source of radiation that increases the field.



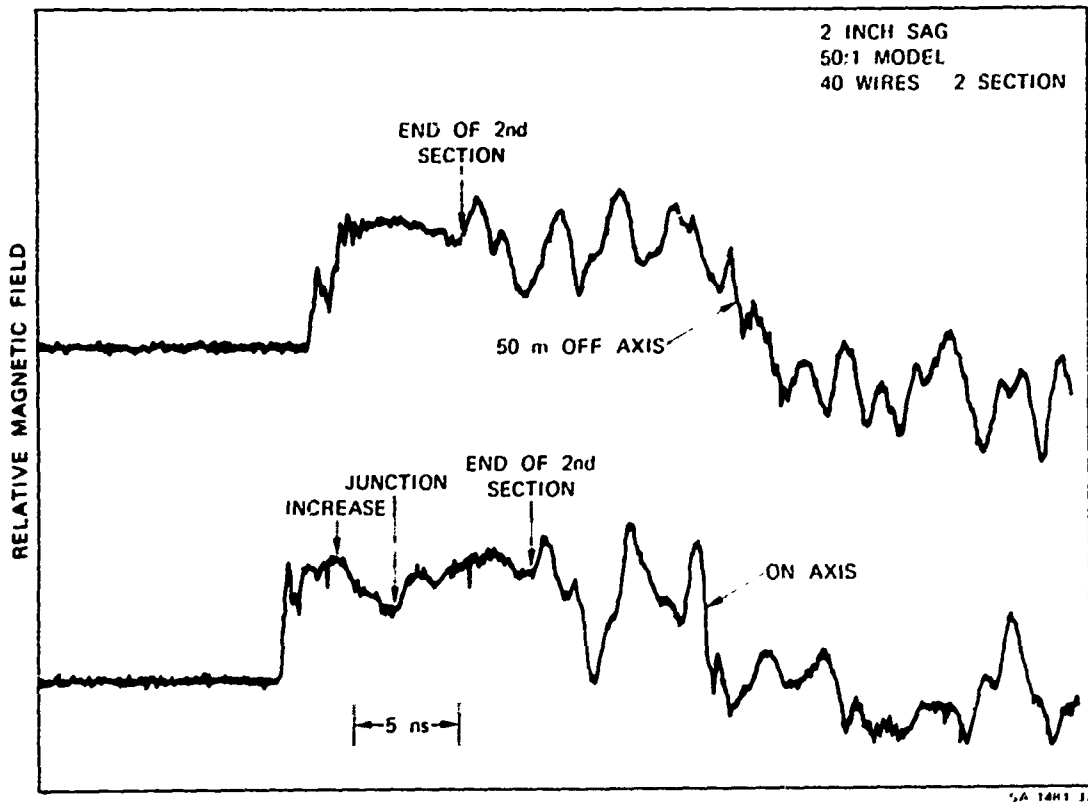


Figure 113 Effect of sag on radial magnetic field.

Data such as shown in Figure 113 were taken at sags of 0 to 2 inches in 0.5-inch steps. The behavior was similar but became less pronounced as the sag was diminished. As an index of the distortion we have plotted the percentage change from the increased signal ( $t \approx 2.5$  nsec) to the minimum signal at about 5 nsec in Figure 114. This change increases rather linearly with sag over the range of the measurements. If the sag is held to less than 2 feet, the change is about 10 percent. Since the signal increases and decreases about the same amount relative to the no-sag case, the deviation from the no-sag case is about one-half the values in Figure 114. It is therefore recommended that sag be held to less than 2 feet.

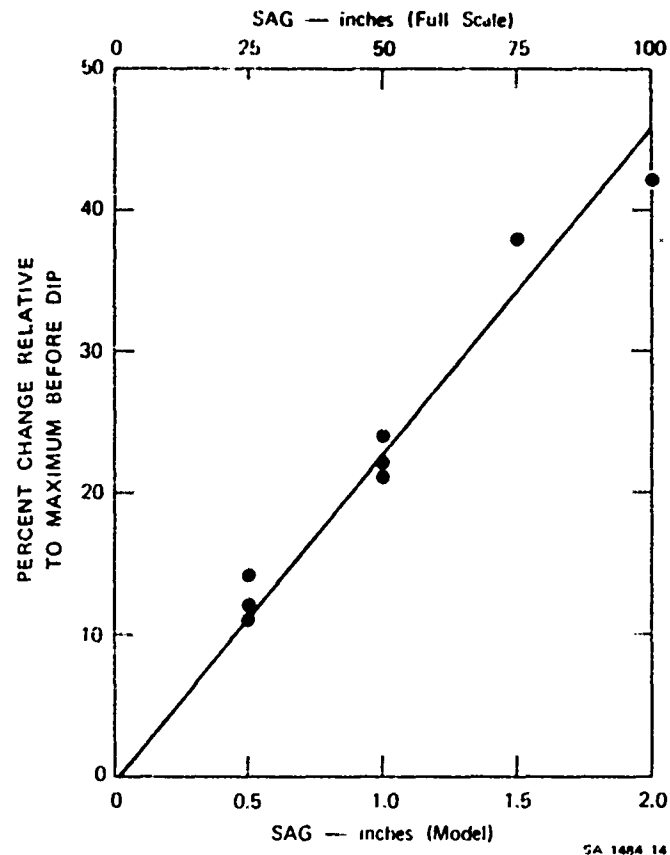


Figure 114 Percentage change in waveform as a function of wire sag.

As with many other phenomena, the effects of sag decrease with increasing antenna-to-ground spacing.

**A.3.4 Grounding Studies.** All the measurements up to this point had been made over an aluminum ground plane. Terminating the antenna in its characteristic impedance involved soldering a resistor from the end of the antenna to a lug on the ground plane. Over real earth this will not be so simple. It will be necessary to construct a ground system of conductors that will provide a sufficiently low-impedance path into the soil so that the currents will flow into the earth with only a small reflection.

Impedance of a Single Ground Rod. A common type of ground consists of a number of conducting pipes driven into the ground and connected in parallel. In order to estimate the impedance of such a ground system we shall first calculate the impedance of a single rod of radius  $a$  driven  $d$  meters into the ground. The treatment is derived by Vance (Reference A-4).

When  $\sigma/\omega\epsilon \gg 1$  for the soil, the rod and soil form a coaxial line with inner conductor equal to the rod radius and outer radius equal to the skin depth  $\delta$ , with

$$\delta = \frac{2}{\omega\mu\sigma}^{1/2}$$

where

$\omega$  = radian RF frequency

$\mu$  = permeability

$\sigma$  = conductivity

The complex characteristic impedance of this line is

$$Z_{os} \approx \frac{1}{4\sigma\delta(1+j)} \left[ 1 + j \frac{4}{\pi} \ln \frac{0.79\delta}{a} \right]$$

$|Z_{os}|$  is proportional to  $1/\sigma^{1/2}$ , since the variation in the logarithm term is very slow. Note that  $Z_{os}$  is complex.

The input impedance of this line, considering that it is open-circuited beyond the rod length, is

$$Z_{in} = Z_{os} \coth \Gamma d$$

where

$$\Gamma = \frac{1 + j1}{\delta}$$

The line is lossy such that when  $d/\delta \geq 1$ , any reflections from the open end are damped out by the time they reach the input. Mathematically,

$$\coth \Gamma d \approx 1 \text{ if } d/\delta \geq 1$$

and

$$Z_{in} = Z_{os} \text{ independent of } d$$

When  $d/\delta \ll 1$ ,

$$|\coth \Gamma d| = 0.7 \frac{\delta}{d}$$

and the phase angle of  $\coth \Gamma d$  is -45 degrees. Then,

$$Z_{in} = \frac{0.175}{\sigma d} \left[ \frac{4}{\pi} \ln 0.79 \frac{\delta}{a} - j \frac{1}{4} \right]$$

The input impedance under these conditions varies as  $1/\sigma$  and is an inverse function of length. For most cases of interest the real part is much larger than the imaginary part.

The magnitude of  $Z_{in}$  has been calculated for a 1-inch-radius rod of length equal to 2, 4, and 8 meters, and for  $\sigma$  equal to  $10^{-2}$ ,  $10^{-3}$ , and  $10^{-4}$  mho/m. The results are shown in Figure 115. The rather horizontal portions of the curves at lower frequencies correspond to  $d/\delta \ll 1$  and mostly real impedances. The curves, increasing with frequency to about the one-third power, correspond to  $d/\delta \gg 1$  and have significant real and imaginary components of impedance. It should be noted that these curves are applicable only when  $\sigma/\omega\epsilon > 1$ . These regions are indicated for each value of conductivity.

The total terminating impedance (resistors and grounding system) should equal 70 ohms at a height of 8.5 meters and about 130 ohms at a height of 20 meters. It can be seen from Figure 115 that for the poorer soils ( $\sigma < 10^{-3}$  mho/m) the impedance of a single rod will be too high unless rods longer than 8 meters are used. Even at  $\sigma = 10^{-2}$ , a single rod would have a significant impedance compared to 70 ohms. It is then clear that a multiple-rod system will be required for most soils.

The curves of Figure 115 were checked experimentally for two values of  $\sigma$ , using soil that had been salted to give a conductivity of 0.3 mho/m and unsalted soil ( $\sigma = 4 \times 10^{-2}$  mho/m). At a 150:1 scale factor, these conductivities correspond to a full-scale  $\sigma = 2 \times 10^{-3}$  mho/m for the salted soil and  $2.7 \times 10^{-4}$  mho/m for the unsalted soil. TDR data were taken with the 150:1 model TEMPS terminated in the 1/16-inch-diameter rods. Rod lengths of 1 to 4 inches (3.8 to 15 meters full-scale) were used to terminate the structure in the salted soil. The structure was fed from a broadband balun, which transformed the

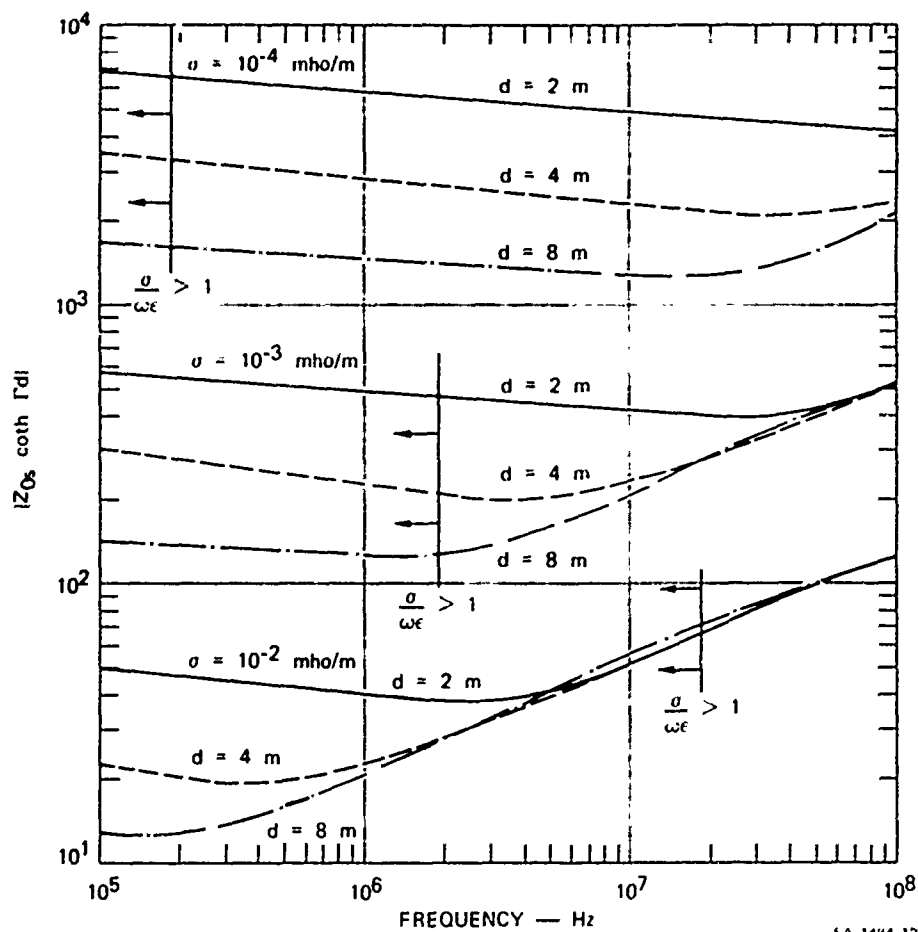


Figure 115 Magnitude of single-ground-rod impedance.

source impedance from 50 to 200 ohms. The data were used to compute the value of the load impedance. At 3 nsec after the signal reached the termination, the data had reached a rather steady level. The data at this time imply a resistance that varied from 107 to 64 ohms as the rod length increased from 1 to 4 inches. The calculated impedance for these rod diameters (9.3 inches full-scale) and lengths varied from about 80 to 60 ohms at the corresponding times. This is quite good agreement.

Over the unsalted soil, rod lengths of 1 to 8 inches were used although only the data for 4- and 8-inch lengths are reliable because of shunting effects of the balun. When the load impedance became large compared to 200 ohms, the balun shunted the load impedance significantly. An 8-inch rod (30 meters full-scale) indicated a resistance of about 75 ohms. The calculated value was about 88 ohms, which again is in quite good agreement. This may be fortuitous since, under these conditions,  $\sigma/\omega\epsilon < 1$  and the analytical model does not apply. Nevertheless, the calculations provide a good starting point for estimating what the ground-system configuration should be.

Since driving rods many meters into the ground may be difficult, an alternative technique was investigated. A rod buried horizontally many radii below the surface will have almost the same impedance as a rod driven vertically into the ground (Reference A-5). Since the rod radii will be about an inch, this would mean that a trench a foot or two deep would be sufficient for obtaining the same impedance as from the vertical rods.

Measurements similar to those described above but with the rod buried about 1/4 inch (~ 1 meter full scale) showed that a horizontal rod buried many radii did give approximately the same impedance as a vertical rod of the same length. The minimum depth used was 1/4 inch, simply because shallower depths were difficult to work with. The shallower soil did not make good contact with the rod and was non-uniform in conductivity because of different moisture content. At full-scale these problems will not be so severe, and 1-to-2-foot depths may be practical.

Termination-System Design for Specific Conductivities. We shall now describe the design procedure for the termination system for specific conductivities. Assume that Figure 115 is applicable for all cases and that the impedance of the ground system of horizontal rods is the same as for vertical rods. We shall first take the case of the TEMPS at a height of 20 meters ( $Z_0 = 130$  ohms).

a. 20-Meter Antenna Height

1)  $\sigma = 10^{-2}$  mho/m. In this case, for the sort of rod length that will be required, the ground impedance will be  $Z_{OS}$  with a magnitude as given in Figure 115. This impedance is a function of frequency and has approximately equal real and imaginary parts. At the highest frequencies,  $|Z_{OS}| = 120$  ohms. In order to use the minimum number of ground rods we shall calculate the reflection coefficient for different values of terminating resistor and ground impedance to find the highest value of ground impedance that will keep the reflection coefficient below 0.2. For this case,

$$\Gamma = \frac{Z_T + \operatorname{Re}|Z_{OS}| - Z_0 + j \operatorname{Im}|Z_{OS}|}{Z_T + \operatorname{Re}|Z_{OS}| + Z_0 + j \operatorname{Im}|Z_{OS}|}$$

where

$$\operatorname{Re}|Z_{OS}| = \operatorname{Im}|Z_{OS}| = Z_g$$

$$\operatorname{Re}|Z_{OS}| = \text{real part of characteristic impedance}$$

$$\operatorname{Im}|Z_{OS}| = \text{imaginary part of characteristic impedance}$$



Normalizing with respect to  $Z_0$ ,

$$\Gamma = \frac{\left( \frac{Z_T + Z_g}{Z_0} - 1 \right) + j \frac{Z_g}{Z_0}}{\left( \frac{Z_T + Z_g}{Z_0} + 1 \right) + j \frac{Z_g}{Z_0}}$$

The value of  $|\Gamma|$  was computed for different values of  $Z_T/Z_0$  and  $Z_g/Z_0$ . The highest value of  $Z_g/Z_0$  that resulted in  $|\Gamma| \leq 0.2$  was  $Z_g/Z_0 = 0.4$ . This occurred for  $Z_T/Z_0 = 0.8$  and was rather insensitive to variations of a few tenths in this ratio. If  $Z_g/Z_0$  is made 0.4 at the highest frequency, then as frequency decreases, both  $Z_g/Z_0$  and  $|\Gamma|$  decrease. For  $Z_0 = 130$  ohms,  $Z_T = 104$  ohms (terminating resistance) and  $|Z_{os}| = 73$  ohms. Since  $|Z_{os}| = 120$  ohms at the highest frequency, a system of two ground radials will bring  $|Z_{os}| < 73$  ohms. In order to prevent day-to-day variation in  $\Gamma$  from increasing to more than 0.2, it is recommended that three radials be used. This will make the design  $|\Gamma| = 0.15$  and allow  $\sigma$  to decrease approximately a factor of 2 without  $\Gamma$  becoming larger than 0.2.

A rod length  $> 4$  meters will ensure that the impedance stays sufficiently low at the lowest frequencies of interest.

2)  $\sigma = 10^{-3}$  mho/m. Reasoning as above, we require  $|Z_{os}| < 73$  ohms. For a conductivity of  $\sigma = 10^{-3}$  mho/m,  $|Z_{os}| = 500$  ohms at the highest frequencies. Therefore, a system of seven radials would be necessary to make  $\Gamma = 0.2$ . Ten radials would be required to give a margin of safety for day-to-day variation. As will be shown later, because of losses in the

ground, the risetime is increased, and the highest frequency is therefore decreased, by the time the wave has reached the termination. The amount of loss of high-frequency content will in general be a function of conductivity, antenna height, and length, but for the range of parameters of interest there will be a significant decrease in risetime.

Thus, for example, if the highest frequency is only 10 MHz (a reasonable number for  $\sigma = 10^{-3}$  mho/m and 150 meter antenna half-length), only five radials would be needed. The radials should be 12 to 16 meters long.

3)  $\sigma = 10^{-4}$  mho/m. For this case the calculated impedance is almost purely resistive. Bearing in mind that the calculations do not strictly apply for this case but are being used for estimations, we find that, for these conditions, the resistance decreases linearly with rod length. The division between the terminating resistor and the ground system is somewhat different for a resistive ground system. The reflection coefficient can be made zero for one assumed conductivity and will increase if  $\sigma$  varies. Thus, if  $Z_T = Z_g = 65$  ohms, then  $\Gamma = 0$ . If  $Z_g$  increases to 130 ohms, then  $\Gamma = 0.2$ . If  $Z_g$  decreases to 32.5 ohms, then  $\Gamma = -0.145$ . Thus, a factor of two in ground impedance is tolerable.

To make  $Z_g = 65$ , eight radials 20 meters in length would be required. Increasing the length will linearly decrease the number of radials and vice versa.

Although the calculations were carried out for a rod radius of 1 inch, the results are quite insensitive to this parameter. A factor-of-5 increase in the radius decreases the impedance by about 35 percent. Two-inch-wide metal braid is easily stored and unrolled, and should be an adequate substitution for rods.

The results of these calculations are summarized in Table XI.

TABLE XI  
TERMINATING SYSTEM FOR AN ANTENNA HEIGHT OF 20 METERS

$\sigma$ (mho/m)	$Z_T$ (ohms)	Number of Radials	Length of Radials (meters)
$10^{-2}$	104	3	4
$10^{-3}$	104	5	12
$10^{-4}$	65	8	20

b. 10-Meter Antenna Height. For an antenna height of 10 meters the risetime will be so degraded that we will take 10 MHz as the upper frequency. The characteristic impedance is 80 ohms.

1)  $\sigma = 10^{-2}$  mho/m. Proceeding as before, we let  $Z_T = 64$  ohms. For  $Z_g/Z_o = 0.2$  (which includes a safety factor of 2),  $|Z_g| = 16$  ohms and  $|Z_{os}| = 22.5$  ohms. The three-radial systems used at 20 meter height will be adequate to keep  $|\Gamma| < 0.2$  for frequencies up to about 18 MHz. Therefore, with the degraded risetime a three-radial system with a 64-ohm resistor will be adequate.

2)  $\sigma = 10^{-3}$  mho/m. A terminating resistor of 64 ohms, and 10 radials 12 meters long would be required to give a safety factor of two with regard to the nominal ground conductivity. Maintaining a 5-radial system at 10 meters (as is used at 20 meters) would not yield any safety factor. However, measurements for simulated earth of  $2 \times 10^{-3}$  mho/m showed that the risetime was so degraded that a two-radial system was adequate (see A.3.4, paragraph 3).

3)  $\sigma = 10^{-4}$  mho/m. A 40-ohm terminating resistor and 40-ohm ground resistor will require either sixteen radials 20 meters long or eight radials 40 meters long. Once again, a more modest ground system may be acceptable because of risetime degradation.

The results of these calculations are summarized in Table XII.

TABLE XII  
TERMINATING SYSTEM FOR AN ANTENNA HEIGHT OF 10 METERS

$\sigma$ (mho/m)	$Z_T$ (ohms)	Number of Radials	Length of Radials (meters)
$10^{-2}$	64	3	4
$10^{-3}$	64	5	12
$10^{-4}$	40	8	40

In addition to the effects of degraded risetime at the termination, another effect may make the grounding problem easier. In order to prevent corona at the end of the antenna, a minimum distance between ground and the bottom of the antenna structure of 3 meters is required. The diameter of the terminating cone at its extremity will be about 5 feet. Therefore, the local transmission line impedance will be 138 ohms. For the 20-meter height this is not much of a difference from the  $Z_0$  of the cylindrical portion. At the lower heights, though, it represents a significant change in impedance. The results of too high an impedance have been seen before in Figure 101. It tends to put a dip in the magnetic field at times associated with the increased impedance.

If the 3-meter minimum clearance is necessary, then the terminating impedance even at 8.5-meter height will be 138 ohms. This can be terminated with a resistor-ground system similar to the one outlined above for the 20-meter height. A resistor of 112 ohms instead of 104 would be more suitable. This system would be the same for all antenna heights.

Due to risetime degradation over real earth, the dip in magnetic field will be smeared out to a degree depending on antenna height and soil conductivity. Measurements to be reported later show that the dip is quite small over soil with conductivity equal to  $6 \times 10^{-3}$  mho/m and should become smaller as the conductivity becomes less.

The recommended terminating system for all heights when the terminating cone tip is held to 3-meter clearance from ground is given in Table XIII.

It has been assumed throughout this discussion that by making an N-rod system, the impedance becomes  $1/N$  times the impedance of a single rod. This will be true if the rods are separated by more than a skin depth. The skin depth is shown in Figure 116 for different conductivities. At the highest frequencies the skin depth is smallest and increases as  $f^{-1/2}$ . For conductivities of  $10^{-2}$  and  $10^{-3}$  mho/m the high-frequency impedance was highest and determined the number of rods required. At these frequencies the rods most nearly look like N rods in parallel. At lower frequencies the impedance of a single rod decreases, but the total impedance will be greater than  $Z_{\text{single rod}}/N$  since the separation will not be a skin depth. The resultant impedance will therefore not drop with decreasing frequency as quickly as was shown in Figure 115. However, since the ground system was designed to have a low enough impedance at the highest frequencies, it should be adequate at the lower ones also. Experimental measurements bear this out.

TABLE XIII

TERMINATING SYSTEM FOR 3-METER TIP CLEARANCE--ALL HEIGHTS

$\sigma$ (mho/m)	$Z_T$ (ohms)	Number of Radials	Length of Radials (meters)
$10^{-2}$	112	3	4
$10^{-3}$	112	5	12
$10^{-4}$	69	8	20

Modeling Measurements Over Real Earth. Magnetic and electric-field measurements have been made with both 150:1 and 50:1 models. The 150:1 model was a scaled-down version of the entire TEMPS (300 meter length) and was made of brass tubing. The 50:1 model included only one 50-meter cylindrical section in each antenna half so that the total length was 200 meters full scale. This model had a solid bicone and 40-wire cage for the cylinder and terminating core sections.

The conductivity was approximately 0.3 mho/m so that the full-scale conductivity for the 150:1 model was  $2 \times 10^{-3}$  mho/m and  $6 \times 10^{-3}$  mho/m for the 50:1 model.

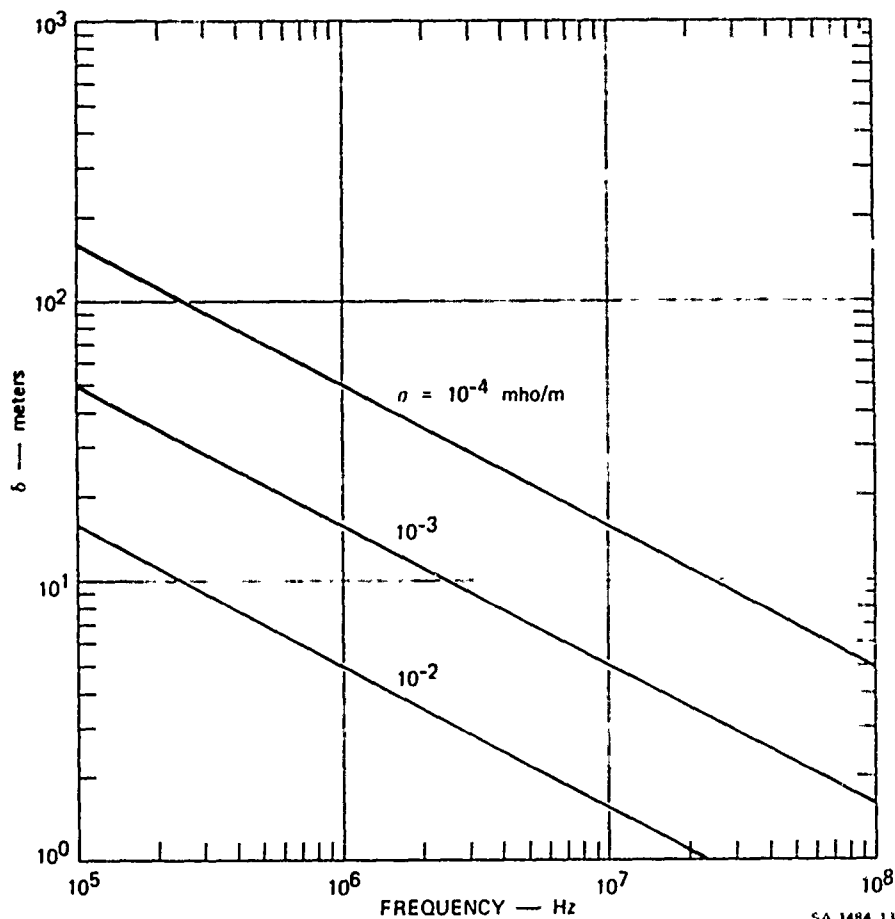


Figure 116 Skin depth as a function of frequency.

a. 150:1 Model Measurements. Measurements were made with a variety of terminating systems. Some typical data at a full-scale antenna height of 20 meters, with a ground system consisting of two radials 3 inches long (11.5 meters full-scale) and a 68-ohm resistor, are shown in Figure 117. The rise after the initial spike is due to interaction with the ground. The increased signal at about 6 nsec after the peak is due to the terminating system having too low an impedance relative to the impedance of the cone. The increase is about 20 percent. Figure 117 shows the same configuration but with a 130-ohm terminating resistor. Here the terminating impedance is too high and causes a reduction of about 20 percent. The results for a 100-ohm resistor are shown in Figure 118. Both on-axis and 50-meter off-axis fields are shown. The termination is not detectable in the waveform, indicating a very good match.

The generally decreasing amplitude with time in these figures is due to sag in the balun and sensor response.

These measured results may be compared with the calculation in Section A.3.4 for soil with conductivity equal to  $10^{-3}$ . There it was concluded that a 104-ohm resistor and five radials 12 meters long would cause reflection less than 20 percent. The measurements show that in soil only slightly better ( $\sigma = 2 \times 10^{-3}$  mho/m), two radials about 12 meters long were sufficient to make the reflection much less than 20 percent. Thus, the terminating system specified in Section A.3.4 is probably conservative. That is, fewer radials may still give adequate performance.



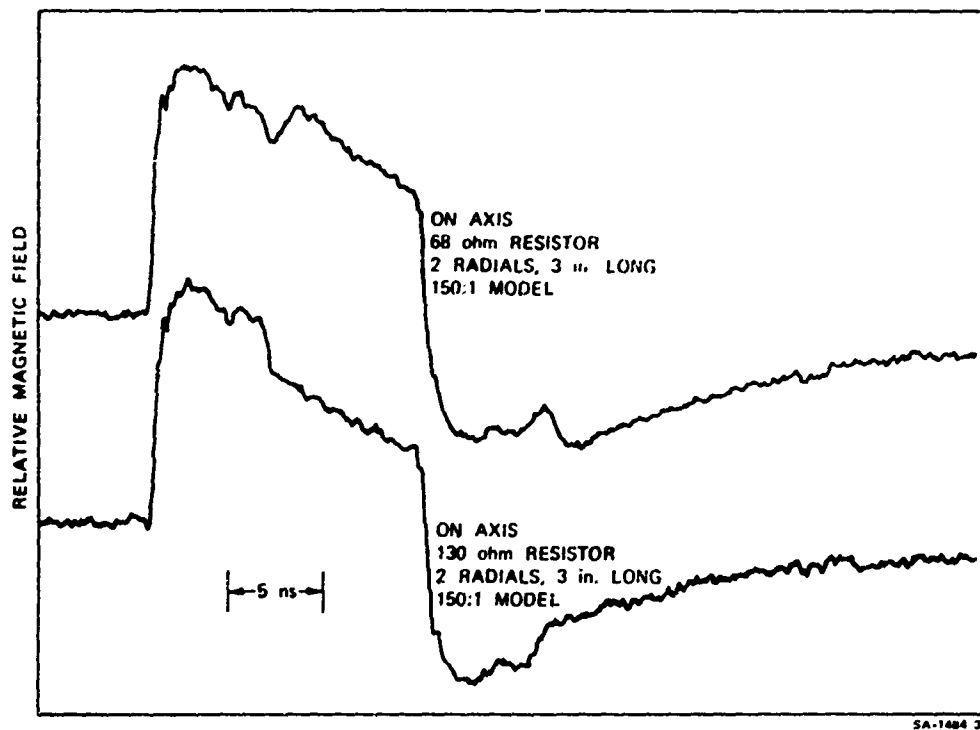


Figure 117 Radial magnetic field over real earth with incorrect terminating impedance.

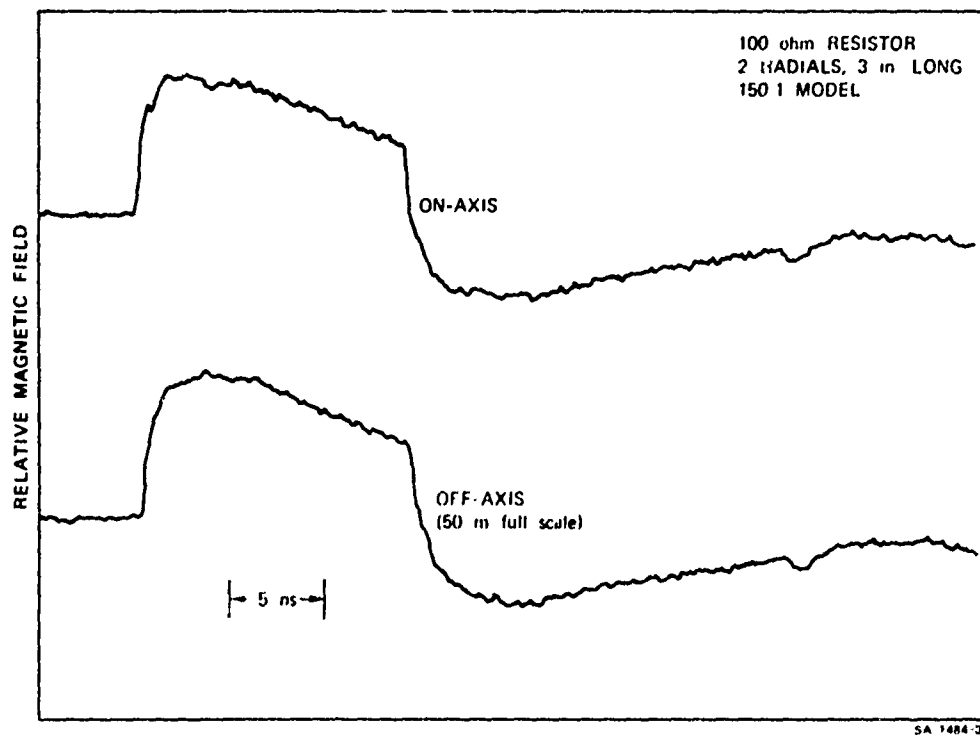


Figure 118 Radial magnetic field over real earth with correct terminating impedance.

b. 50:1 Model Measurements. Measurements were made with the 50:1 model at scaled heights of 8.5 and 20 meters. Because of the length of the model an input-pulse length of 28 nsec was used. The sag due to sensor and balun low-frequency performance produced an almost linear decay after about 15 nsec. Nevertheless the main features are still discernible--most importantly, the effect of the terminating system and the terminating-cone spacing at its tip.

Figure 119 shows the results with a 100-ohm terminating resistor and two 9-inch-long (11.3 meters full scale) ground radials. The tip spacing was about 1 meter full scale. The increase at about 5.5 nsec marks the transition from cylinder to terminating cone. It is probably exaggerated because this junction was covered over with copper tape instead of carrying the 40 wires around the bend. Any reflection from the tip should have arrived at the sensor after 11.5 nsec if the velocity was the speed of light. No change in waveform occurred at this time, indicating a very small reflection. Increasing the tip spacing to 2 meters full-scale gave the results of Figure 120. At about 11 nsec a small decrease in signal is detectable. This is associated with the increase of the impedance of the terminating cone near the end. The dip is less than 10 percent. Increasing the tip spacing to 3 meters gave Figure 121, which still shows only a small dip due to reflections from the termination. This shows that the 3-meter tip spacing will be usable over real earth of conductivity as high as  $6 \times 10^{-3}$  mho/m. It is unlikely that the dip will increase markedly for a conductivity higher by a factor of 2.

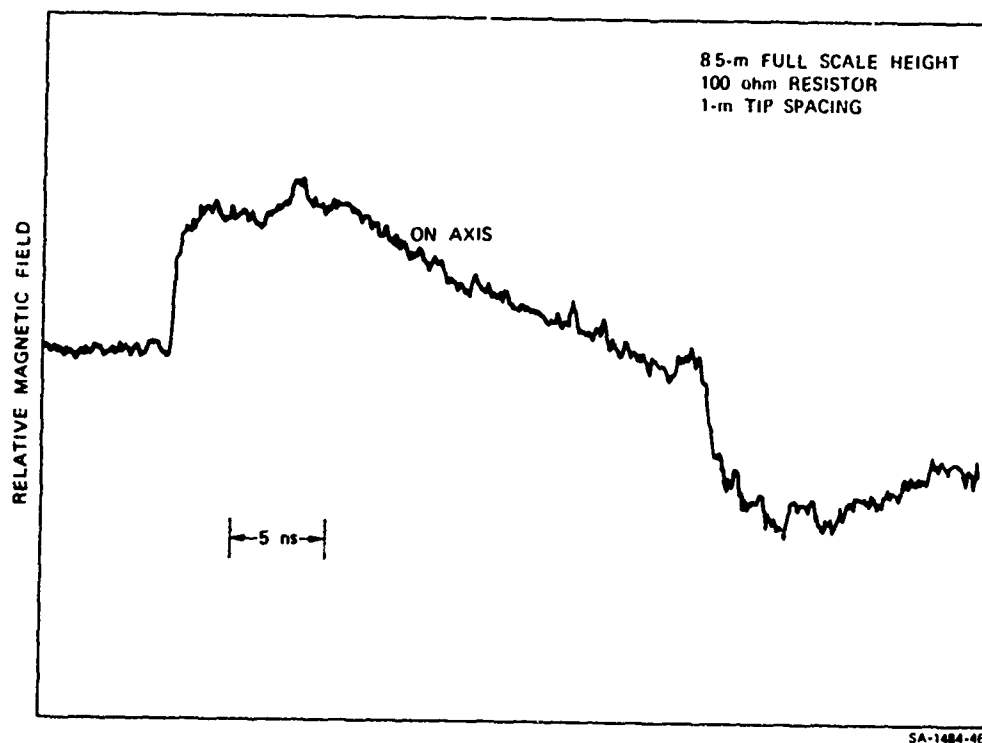


Figure 119 Radial magnetic field over real earth with 1-m tip spacing.

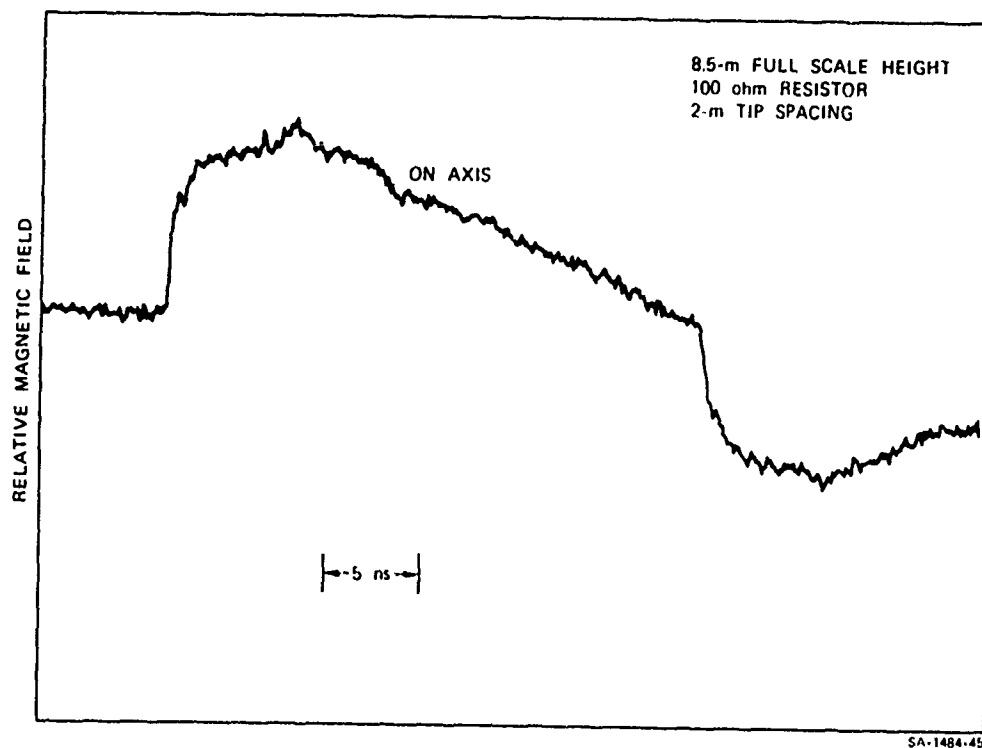


Figure 120 Radial magnetic field over real earth with 2-m tip spacing.

To illustrate how smeared the risetime becomes, a cut was taken with no termination at all. The results are shown in Figure 122. The decrease in magnetic field does not become noticeable until about 12.5 nsec, and then it takes about 4 nsec to decrease to a new level. Over aluminum ground planes the time for this decrease is much faster and is quite close to the input risetime. The earth is clearly degrading the risetime when it reaches the termination.

Vertical-electric-field measurements were also made at a full-scale distance of 50 meters from the axis and at intervals of 25 meters from the feed point. The data are shown in Figure 123. On-axis, the vertical electric field is quite small, as it should be. At 25 meters off-axis the field increases significantly to a level of about 50 percent of the maximum off-axis field. From 50 to 100 meters off-axis the amplitudes are quite uniform. The dip noted in the laboratory tests over aluminum ground planes is still there but is smoothed somewhat over real earth.

c. Current-Waveform Degradation Due to Finitely Conducting Earth. In order to study the degradation of risetime as a wave travels down a transmission line, measurements were made on a line consisting of 1/4-inch-diameter rods fed by a balun. Several rod-to-ground spacings were tried but the most marked effects were seen with a centerline height-to-radius ratio of 3. This is comparable to the TEMPS spacing. A current transformer was inserted into the line at the feed point--then at 34 inches and finally at 68 inches down the line--and the current waveform was measured. The results are shown in Figure 124. The degradation of risetime is clearly discernible.

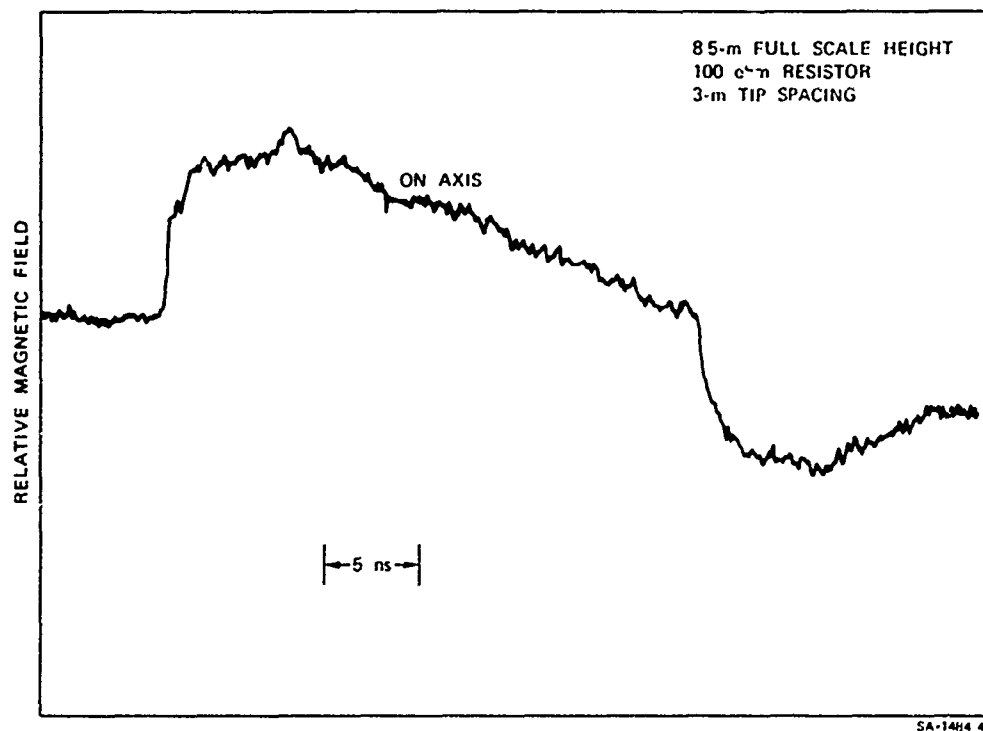


Figure 121 Radial magnetic field over real earth with 3-m tip spacing.

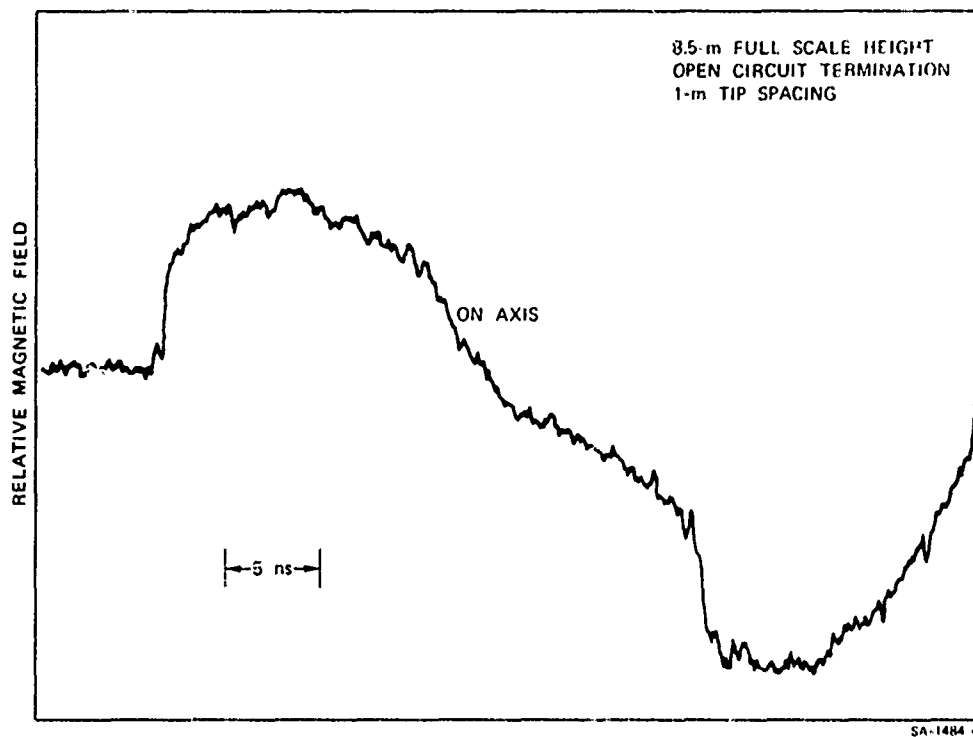


Figure 122 Radial magnetic field over real earth with no termination system.

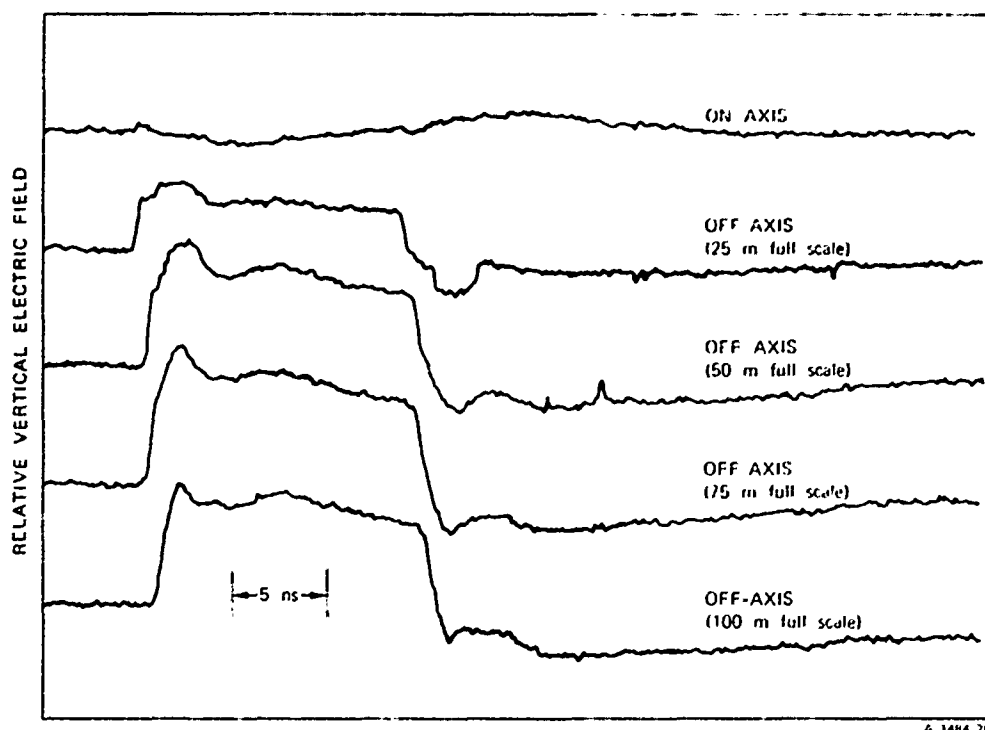


Figure 123 Vertical electric field over real earth.

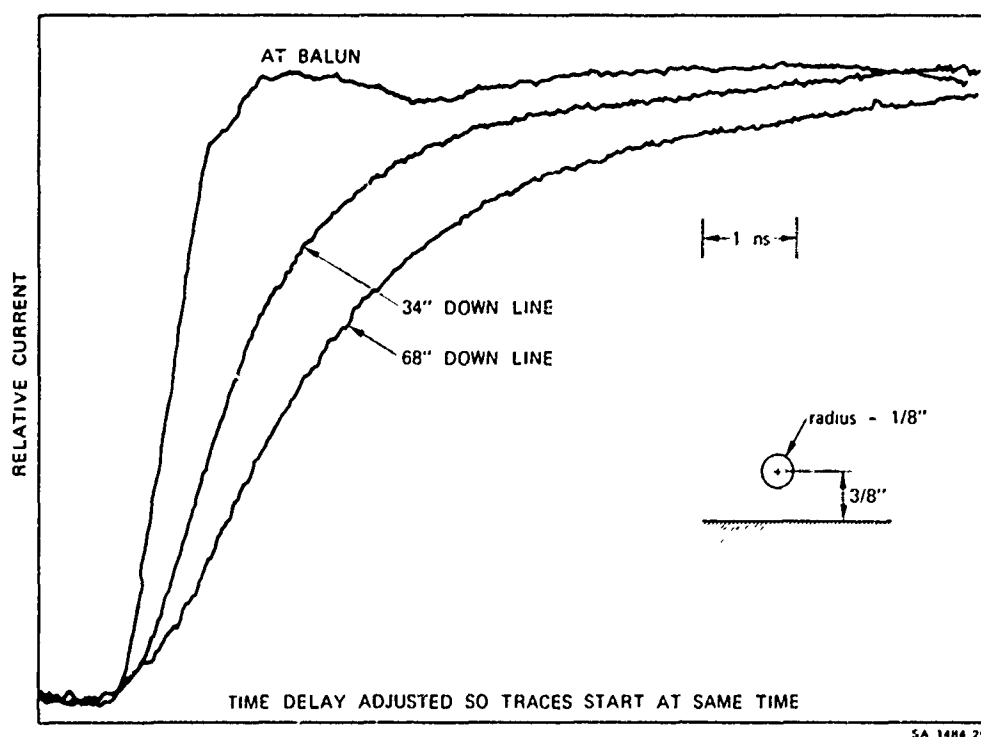


Figure 124 Current waveforms down a transmission line over real earth.

These results have been compared to some analytical results derived from Sunde (Reference A-6) so that predictions could be made of risetime at the TEMPS termination system. The analysis is given in Section A.5. The results essential for the present discussion are the risetime expressions for a step-function input. There are two regimes defined by the relation between the skin depth and the antenna height.

One regime is the case in which if  $\delta \gg 2h$ , then the normalized amplitude as a function of time, position, and rod-to-ground spacing is given by

$$P(x,t) = 1 - X \frac{1 + \left( \frac{2}{\beta_1} \frac{t_o}{\pi} \right)^{1/2}}{4v t_o \ln \frac{2h}{a}} .$$

where

$P$  = normalized amplitude

$X$  = distance from input

$v$  = velocity

$t_o = t - x/v$  (delayed time)

$$\beta_1 = \frac{\beta \beta_i}{\beta x \beta_i}$$

$$\beta = h \left( \frac{\mu_o}{\rho} \right)^{1/2} \quad \beta_i = a \left( \frac{\mu_o}{\rho_i} \right)^{1/2}$$

$h$  = transmission-line height

$a$  = transmission-line radius

$\mu_o$  = permeability

$\rho$  = resistivity of the earth

$\rho_i$  = sensitivity of the transmission-line conductor

For most cases,

$$\left( \frac{2}{\beta_1} \frac{t_o}{\pi} \right)^{1/2} \ll 1$$

so that the expression becomes

$$P(x,t) = 1 - \frac{x}{4v t_o \ln \frac{2h}{a}}$$

The time for  $P$  to go from 0 to 90 percent is given by

$$t_{90} = 500 \frac{x}{Z_o} \text{ nsec}$$

when  $x$  is in meters and

$$Z_o = 60 \ln \frac{2h}{a}$$

Note that  $t_{90}$  is independent of conductivity. For  $x = 150$  meters and an antenna height of 8.5 meters,  $Z_o = 70$  ohms and  $t_{90} = 1065$  nsec. It would take over 200 nsec for the amplitude to reach even 20 percent of its peak. Thus, if this condition holds, the risetime will be seriously degraded, making the termination easier.



The other regime is the case in which

$$\delta < \frac{2h}{5}$$

Then

$$P(x,t) = \operatorname{erfc} \left[ x \left( 4\beta_1 v t_o^{1/2} \ln \frac{2h}{a} \right)^{-1} \right]$$

where  $\operatorname{erfc}$  = complementary error function.

The amplitude reaches 90 percent when

$$t_{90} = 245 \frac{x^2 \rho}{h^2 z_o^2} \text{ nsec}$$

For  $x = 150$  meters,  $h = 8.5$  meters, and  $\rho = 10^2$  ohm-m,  $t_{90} = 1560$  nsec. The time to reach the 50 percent amplitude is about 1/29 the time to reach 90 percent so that the 0-to-50 percent time is only about 55 nsec. This is still a significant degradation in high-frequency content.

For the pulse shapes and soils of interest, neither of the two solutions will hold for all frequencies, but the waveform will vary from one solution to the other. However, both calculations show that the risetime will be appreciably degraded by the time the wave reaches the termination.

A comparison of the analytical results with the measured data of Figure 124 is shown in Figure 125. The agreement is quite good.

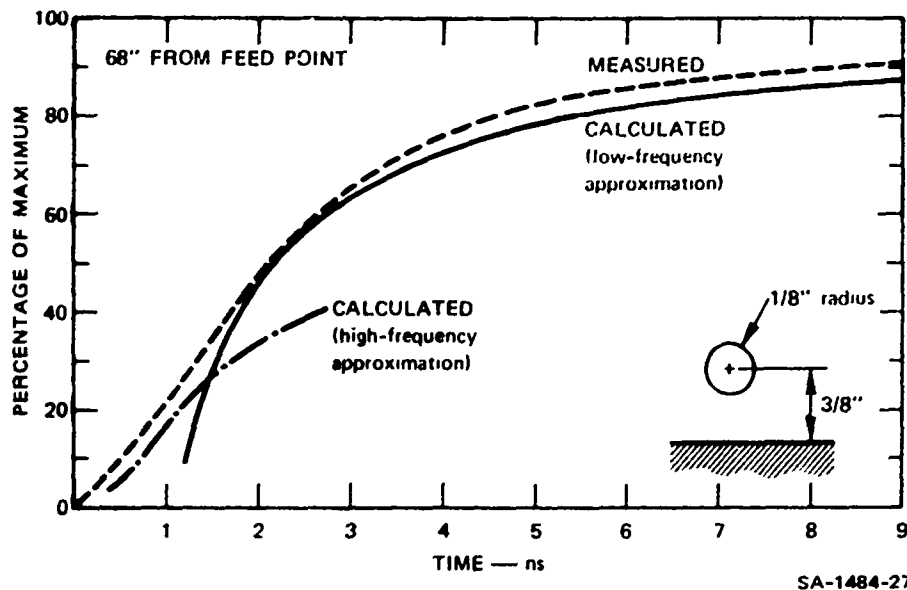


Figure 125 Comparison of calculated and measured current waveforms.

A.3.5 Rotated Polarization. One of the requirements of TEMPS is to rotate the polarization up to 15 degrees. This is equivalent to having a vertical and horizontal electric field, with the vertical field about one-quarter of the horizontal field. There is a corresponding ratio for the transverse and vertical magnetic fields.

Measurements have been made on several of the tilt configurations. These include (a) one side of the TEMPS in the horizontal position while the other side is terminated to ground through the 50-meter-long terminating cone, (b) the two terminating cones forming a tilted dipole, and (c) a bicone and portion of the cylinder (total overall length of 100 feet) tilted, with the rest of the LTA parallel to the ground at different heights on each side of the feed.

As a baseline measurement, data have been taken on a full TEMPS model in its usual configuration parallel to the ground. The data for vertical electric field are shown in Figure 126. Note that the on-axis vertical electric field is very small while the off-axis field is much larger. Its amplitude is about the right value for the vertical component of a 15-degree polarization rotation. The off-axis field has the input rise-time. There is a drop of about 25 percent when the reflection from the cylinder-terminating cone junction reaches the sensor. The H-field data do not show as marked a change at this time. The E-field signal recovers when the reflection from the junction on the other side arrives at the sensor. Over real earth this dip is smoothed somewhat. Data taken under these conditions also showed that the vertical E field was relatively uniform from 50 meters off-axis to the start of the terminating cone.

When the TEMPS was modified by attaching the terminating cone directly to the bicone the results of Figure 127 were obtained. E5 (on-axis electric field) has been increased considerably although the waveform is quite irregular. This at least produces some vertical electric field on-axis although it is still too low. The magnetic field is not significantly different than with the ordinary TEMPS configuration.

The vertical electric field for the tilted dipole made up of the bicone and terminating cones tilted at 15 degrees is shown in Figure 128. The waveform is clearly unacceptable. The magnetic fields are also highly distorted. Varying the terminating impedance changed the waveform somewhat, but in no case was it acceptable.

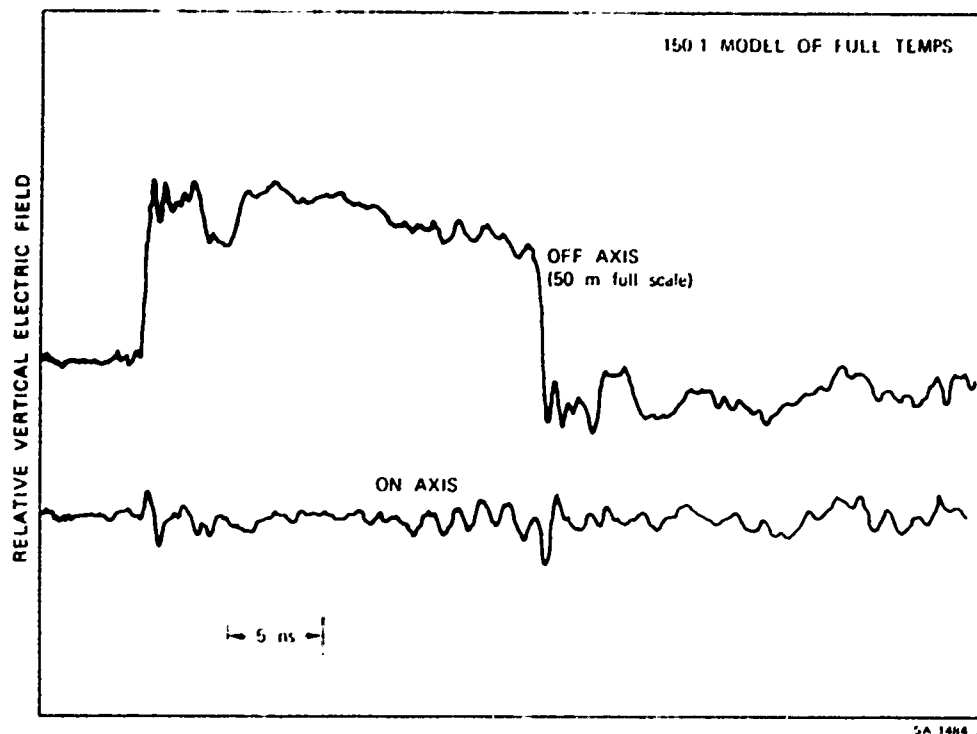


Figure 126 Vertical electric field from horizontal TEMPS.

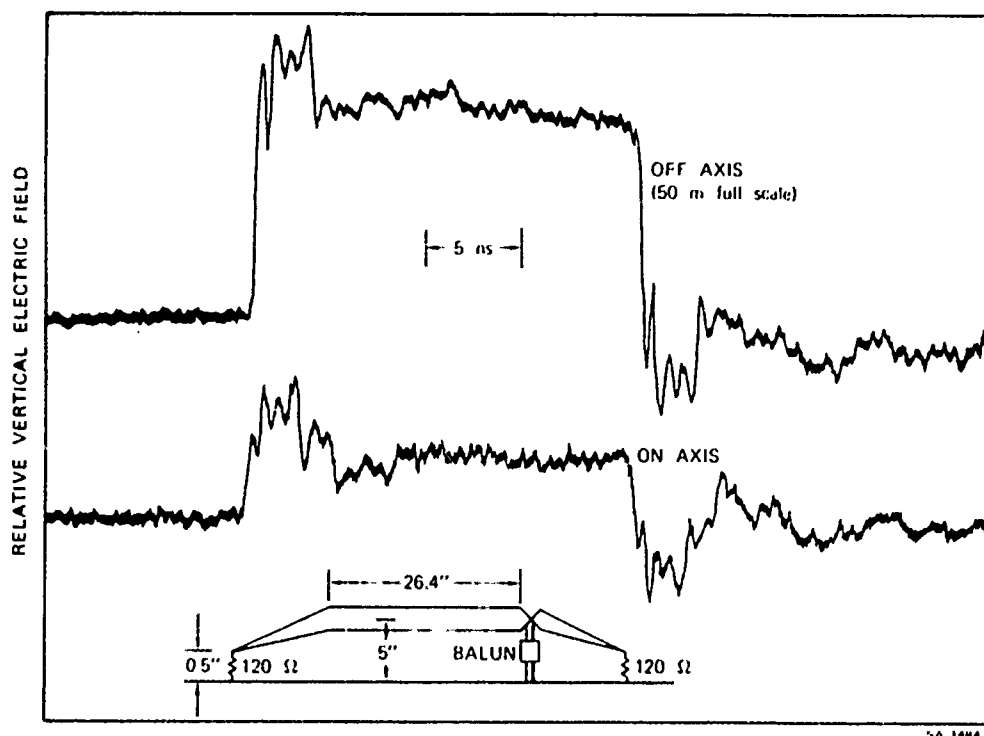


Figure 127 Vertical electric field with termination cone attached to bicone on one side.

The results for Configuration 3 (tilted bicone and section of cylinder) are shown in Figures 129 and 130. These data are for a distance from the axis of 25 meters full-scale and for positions on-axis and  $\pm 25$  meters off-axis. Although there is some vertical electric field at early times, the waveforms are quite distorted. The magnitude of both E- and H-fields is asymmetric, with much higher values on the side of the antenna that has a greater spacing to ground. Further, the risetime on the low side is smeared to much longer times than the input risetime.

Similar results were obtained at scale distances of 50 meter range and  $\pm 50$  meters off-axis, but because of the limited ground-plane size, only the first couple of nanoseconds of data were free of edge effects. Nevertheless, the distortion and asymmetry were evident in these data also.

The tilted-mode-model measurement results indicate the significant non-uniform nature of the electric and magnetic field data for these configurations for pulse durations as long as the required 800 nsec. Since this significant non-uniformity is not threat relatable, a tilted TEMPS configuration can be essentially ruled out. An alternative solution may be to locate the test object off the centerline of the TEMPS antenna. While it is recognized that it may be possible to achieve variable incident polarizations over a limited volume off the antenna centerline, the vertical electric field measurements obtained in this effort are insufficient to determine if the fields are threat relatable. In order to relate a total electric field vector (composed of horizontal and vertical components) from TEMPS to a threat situation with certain threat

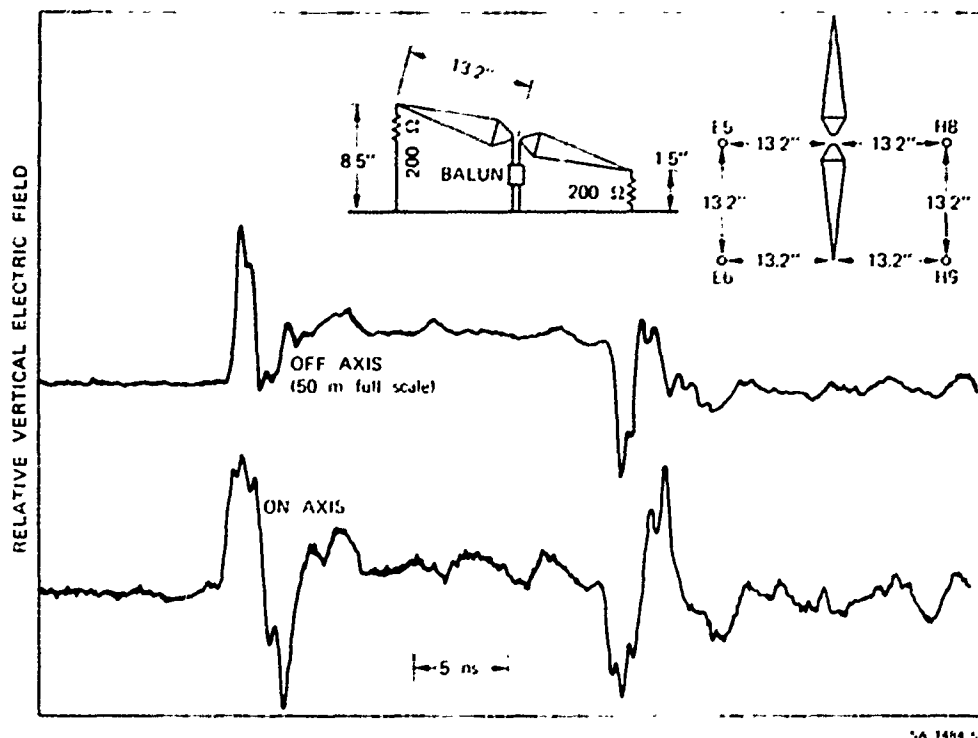


Figure 128 Vertical electric field from tilted-dipole made of termination cones.

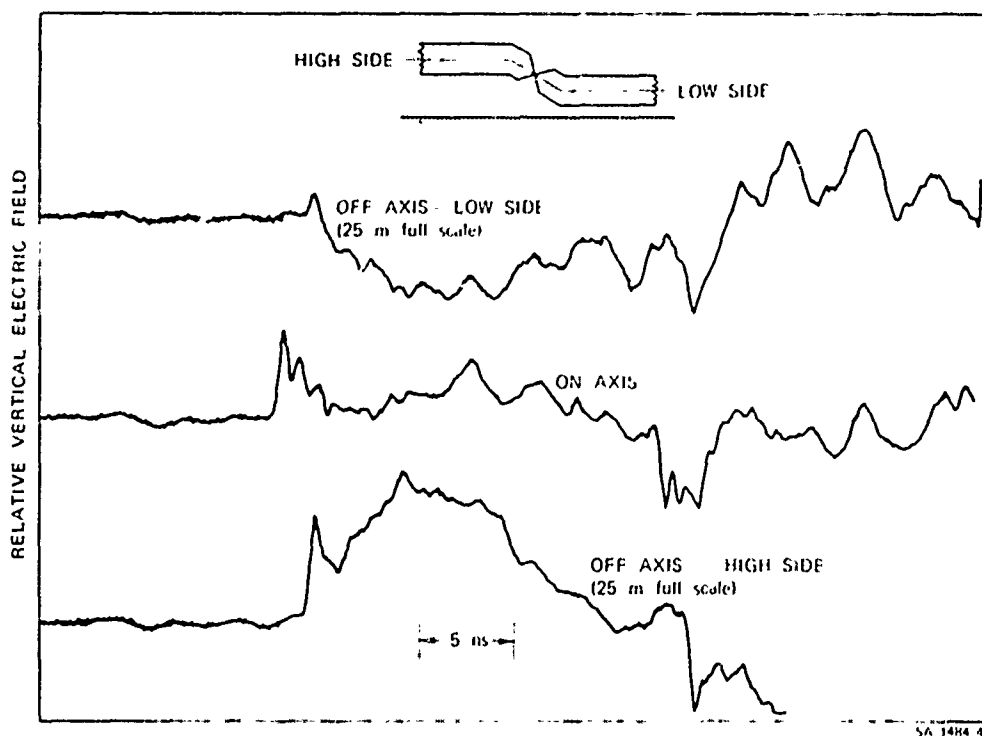


Figure 129 Vertical electric field from tilted bicone-cylinder configuration.

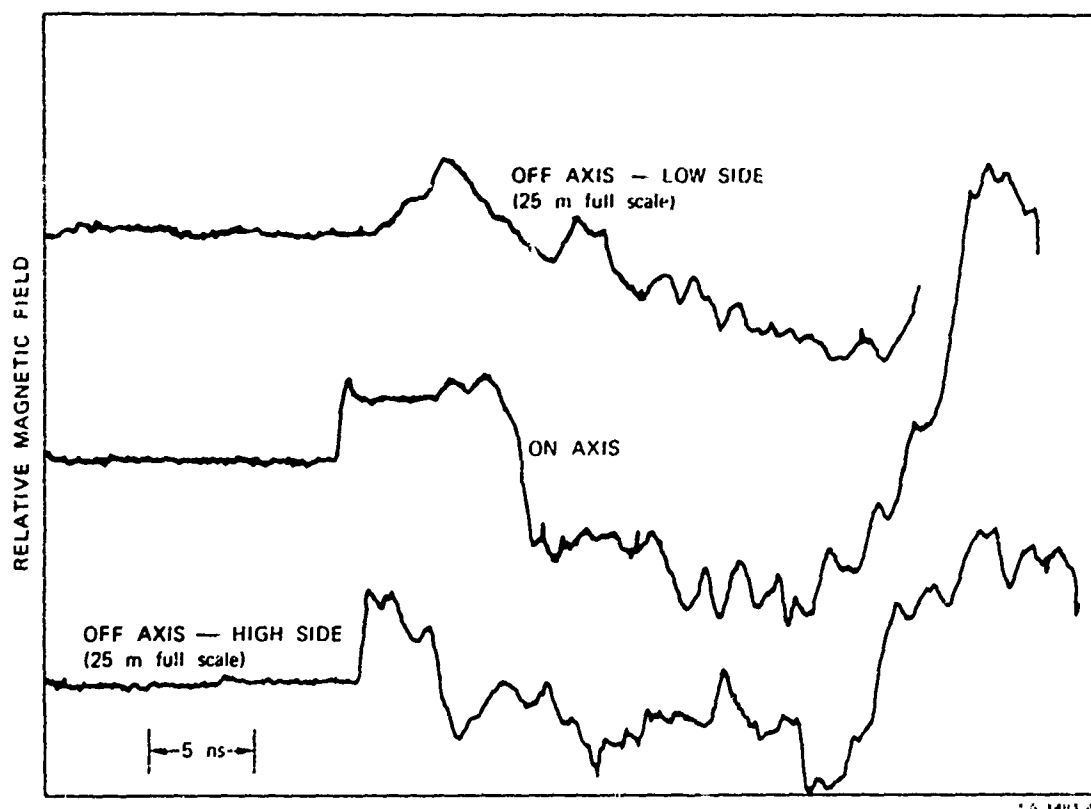


Figure 130 Radial magnetic field from tilted bicone-cylinder configuration.

parameters, the total magnetic vector must also be described in terms of its components (see Section A.3.5). The total electric and magnetic field vectors from TEMPS must then be compared with calculations of the threat environment in the presence of ground in order to determine if the TEMPS output is threat relatable in terms of an incident plane wave with a certain polarization angle and a certain angle of incidence.

## A.4 CONCLUSIONS

A full-scale late-time antenna consisting of cylindrical wire cages 30 feet in diameter and terminating cones that maintain an approximately constant impedance with respect to the ground will best meet the design specifications. This structure will radiate the desired pulse shape and duration with a pulser capacitance of 2.5 nF.

A 150:1 model of the TEMPS is shown in Figure 131. The model uses solid metal instead of wires. A wire cage consisting of about 40 wires, 1/8 inch in diameter, will produce fields that are only slightly below those of a solid metal cylinder. The wires may be held in place with metal hoops without significantly affecting the waveshape.

Wire sag can produce serious waveform distortion. To hold these effects to less than 10 percent at the lowest antenna height, wire sag should be less than 2 feet. At greater antenna heights, larger amounts of sag may be tolerated.

The terminating system should consist of a combination of a resistor and ground rods as given in Table XIII. The required combination for soil conductivities between  $10^{-2}$  and  $10^{-4}$  mho/m has been estimated.

To produce the effect of a rotation of polarization of 15 degrees it is recommended that the vertical electric field associated with the transmission-line mode be used although the threat reliability of this operating mode is questionable. To effect this mode will require mounting the TEMPS feed points off the center of the test site. For large test sites, three of the cylindrical cages may be mounted on the test-site side of the pulser and one cylindrical cage may be used on the other side.



## A.5 STEP RESPONSE OF A SINGLE-WIRE TRANSMISSION LINE ABOVE A LOSSY GROUND PLANE

A.5.1 Introduction. This section summarizes the theoretical results obtained for the risetime of a step-fuction input to a single-wire transmission line above an infinite ground plane with a finite resistivity. The results are based on work published by Sunde (Reference A-6). Two approximate expressions for the risetime of a step-voltage input are derived as a function of the line length, the line impedance, and the earth resistivity. One approximation is valid when the skin depth in the earth (of the highest frequency of interest) is much less than the height of the line above the earth. The other approximation is applicable when the skin depth is comparable to or larger than the height of the transmission line.

### A.5.2 Problem Solution

Step Response. Sunde has considered the problem of a single-wire transmission line above a ground plane that has a finite conductivity. Using Laplace transform techniques, he has derived an expression for the propagation constant,  $\Gamma$ , of the line and two asymptotic expressions for the step response:

$$\Gamma = p/vH(p) \quad (A-1)$$

where

$$H(p) = \left\{ 1 + \left( \log \frac{2h}{a} \right)^{-1} \left[ \log \left( \frac{1 + \beta p^{1/2}}{\beta p^{1/2}} \right) + \frac{1}{\beta_i p^{1/2}} \right] \right\}^{1/2} \quad (A-2)$$

$$\approx 1 + \frac{1}{2} \left( \log \frac{2h}{a} \right)^{-1} \left\{ \log \left( \frac{1 + \beta p^{1/2}}{\beta p^{1/2}} \right) + \frac{1}{\beta_i p^{1/2}} \right\} \quad (A-2)$$

$$\beta = h \left( \frac{\mu_o}{\rho} \right)^{1/2} ; \beta_i = a \left( \frac{\mu_o}{\rho_i} \right)^{1/2} \quad (A-3)$$



Figure 131 Photograph of 150:1 TEMPS model.

and

$p$  = Laplace transform variable

$h$  = distance from ground plane to center of the line

$a$  = radius of transmission line

$v$  = velocity of light in free space

$\mu_0$  = permeability

$\rho$  = resistivity of the earth

$\rho_i$  = resistivity of transmission line

The above result can be used to derive the time response for small times and large times. The approximation for small times is obtained by letting  $p \rightarrow \infty$  in Equation (A-2) above. Then the operational expression for the propagation characteristic becomes

$$\frac{I(x,p)}{I(0,p)} = \exp\left(-p \frac{x}{v}\right) \cdot \exp\left[-p^{1/2} x \left(2v\beta_1 \log \frac{2h}{a}\right)^{-1}\right] \quad (A-4)$$

where  $I(0,p)$  is the Laplace transform of the input signal. If the input signal is a unit step function, the solution of Equation (A-4) is

$$P(x,t) = \operatorname{erfc}\left[x \left(4\beta_1 v t_0^{1/2} \log \frac{2h}{a}\right)^{-1}\right] \quad (A-5)$$

where  $t_0 = t - x/v$  and  $\beta_1 = \beta\beta_i/(\beta + \beta_i)$ . Thus, the initial portion of the step response at a point  $x$  is given by the complementary error function. Also there is a time delay equal to the time required for the input to propagate to the point  $x$ .

Similarly, the asymptotic expression for large times is obtained by letting  $p \rightarrow 0$  in Equation (A-2). The corresponding operational expression for the propagation characteristic becomes approximately equal to the following:\*

$$\frac{I(x,p)}{I(0,p)} \approx \exp \left( -p \frac{x}{v} \right) \left[ 1 + \frac{px}{4v \log \frac{2h}{a}} \left( \log \beta_i^2 p - \frac{2}{\beta_i p^{1/2}} \right) \right] \quad (A-6)$$

The inverse transform of the above expression is

$$p(x,t) = 1 - x \frac{1 + \left( \frac{2}{v_1} \right) \left( \frac{t_0}{\pi} \right)^{1/2}}{4vt_0 \log \left( \frac{2h}{a} \right)} \quad (A-7)$$

There is some question in the mind of this author that Equation (A-7) is valid when  $a$  is comparable to  $h$ , but for lack of a better approximation we will proceed with Sunde's results.

One can use Equations (A-5) and A-7) to plot the step response for a given transmission line and ground plane. For example, Figure 132 shows the step response of a matched line 150 meters long, with a radius of 5 meters, at a height of 10 meters above the earth with resistivity equal to 100 ohm-meters. Curves for both the small time approximation and the large time approximation are shown. For the times shown, the small time approximation is the appropriate one. The conditions of applicability are discussed below. The time to reach 90 percent is about 1000 nsec.

---

\* Note that the term  $\beta_i p^{1/2}/2$  should be inverted in the expression on page 275 of Reference A-6.

Risetime. For many applications, the actual shape of the step response is not as important as the risetime. Expressions for the risetime can be obtained from Equations (A-5) and (A-7) by choosing an arbitrary value for the magnitude of  $P(x,t)$  as a measure. Typical choices are  $P(x,t) = 0.5$ ,  $0.9$ , or the time difference between  $P(x,t) = 0.1$  and  $0.9$ . We prefer to define the risetime as that value computed by setting  $P(x,t) = 0.9$  in either Equation (A-5) or (A-7).

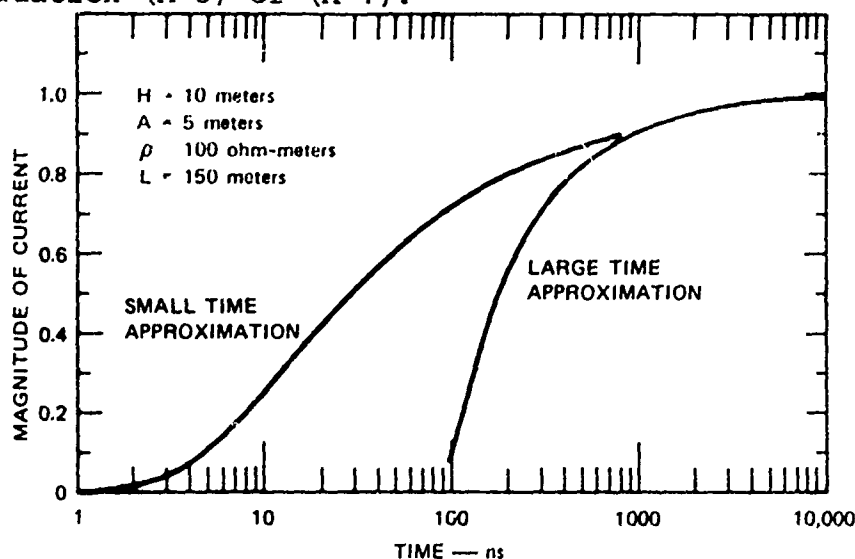


Figure 132 Large and small time approximations to waveform of a single-wire transmission line.

At first glance one may be tempted to assume that the rise-time would be determined only from Equation (A-7) since it applies for long times, and one would expect that  $P(x,t)$  would be close to  $0.9$ . However, for certain values of the transmission-line parameters and particularly for small values of resistivity for the earth, the small time approximation [Equation (A-5)] is valid even for values of  $P(x,t)$  in excess of  $0.9$ .

The small time approximation is obtained when  $p \rightarrow \infty$  in Equation (A-2). Then,

$$\log \left( \frac{1 + \beta p^{1/2}}{\beta p^{1/2}} \right) = \frac{1}{\beta p^{1/2}} - \frac{1}{2\beta^2 p} + \frac{1}{3\beta^3 p} \dots \quad (\text{A-8})$$

In this approximation it is assumed that the second- and higher-order terms are negligible. If the second term is negligible, then

$$\frac{1}{2\beta p^{1/2}} \ll 1 \quad (\text{A-9})$$

If we assume that the much-greater-than inequality is satisfied by a factor of 10, then Equation (A-9) may be rewritten as

$$\beta p^{1/2} > 5 \quad (\text{A-10})$$

Substituting for  $\beta$  we obtain

$$\delta < \frac{\sqrt{2h}}{5} \quad (\text{A-11})$$

where  $\delta = (2\rho/\mu_o p)^{1/2}$  is the skin depth for a given resistivity  $\rho$ . The inequality (A-11) is satisfied for all frequencies greater than some minimum frequency  $f_{\min}$ , which can be found by substituting  $p_{\min} = \omega_{\min} = 2\pi f_{\min}$  in Equation (A-11). Thus,

$$f_{\min} > \frac{25 \rho}{2\pi \mu_o h^2} \quad (\text{A-12})$$

The significance of this last result is that one can examine the spectrum of the input pulse and determine over what significant range of the time response the small time approximation

would be valid. If a major portion of the energy spectrum is above  $f_{\min}$ , then the small time fraction would be valid over most of the response time (possibly even above the 90 percent magnitude). On the other hand, if most of the energy is contained in the spectrum below  $f_{\min}$ , the small time approximation would be valid only over the very initial portions of the time response.

The minimum frequency decreases with decreasing earth resistivity and increasing line height. As an example, let

$$\begin{aligned}\rho &= 100 \text{ ohm-meter} \\ h &= 10 \text{ meter} \\ \mu_0 &= 4\pi \times 10^{-7} \text{ henry/meter}\end{aligned}$$

Then

$$f_{\min} \geq 3.2 \text{ MHz}$$

and a corresponding risetime,  $t_{\max}$ , would be

$$t_{\max} \leq \frac{1}{f_{\min}} = 314 \times 10^{-9} \text{ second}$$

It is evident from Figure 132 and the above result that the small time approximation is valid over a major fraction of the risetime of the step response for these parameters.

The large time approximation is obtained from  $p \rightarrow 0$  in Equation (A-2). Sunde (Reference A-6) uses the approximation

$$\log \left( \frac{1 + \beta p^{1/2}}{\beta p^{1/2}} \right) \approx - \log \beta p^{1/2} \quad (\text{A-13})$$

or

$$\beta p^{1/2} \ll 1 \quad (\text{A-14})$$

This inequality may be rewritten in terms of the skin depth as

$$\delta \gg \sqrt{2h} \quad (\text{A-15})$$

The large time approximation, therefore, is valid when the skin depth is much larger than the height of the line. We can find the corresponding maximum frequency,  $f_{\max}$ , and corresponding minimum time,  $t_{\min}$ , that satisfy the inequality (A-15), as follows:

$$f_{\max} \ll \frac{\rho}{2\pi\mu_0 h^2} \quad (\text{A-16})$$

$$t_{\min} \gg \frac{2\pi\mu_0 h^2}{\rho} \quad (\text{A-17})$$

If the major fraction of the energy in the input signal is below  $f_{\max}$ , then the large time approximation may be valid over a significant fraction of the time-response curve. Using our previous example, where  $\rho = 100$  ohm-meters and  $h = 10$  meters, we find  $f_{\max} \leq 0.12$  MHz and  $t_{\min} > 10^{-5}$  second. We see from



Figure 132 that the large time approximation for this example is valid only for  $P(x,t) \approx 0.99$ . On the other hand, as  $\rho$  increases,  $t_{\min}$  decreases. Thus, for  $\rho > 1000$  ohm-meters, the large time approximation may be used to find the risetime of the step response at the 0.9 point.

The dependence of the risetime on the line impedance, line length, and earth resistivity for the small time approximation and the large time approximation are determined by setting  $P(x,t) = 0.9$  in Equations (A-5) and (A-7).

If  $y$  is equal to the argument of the complementary error function with  $P(x,t) = 0.9$ , it is easily shown that the risetime,  $t_r$ , for the small time approximation is given by the following expression:

$$t_r = \frac{225x^2\rho}{y^2\mu_0 v^2 h^2 Z_0^2} \quad (A-18)$$

where  $\beta_1 \approx \beta$  has been used, and  $Z_0 = 60 \log 2h/a$  is the transmission-line characteristic impedance. This expression shows that the risetime is proportional to the earth's resistivity and to the square of the line length. The risetime is inversely proportional to both the square of the height of the line above the earth and the square of the line impedance.

For the large time approximation the risetime (90 percent point) is given by the following linear relationship:

$$t_r = \frac{150x}{vZ_0} \quad (A-19)$$

where the term

$$\frac{2}{\beta_i} \left( \frac{t_o}{\pi} \right)^{1/2}$$

has been dropped because it is negligible compared to unity for copper wires. In this approximation the risetime is a linear function of line length and inversely proportional to the line impedance. This expression is valid only for earth resistivities greater than 1000 ohm-meters.

The accuracy of Equation (A-19) is questionable because the approximation used to derive this result may not be valid for large values of wire diameter. In Equation (A-2),  $H(p)$  was approximated by the first two terms of a series expansion for the radical expression. This series approximation is valid if the second term under the radical sign is small. However for transmission lines with large diameters the second term may be comparable to unity for low frequencies. We have used Sunde's result with this reservation because the complexity of the mathematics precludes a more accurate approximation without considerable effort.

A.5.3 Conclusions. Based on Sunde's work we have derived two approximations for the risetime of a step-function pulse on a single-wire transmission line above a ground plane with finite resistivity. The small time approximation is valid when the skin depth of the highest frequencies of interest is less than the height of the line above the earth. The large time approximation is to be used when the skin depth is greater than the height of the transmission line. This large time approximation appears to be applicable for resistivities in excess of 1000 ohm-meters.

## REFERENCES TO APPENDIX A

- A-1. S. Ramo, J. R. Whinnery, and T. Van Duzer, Fields and Waves in Communication Electronics, John Wiley & Sons, New York, N.Y. (1965).
- A-2. D. E. Merewether, "Synthesis of an Electromagnetic Pulse Generator," IEEE Trans., PGAP-17, pp. 236-237, March 1969.
- A-3. Schelkunoff and Friis, Antenna Theory and Practice, John Wiley & Sons, Inc., New York, N.Y. (1952).
- A-4. E. F. Vance and S. Dairiki, Analysis of Coupling to the Command Power System, Technical Report 5 SRI Project 7995, Contract F29601-69-C-0127, Stanford Research Institute, Menlo Park, California (in press).
- A-5. A. L. Whitson and E. F. Vance, Electromagnetic Field Distortions and Currents In and Near Buried Cable Bunkers, AFWL-TR-65-39, Stanford Research Institute, Menlo Park, California, September 1965.
- A-6. E. Sunde, Earth Conduction Effects in Transmission Systems, pp. 271-275, D. Van Nostrand, Co., New York, N.Y. (1949).

APPENDIX B  
CAPACITOR DEVELOPMENT  
AND TESTING

## B.1 ENERGY STORAGE CAPACITOR SPECIFICATIONS

B.1.1 General. This specification describes the electrical and physical requirements of energy storage and discharge capacitors for operation in a 50-kJ Marx generator situated in a Freon 12 or SF<sub>6</sub> gas insulation environment.

Low capacitor weight and inductance were desirable, but the delivery schedule for the completed system precluded advanced capacitor design and development.

As a result, capacitors were sought of conventional design that can be readily packaged to satisfy the electrical and physical requirements of the system.

Orders were placed with more than one capacitor manufacturer for the prototype units.

### B.1.2 Electrical Requirements.

- a. Voltage and capacitance: The maximum capacitor operating voltage is 100 kV. Capacitance is 0.18  $\mu$ F  $\pm$  10 percent.
- b. Time to charge:  $\geq$  20 seconds but  $\leq$  60 seconds.
- c. Time at full charge:  $\leq$  5 seconds per shot.
- d. Repetition rate:  $\leq$  1 shot per 2 minutes.
- e. Inductance: Consistent with a 2-MHz self-resonant frequency.
- f. Equivalent series resistance under pulse discharge conditions: 150 m $\Omega$ .
- g. Percent reversal: Zero reversal under normal operating conditions. Under fault conditions, which is estimated to occur once in every 200 shots, reversal will be approximately 40 percent at 1 MHz.

h. Current: Normal peak operating current is approximately 50 kA. Under fault conditions peak current will be less than or equal to 200 kA.

i. Life: For the specified conditions a mean life of 10,000 shots is sought.

B.1.3 Physical Requirements. A compact low-inductance Marx generator is necessary to satisfy system requirements. The physical shape of the required capacitors is that of a flat rectangular box, to be compatible for stacking in one column.

Rail type connection to the capacitors is required.

Capacitor energy density of at least 20 J/lb ( $\approx 1.25 \text{ J/in.}^3$ ) is required. Capacitor thickness in the direction of voltage is important and the goal is 2-1/2 inches or less.

The remaining capacitor dimensions, i.e., length and width, are flexible with bounds (stated below) providing that capacitor energy density is equal to or greater than 20 J/lb. The preferred dimensions are approximately 17 inches x 17 inches x 2-1/2 inches.

However, neither the length nor width dimensions of the capacitor may exceed 20 inches.

Capacitor cases are to be plastic and are to be leak proof under the environmental conditions described below. If your design consists of the combination of smaller capacitor units in series and/or parallel, no additional case is required, although a light framework to hold the smaller units together must be provided.

#### B.1.4 Environmental Conditions and Specifications.

a. Operating environment: Freon 12 or SF<sub>6</sub> gas at a pressure of 12 to 30 psia. The gas may be mixed with air; however, the breakdown yield strength of the gas will not be less than 75 percent of that of pure Freon 12. DC insulation of the terminals must be adequate for safe operation in such as a gas mixture at the lowest pressure. Operation at up to 15 psi above ambient is desirable though not essential; limitations to a lower pressure should be stated, however.

b. Storage temperature: -20°F to 120°F.

c. Operating temperature: 0°F to 100°F with no de-rating.

#### B.2 PROTOTYPE CAPACITOR PULSE DISCHARGE TEST PLAN

B.2.1 Purpose. The purpose of prototype capacitor testing was to evaluate capacitor electrical performance to provide a basis for selection of the TEMPS system capacitors.

Two prototype capacitor manufacturers were selected, Maxwell Laboratories and Condenser Products, Inc. Capacitor specifications including dimensions are given in the next section.

B.2.2 Approach. Pulse discharge testing was conducted under electrical conditions that simulate, within reasonable limits, the operating conditions "seen" by the capacitors in actual use.

In service, the maximum peak current supplied by each Marx is approximately 50 kA under normal conditions and may be as much as three times this value under fault conditions. Thus, for the Condenser Products, Inc. capacitor, normal peak current per capacitor is approximately 50 kA and is approximately 25 kA for the 0.09 μF Maxwell units.

The electrical circuit for pulse discharge testing is shown in Figure 133, where the load is essentially a pure resistance. The TEMPS circuit uses a peaking capacitor, and it is during pulse charge of the peaker that the Marx supplies the peak current. Thus, the test circuit only crudely approximated the actual circuit, but was felt to be adequate and was a less complex circuit to construct for test purposes.

B.2.3 Test Description. For pulse discharge testing, all five prototype capacitors from each manufacturer were charged in parallel to the maximum voltage (100 kV) from a common high-voltage power supply. Each capacitor was, however, resistively isolated from the remainder (Figure 133).

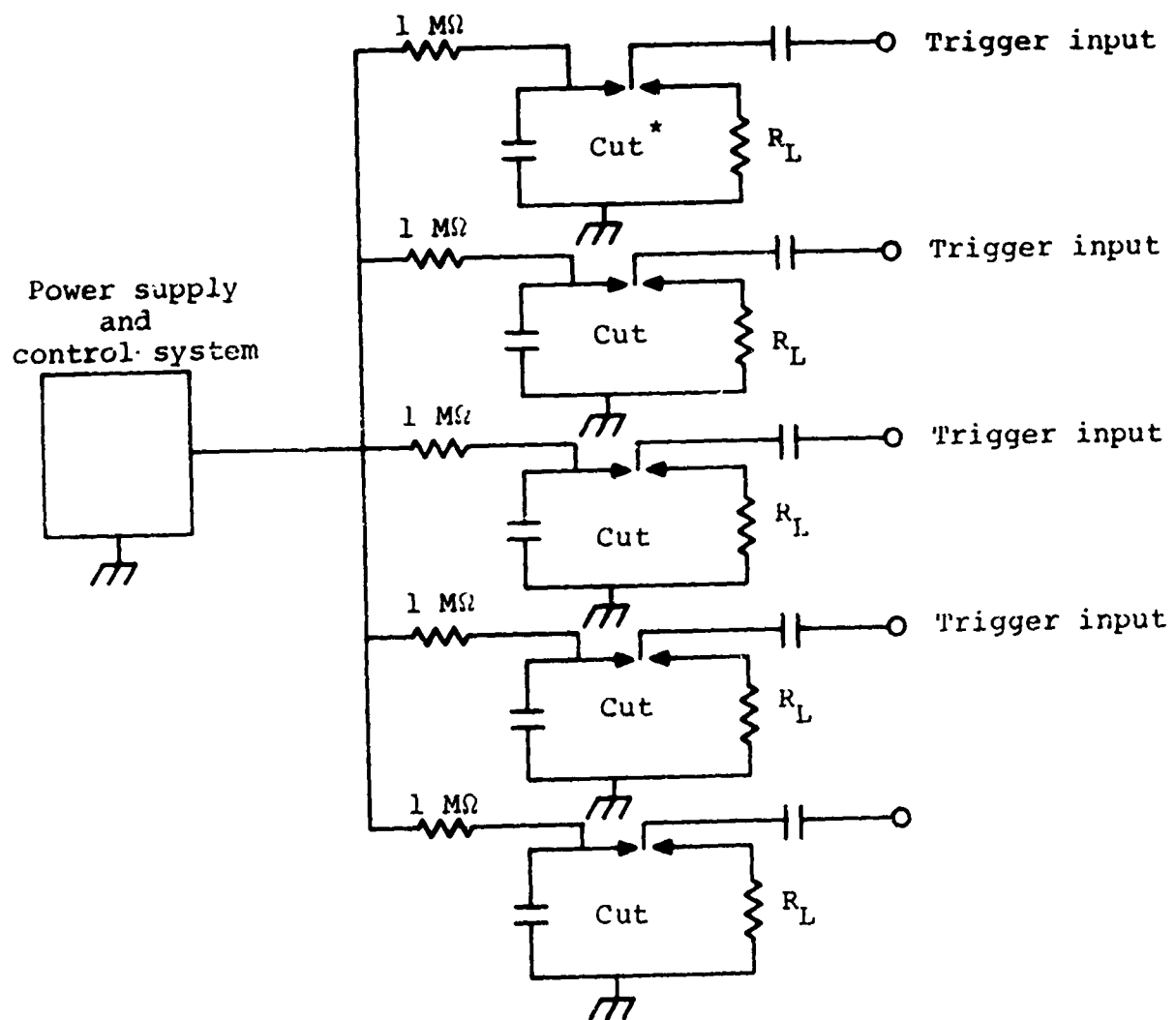
After reaching full charge voltage, the power supply was automatically disconnected from the high voltage circuit and the capacitors discharged into their respective individual loads.

Pressurized gas rail spark gaps were used to switch the capacitors into their loads. These gaps were electrically triggered for simplicity. Gap electrodes are 5/8 inch in diameter separated by a 1.25-cm gap spacing.

A repetition rate of 1 pulse per minute maximum was proposed. The power supply is capable of supplying 5.5 mA at 100 kV. For constant current charging, this is adequate for either the Condenser Products or Maxwell units.

Resistive loads for the Condenser Products and Maxwell units must be less than or equal to 2 and 4 ohms respectively, to meet the peak current requirements. The actual values were somewhat





\* Capacitor under test

Figure 133 Prototype capacitor test circuit.

less than those quoted above since stray series inductance tends to limit the current. Assuming critically damped circuits we are able to place an upper bound on stray circuit inductance. For the Condenser Products unit, the critical circuit resistance  $R_c$  is about 1.5 ohms with an associated inductance of approximately 100 nH. For the Maxwell units the critical resistance and associated inductance are 3 ohms and 200 nH respectively. Load resistor design is based upon the above values of  $R_c$  and the inductance must not exceed the quoted values. If the inductances were less than the quoted value, then the resistance could be increased somewhat.

An appropriate choice of load medium is a copper sulfate liquid resistor which may be easily changed to satisfy the electrical requirements provided that a minimum basic volume to reach the lowest resistance anticipated is incorporated into the original load design.

The anticipated load configuration and connections for each of the five test stations is shown in Figure 134. The physical geometry is roughly that of a stripline.

Inside dimensions of the load are approximately 3 inches long x 18 inches wide x 4 inches deep. The box is filled to within 1/2 inch of the top; hence the volume of liquid is approximately 204 in.<sup>3</sup> ( $\sim 3350$  cm<sup>2</sup>). Maximum energy deposited in the resistor per shot is 900 joules ( $V_{dc} = 100$  kV,  $C = 0.18$   $\mu$ F) which corresponds to 215 calories. Taking the specific heat of water as 1 cal/gm/C<sup>0</sup>, the temperature rise per shot is approximately 0.065 C<sup>0</sup>. For a pulse repetition rate of 1 shot per minute, the equilibrium temperature of the load should be only a few degrees above ambient.

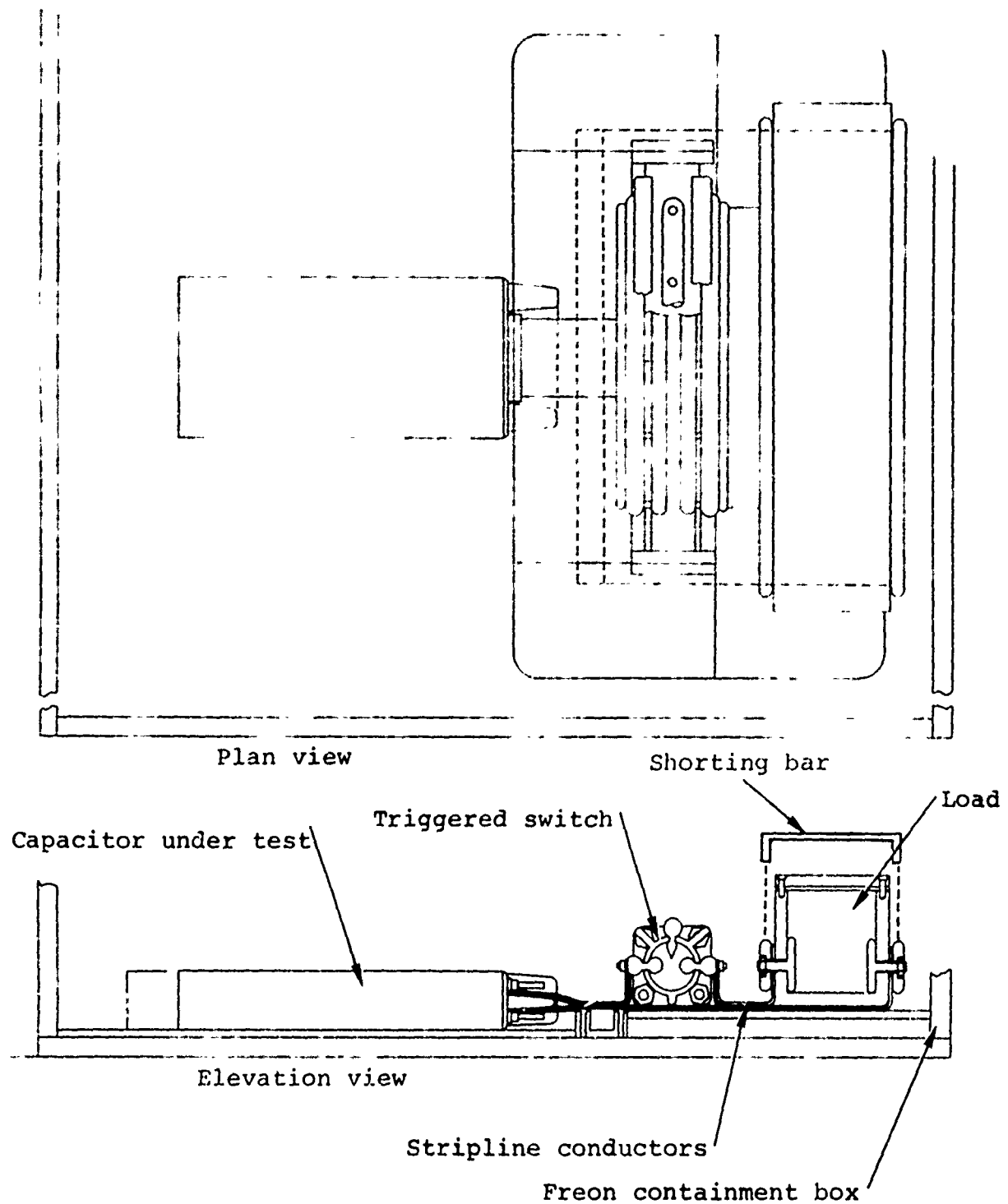


Figure 134 TEMPS storage capacitor test bed.

Load electrodes are copper for compatibility with the cupric sulfate solution and also aid in the cooling of the load.

For a saturated cupric sulfate solution at room temperature, load resistance is less than 1 ohm, significantly less than the minimum required resistance.

Circuit inductance estimates based upon the physical geometry and anticipated capacitor inductances are tabulated in Table XIV. In both cases the estimated inductance is less than the maximum allowable values.

For fault current testing a load shorting bar is installed as shown in Figure 134. Length of the shorting bar legs was, in the course of testing, adjusted to yield the correct inductance. With minimum dimensions, the shorting bar increases circuit inductance by about 15 nH. At 100 kV dc and assuming no stray series resistance, peak current is 80 kA and 130 kA for the Maxwell and Condenser Products capacitors respectively. Maximum values were less than these because of stray series resistance. However, fault current testing was tailored for each capacitor manufacturer to reflect actual expected conditions.

**B.2.4 Test Procedure.** Five prototype capacitors from each of the two manufacturers were tested at one time. DC charge voltage was 100 kV, the maximum voltage, and all five units were charged in parallel from a single power supply. Pulse discharge repetition rate was approximately 1 pulse per minute, a reduction from the proposed 2 shot/min (Reference 1). But a pulse repetition rate of 1 pulse/minute is more in keeping with the final system dc charge time and hence its use probably provides a better basis for capacitor evaluation.

TABLE XIV  
CIRCUIT INDUCTANCE

	Maxwell (nH)	Condenser Products (nH)
Capacitor	56	28
Connection to spark gap	~ 10	~ 10
Spark gap electrodes	11	11
Spark gap arc	24	24
Connection to load	negligible	negligible
Load	20	20
TOTAL	121	93

After the prototype capacitors have received 2500 shots, a decision point was reached which depended upon the number and modes of failures occurring up to that time. If no failures had been experienced, 2500 additional shots would have been taken.

Fault current testing, 1 shot out of every 101 normal discharge shots, was originally proposed (Reference 1). It appeared appropriate at this juncture to delay fault current testing until capacitor evaluation under normal conditions were complete in order to separate and identify potential energy storage capacitor problems and limitations.

Current monitors were incorporated into each of the five pulse discharge circuits which took the form of a small series inductance--small with respect to the stray series inductance. These monitors yield an i-dot signal which can be passively integrated to yield circuit current as a function of time.

Discharge current was recorded periodically to ensure proper operation of each of the five capacitor test circuits.

### B.3 PROTOTYPE CAPACITOR PULSE DISCHARGE TEST RESULTS, CONDENSER PRODUCTS COMPANY UNITS

All five Condenser Products capacitors were installed in the test stand (the stand is shown in Figure 135) and the load resistors adjusted to 1.7 ohms, a value which yields a capacitor peak current of about 50 kA. This value is in keeping with the anticipated actual current that the energy storage capacitors must supply in the TEMPS system.

Circuit inductance for each test station was approximately 85 nH, determined from analysis of the discharge waveforms. An approximate breakdown of circuit inductance is shown in Table XV.

A typical example of the normal discharge waveform, both calculated and measured, is shown in Figure 136. The measured waveform was made with the use of an i dot monitor in series with the discharge circuit, which was passively integrated at the monitor recording oscilloscope (Tektronix Model 454). Integrator time constant was 10  $\mu$ sec, yielding about a 5 percent droop in the measured current over the pulse duration.

All five capacitors were charged to full voltage (100 kV) and discharged at a rate of 1 shot per minute for 24 hours a day, i.e., about 1440 shots per day. This discharge rate was maintained for a minimum of 5000 shots on each unit. All five capacitors successfully survived this part of the testing and the actual number of shots accrued on each unit is shown in Table XVI.\*

---

\* All capacitors did not receive an equal number of shots since some initial difficulties were experienced in the operation of the test stand and not all units were operated during this debugging period.

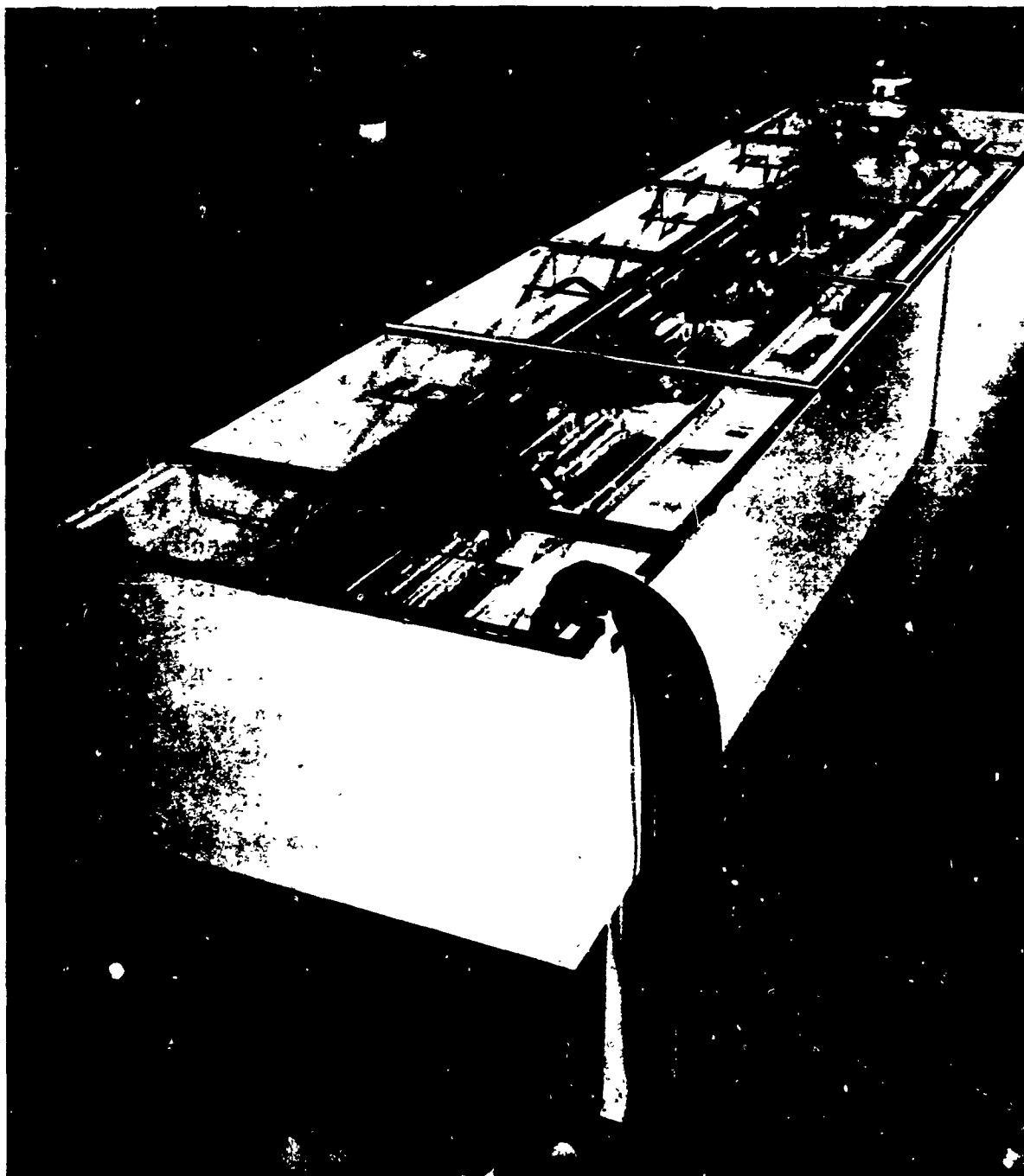


Figure 135 Five-station capacitor test stand.

TABLE XV  
CIRCUIT INDUCTANCE, CONDENSER PRODUCTS CAPACITORS

	<u>Inductance (nH)</u>
Capacitor	18
Connection to spark gap	7
Spark gap electrodes	11
Spark gap arc	24
Connection to load	5
Load	<u>20</u>
TOTAL	85

TABLE XVI  
NORMAL DISCHARGE SHOT SUMMARY

<u>Station Number</u>	<u>Serial Number</u>	<u>Shots</u>
1	CP 11	5207
2	CP 00	5047
3	CP 44	5687
4	CP 33	5167
5	CP 22	5206



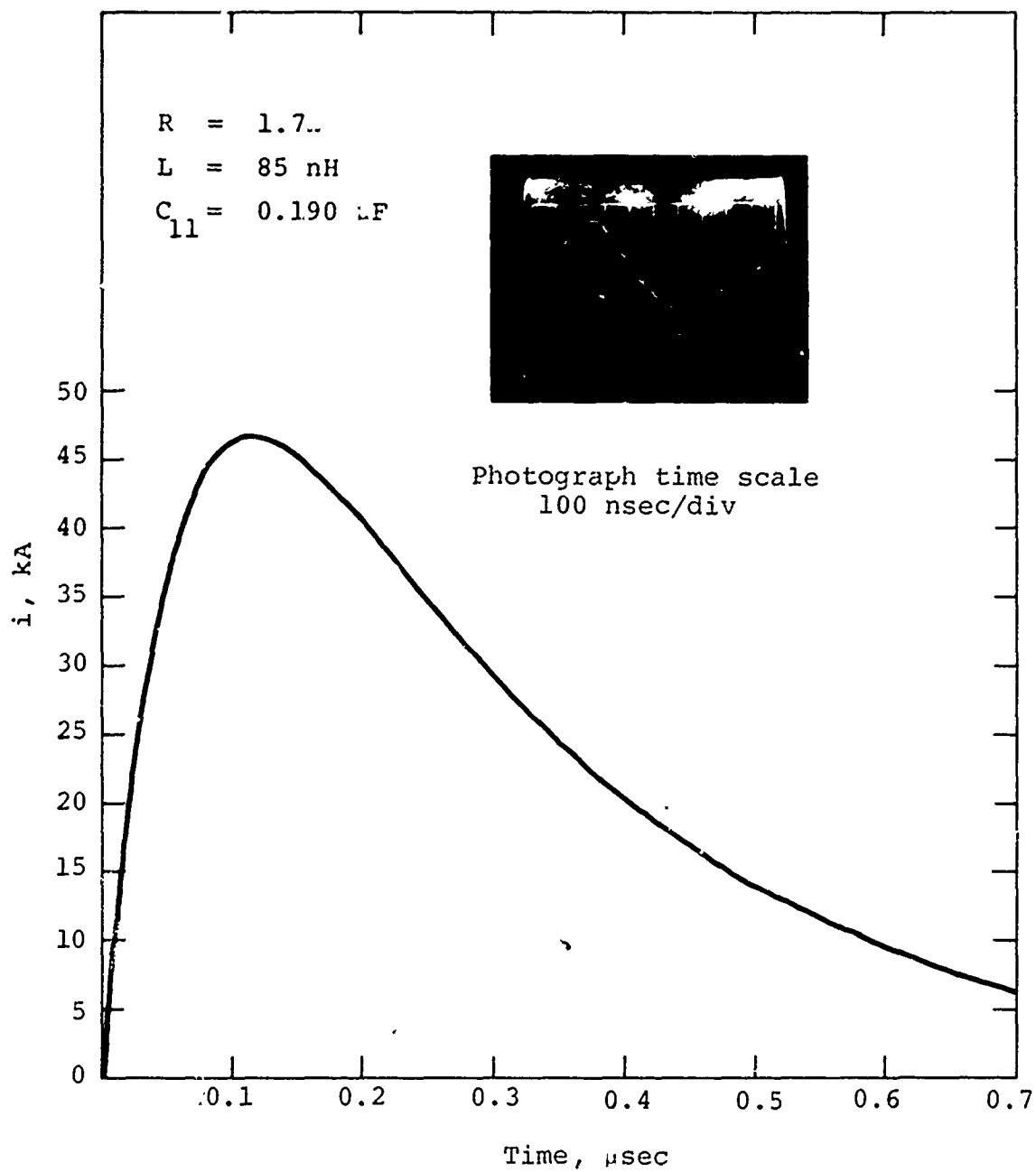


Figure 136 Pulse discharge waveform (calculated and actual),  
Condenser Products prototype capacitor.

All units were removed from the test stand upon completion of this part of the testing and thoroughly examined. Station numbers 1, 3, 4, and 5 showed evidence of impregnant leakage from the units. In no case was the leakage from the region around the studs or epoxy joint at the individual tube ends, which might be expected, but was associated for the most part with small hairline cracks in the cases of isolated tubes within each unit. In two instances, oil leakage from the impregnation holes in two tubes was noted.

It was preliminarily concluded that the small cracks were due to defects in the phenolic tubing which showed up as a result of pressure build-up in the tubes. Hydrogen gas is normally evolved within energy storage discharge capacitors as a result of the corona-induced decomposition of the impregnant at the capacitor foil edges, and internal pressure build-up results. However, this process would normally occur very slowly for TEMPS, since the capacitors would not be cycled continuously but only for perhaps as much as 10 hours a day. In the judgment of the manufacturer, this mitigates the pressure build-up problem because there is sufficient off-time for some fraction of the gas to combine chemically with the impregnant. A related problem is also apparently introduced by this gassing process. In a continuous cycling operational mode, sufficient gas may build up to the point at which impregnant is excluded from the margin of a capacitor section winding, leading to flashover of the margin and subsequent section short circuit. These conclusions appear to be generally held among capacitor manufacturers, but the details of the process do not seem to be well understood.

Autopsy of three capacitor tubes having cracked cases revealed that in two of the three tubes one section of the ten series sections was indeed shorted.

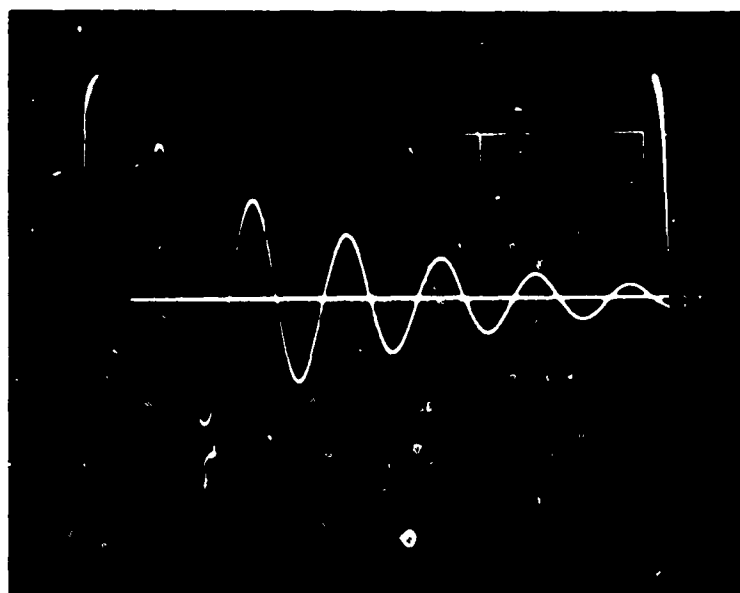
Based upon this information, it was then concluded that capacitor tube case cracks were due largely to section failure, accelerated gas evolution, pressure build-up, and subsequent mechanical damage to the phenolic tubes in the immediate vicinity of the shorted section. However, in other instances, defects in the phenolic cases or inadequate sealing of the impregnant fill holes appeared to have been the cause for impregnant leakage.

It is probably fair to conclude that the continuous cycling test mode was, in effect, an overtest since no off-time was included in the testing to allow evolved gas to chemically combine with the mineral oil impregnant.

B.3.1 Fault Current Test Results. After examination of the capacitors was complete, unit no. CP 11 was re-installed in the test stand, the load short-circuited, and fault current testing begun.

A typical discharge current waveform is shown in Figure 137. Analysis of the waveform yielded the equivalent circuit shown in Figure 138. Stray series circuit inductance was approximately 1.00 nH, an increase of 15 nH from normal discharge testing; the increase was due to the short circuit connection across the top of the load resistor. Stray series circuit resistance was approximately 90 m $\Omega$ , about 40 m $\Omega$  associated with the capacitor; the remainder was due to connections and the spark gap arc.

An operating level of 67 kV was chosen for this testing, since peak current for this voltage is about 85 kA, comparable to that expected from TEMPS in the event of a fault. The waveform for this testing is much less damped than that anticipated in TEMPS; capacitor reversal in this testing was about 83 percent.



Time scale 0.5  $\mu$ sec/div.

Figure 137 Prototype capacitor high reversal waveform.

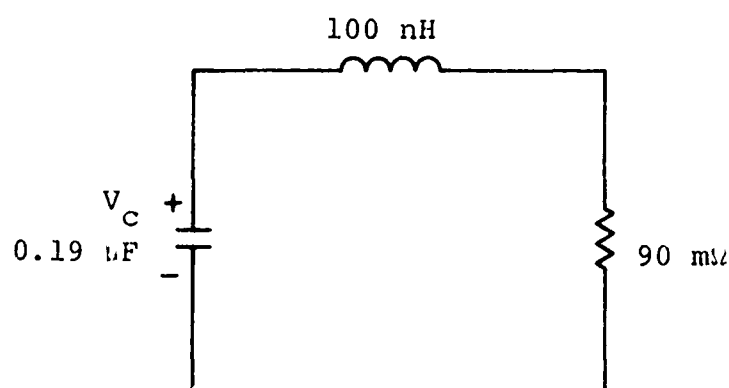


Figure 138 High reversal test equivalent circuit.

Forty-three shots were taken on capacitor no. CP 11 before it was noticed that a tube had burst (Figure 139). The capacitor still functioned normally electrically, but was removed from the stand. The tube had burst somewhere between shot no. 32 and no. 42, but because it was electrically sound, the exact number is not known. This failure was due to a shorted section, which accelerated gas evolution and resulted in pressure build-up, which subsequently ruptured the case.

Capacitor no. CP 44 was then installed in the stand for testing under the above conditions. After 1628 shots, a blown tube similar to that of the previous unit was discovered. The capacitor was electrically all right; hence, the exact shot in which the case blew is not known. Autopsy of the blown tube revealed a shorted section at the rupture location.

In the capacitor specifications, it was estimated that, in use, a fault discharge would occur no more often than 1 shot out of each 200 normal shots. Hence, for 5000 normal discharge shots, 25 fault discharges could, in the worst case, be expected. Both units tested survived well beyond this number of shots, and therefore are judged satisfactory for the TEMPS system.

While the purpose of fault current testing was to test the adequacy of connections within the capacitors to withstand high peak currents, operation at 67 kV was not a true test of the capacitors ability to sustain the total peak-to-peak voltage swing consistent with operation at 100 kV.

Therefore, the pulse discharge circuit was modified with the installation of series limiting resistance of the value proposed for TEMPS, i.e., about 270 m $\Omega$ . Stray resistance

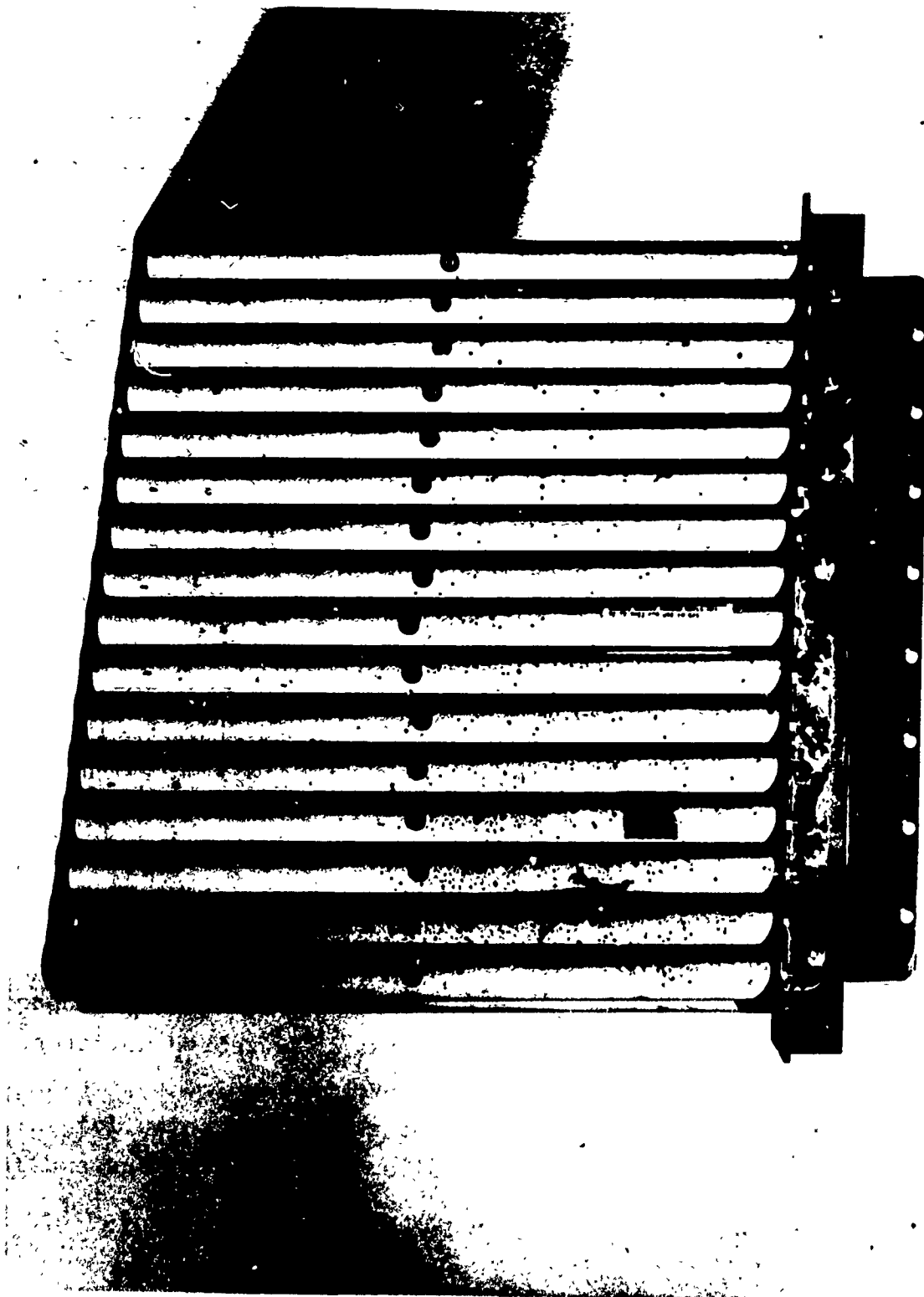


Figure 139 Burst tube, station No. 1.

increases this value about 0.36 ohm for the total circuit. Computed and measured discharge current waveforms are shown in Figure 140 and are nearly identical to those anticipated for the TEMPS system for the condition existing when the Marx is erected into a short circuit.

Capacitor no. CP 33 was tested with this circuit for the following conditions: 327 shots at 48 kV charge, 325 shots at 70 kV, 75 shots at 100 kV, and 30 shots at 87 kV.

The unit successfully survived this testing without electrical failure of the capacitor as a whole nor was there any evidence of section failure within the individual tubes.

B.3.2 Summary, Conclusions, and Recommendations. In summary, all five Condenser Products Company prototype units successfully survived a minimum of 5000 normal pulse discharge cycles and three units at least 40 fault discharge cycles; i.e., all units were electrically operational with no detectable change of performance at the conclusion of the testing.

Upon examination at the conclusion of normal pulse discharge testing, it was noted that four out of the five units were leaking a small amount of mineral oil impregnant. In the majority of the cases, this was later determined to be caused by a short circuit failure of one section of one tube of the capacitors. In the remainder of the cases, leakage appeared to be caused by defects in the phenolic tubing or inadequate sealing of the impregnation holes in the tubes. In no case were more than two tubes of any one capacitor affected in these ways.



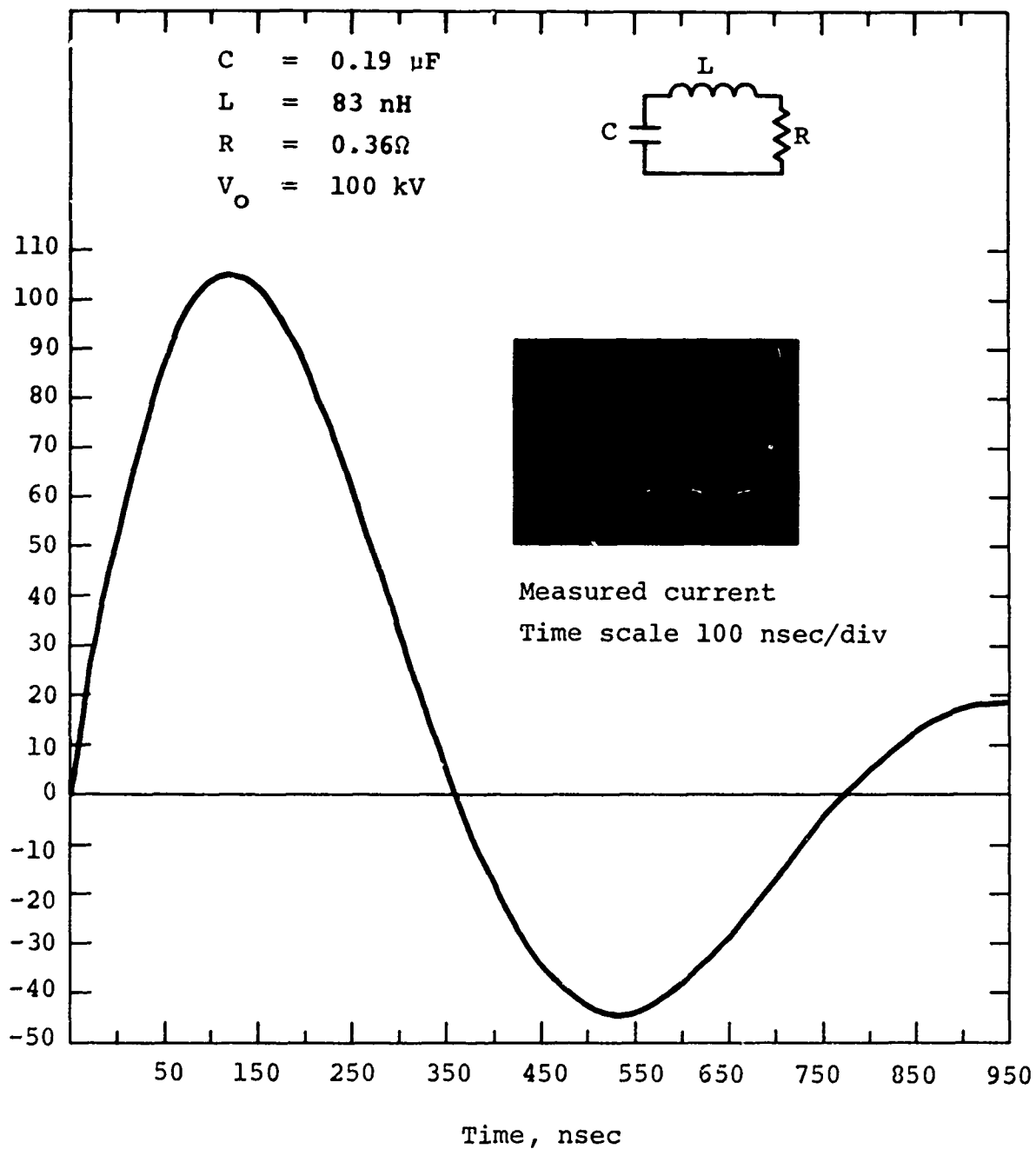


Figure 140 Computed and measured pulse discharge current, series limiting resistance installed.

While these problems are of some cause for concern, there is evidence that the test repetition rate and continuous cycling accelerated section short-circuit failure, and hence constituted an overtest.

Defects in the phenolic tubing and sealing problems can be overcome by improving material quality control and inspection. These concerns have been communicated to the manufacturer and he has taken steps to improve quality control.

In conclusion, based upon pulse discharge testing, the Condenser Products Company capacitors appear to adequately satisfy energy storage pulse discharge capacitor requirements for the TEMPS systems. However, Physics International Company recommends that additional capacitors be procured and tested to provide a more complete statistical basis for determining capacitor life. For this testing, PI recommends that the test repetition rate be no greater than 1 shot per 3 minutes and that the units be tested for one 8-hour period per day.

#### B.4 PROTOTYPE CAPACITOR PULSE DISCHARGE TEST RESULTS, MAXWELL LABORATORIES, INC. UNITS

As described in Reference 12, Section 2.1.2, dc-insulation problems associated with the Maxwell Laboratories prototype capacitor header were experienced during initial pulse-discharge tests, and a separate evaluation of this problem was initiated. The following paragraphs report the results of dc-insulation tests and pulse-discharge testing.

B.4.1 DC-Insulation Tests. A typical Maxwell Laboratories prototype TEMPS energy storage capacitor is shown in Figure 141. The header or bushing installed on these units is essentially identical to that employed on the Maxwell Laboratories 50-kV "Series S" units listed in their catalogue. The header is injection molded, and the material appears to be Celcon or Delrin. Salient header dimensions are shown in Figure 142. As a result of dc-breakdown problems at voltages approaching 100 kV in Freon 12 and SF<sub>6</sub> gas environments, bare headers were obtained from Maxwell Laboratories to facilitate dc-insulation tests.

DC-insulation tests began with a test of the bare header with no conductors attached to the rail terminals (Figure 142). In all tests a 500-pF high-voltage capacitor was connected across the terminals to drive incipient streamers into arc. These and the following tests were performed in both Freon 12 and SF<sub>6</sub> gas environments; gas pressure was 1 atm abs.

B.4.2 Bare-Header Test Results. Using SF<sub>6</sub> gas, header flashover occurred at 153 kV. With Freon 12, flashover occurred at 120 kV. In both cases the arc path was on the barrier surface from one output rail to the other.

B.4.3 Close Spaced Output Connector. To make effective use of the low inductance associated with this type of capacitor, a stripline conductor geometry is the most appropriate means of connecting the capacitor and load. This type of configuration was tested. For this test, two 3-inch-wide brass plates equipped with 1/8-inch-diameter edge radii were installed as indicated in Figure 143. Mylar insulation (4 sheets of 5 mil Mylar) was wrapped around each conductor extending beyond the ends of the conductors, although tests were performed without any Mylar at all. Test results are summarized in Table XVII. The breakdown arc paths were over the capacitor barrier from one output-rail connector to the other, essentially identical to the first test.



Figure 141 Maxwell prototype, TEMPS energy storage capacitor.

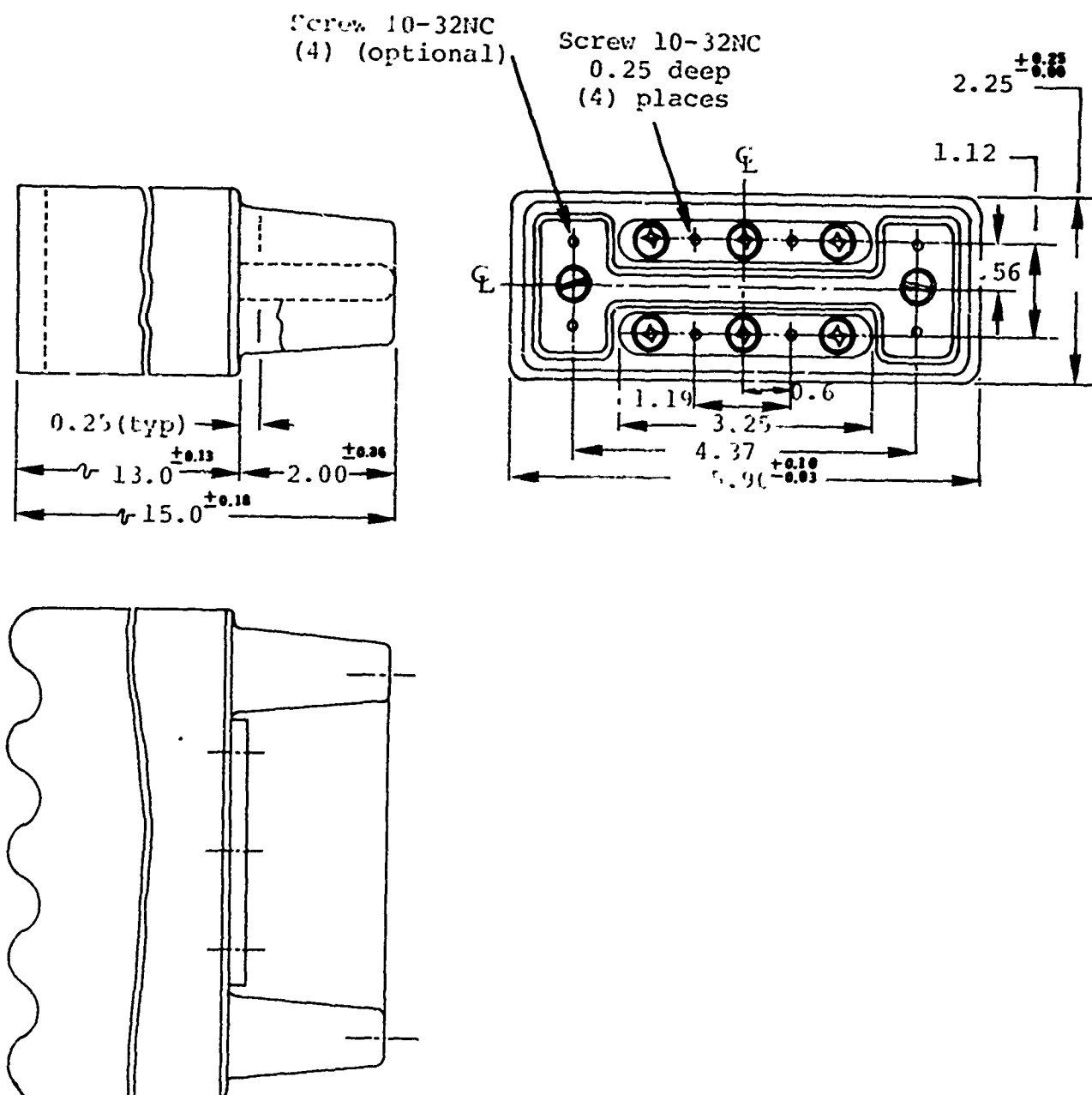


Figure 142 Energy-storage capacitor.

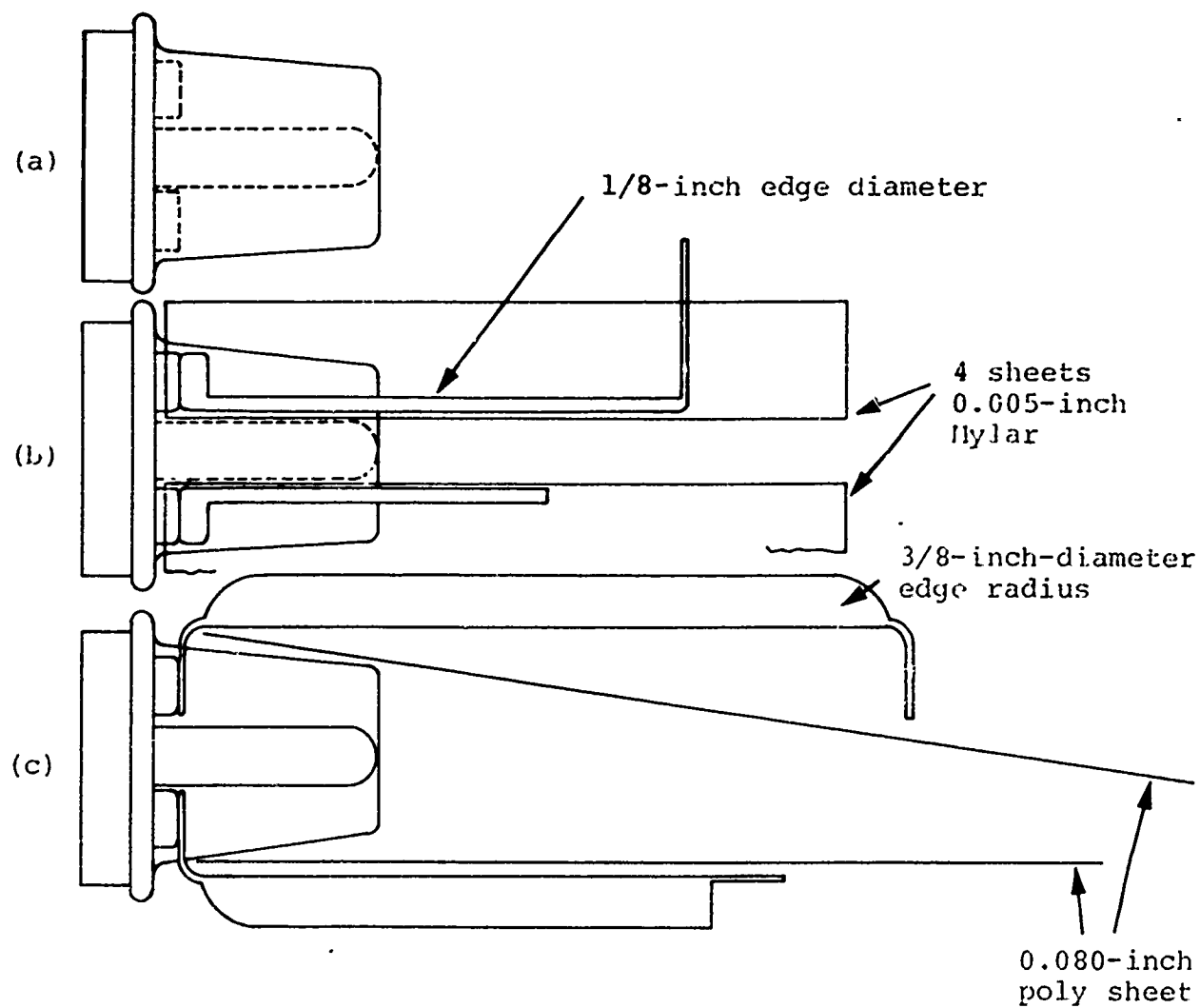


Figure 143 Connector configurations.

TABLE XVII  
CLOSE SPACED CONDUCTOR TEST RESULTS

	<u>Breakdown Voltage</u>	
	<u>SF<sub>6</sub></u>	<u>Freon 12</u>
A. No Mylar	83 kV	78 kV
B. Mylar around lower conductor only	96 kV	88 kV
C. Mylar around both plates	106 kV	95 kV

Concern was expressed in this test sequence that field enhancement associated with the abrupt ends of the conducting plates may have produced sufficient corona between conductors to initiate breakdown. Actually this is probably the case, except not associated solely with the conductor ends, i.e., the fields between conductors do exceed the breakdown field of the gas dielectric at elevated voltage and the resulting corona apparently does induce breakdown over the barrier. Lengthening the barrier and thus the arc tracking distance would probably alleviate this problem.

B.4.4 Widely Spaced Conductors. In this test sequence the stripline conductors were separated (Figure 135), thereby reducing the mean field between plates. Plastic insulation was again installed, but primarily to suppress or limit the extent of corona at the edges of the plates where the fields are high (3/8-inch-diameter edge radii). Table XVIII summarizes the results of this test series. Again, when breakdown occurred, the arc path was between rail electrodes over the barrier surface.

TABLE XVIII  
WIDELY SPACED STRIPLINE CONDUCTORS

	<u>Breakdown Voltage</u>	
	<u>SF<sub>6</sub></u>	<u>Freon 12</u>
A. No plastic (polyethylene) insulation	115 kV	110 kV
B. Lower polyethylene sheet only	140 kV	122 kV
C. Both polyethylene sheets	143 kV	124 kV

Based upon the results of these tests, widely spaced electrodes were installed on the Maxwell prototype capacitors for installation into the pulse-discharge test stand. With Freon 12 gas in the test stand, breakdowns occurred infrequently at the 100-kV charge level. Since these breakdowns could not be tolerated, SF<sub>6</sub> gas was added to the Freon 12 since the dc-test results indicated a consistent improvement of breakdown voltage by about 10 percent using SF<sub>6</sub> rather than Freon 12. A mixture of SF<sub>6</sub> and Freon 12 within the test stand eliminated further dc-breakdown problems during pulse-discharge testing.

B.4.5 Pulse-Discharge Test. All five Maxwell Laboratories prototype capacitors were installed in the test stand (Figure 135) and the load resistors adjusted to about 3.5 ohms, a value which yields a capacitor peak current of about 25 kA. This value is in keeping with the anticipated actual current that the energy-storage capacitors must supply in the TEMPS system.



Circuit inductance for each test station was approximately 85 nH, determined from analysis of the discharge waveform. A typical example of the normal discharge waveform, both calculated and measured, is shown in Figure 144 using the monitoring techniques described in Reference 15. All five capacitors were charged to full voltage (100 kV) and discharged at a rate of 1 shot per minute 24 hours per day. This discharge rate was maintained until two units had accrued over 5000 shots. Shot count is summarized in Table XIX.

TABLE XIX

MAXWELL LABORATORIES PROTOTYPE CAPACITORS  
SHOT SUMMARY--NORMAL DISCHARGE MODE

<u>Station No.</u>	<u>Serial No.</u>	<u>Shot Count</u>
1	11305	278
2	11308	3450
3	11310	5050
4	11311	5050
5	11304	1133

All units were removed from the test stand upon completion of this part of the testing and thoroughly examined. All units were satisfactory, i.e., there was no evidence of electrical or mechanical degradation.

B.4.6 Fault-Current Test Results. After the capacitors were examined, unit serial number 11305 was re-installed in the test stand, the load short circuited, and fault-current testing began.

A typical discharge-current waveform is shown in Figure 145. Analysis of the waveform yielded the equivalent circuit shown in Figure 146. Stray-series circuit inductance was approximately 190 nH. Stray-series circuit resistance was approximately 220 mΩ.

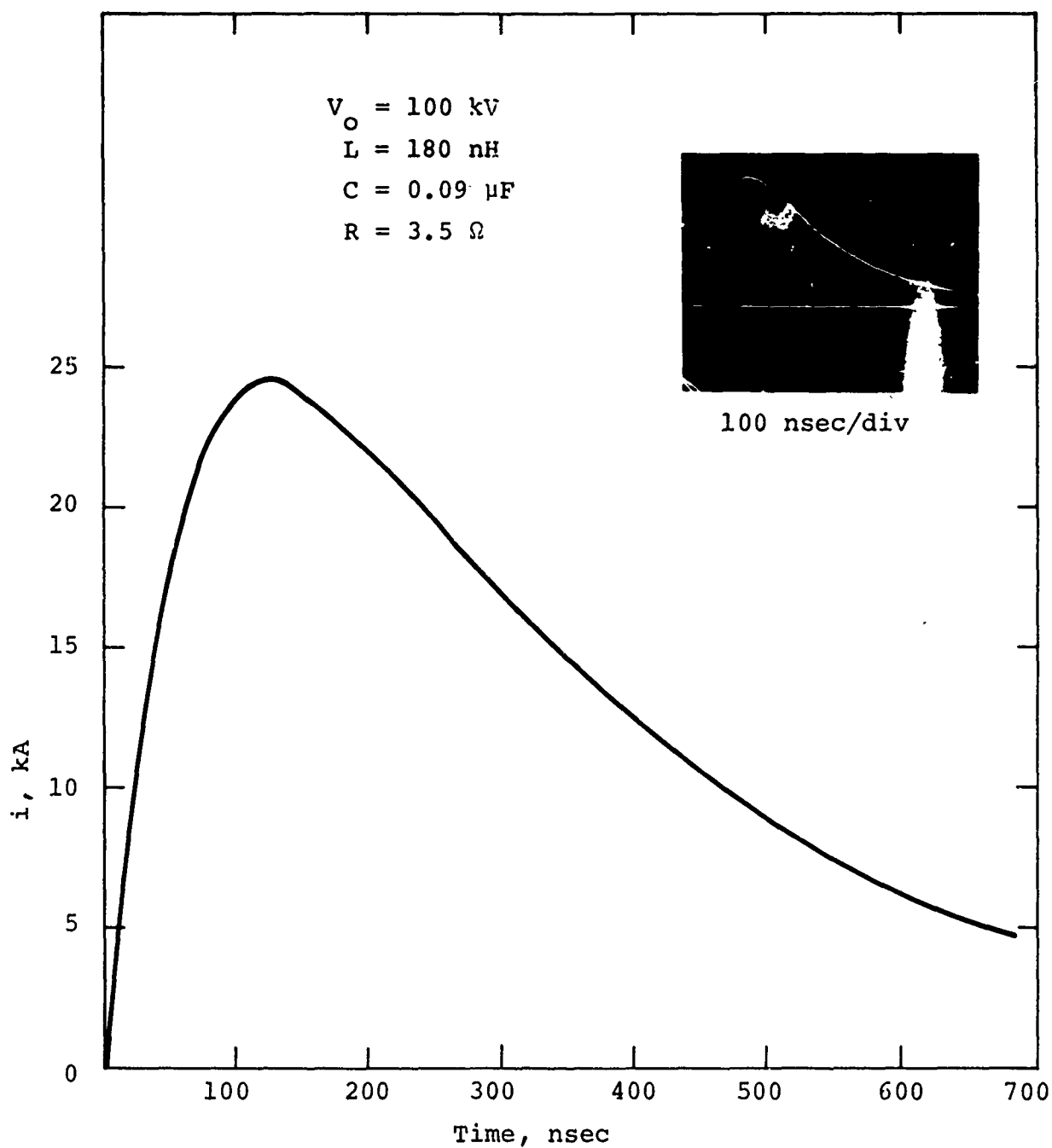


Figure 144 Maxwell prototype capacitor--normal discharge waveform.

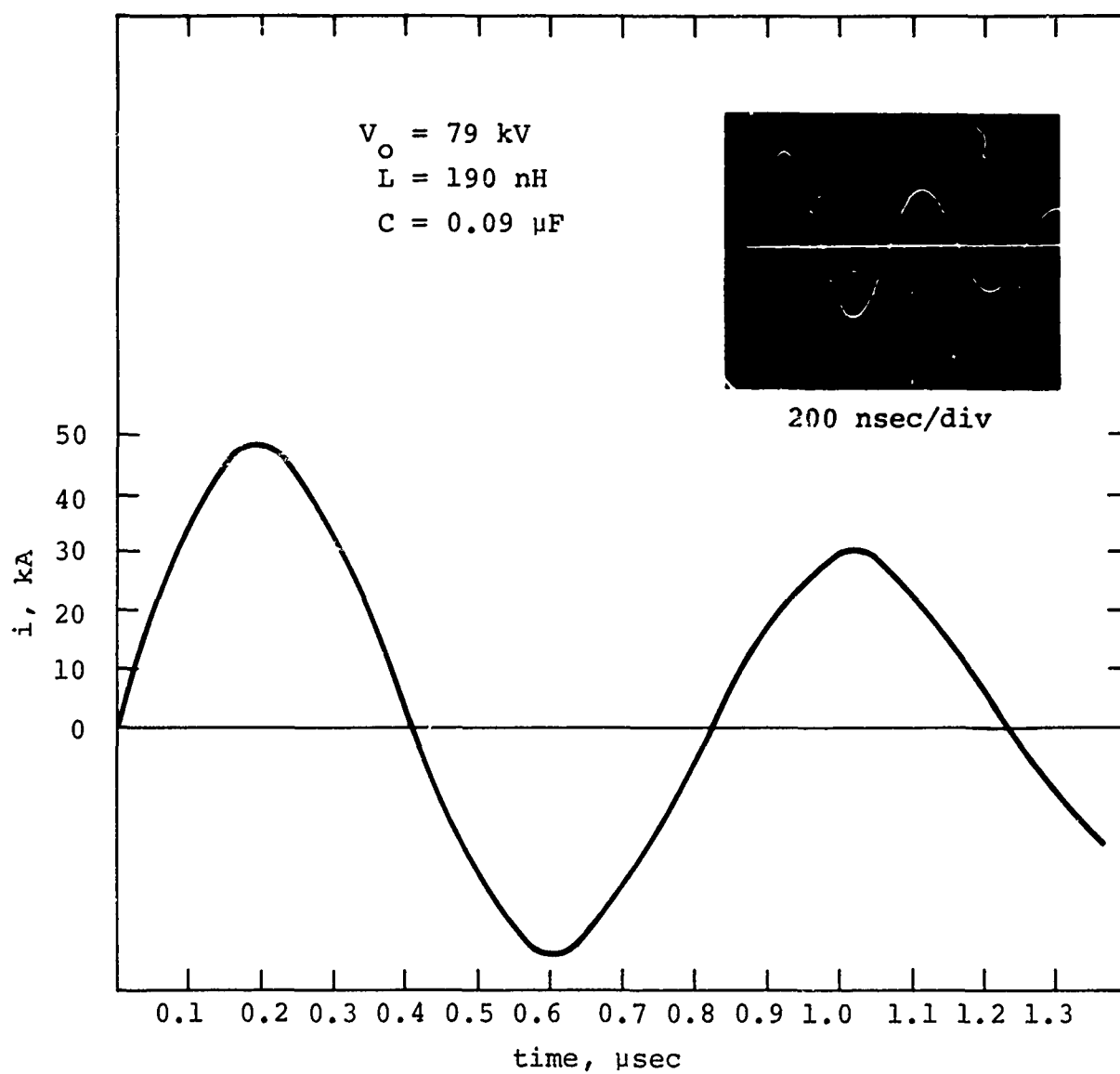


Figure 145 Maxwell prototype capacitor--fault waveform.

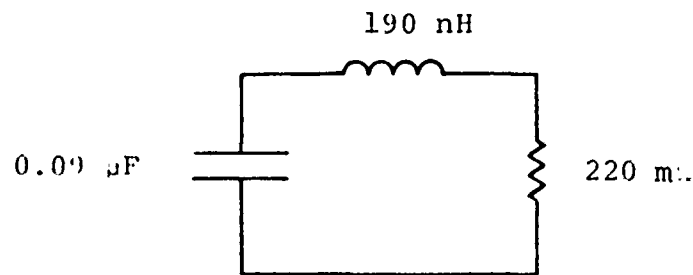


Figure 146 Equivalent circuit--fault test.

An operating level of 79 kV was chosen for this testing since peak current for this voltage is about 50 kA, comparable to that expected from TEMPS under fault conditions.

Four hundred shots were taken on the one unit tested with no failure, and testing was discontinued at the completion of this 400-shot series.

**B.4.7 Conclusions.** Pulse-discharge test results were very satisfactory for the Maxwell Laboratory prototype capacitors, and these units appear to adequately satisfy TEMPS pulse-discharge requirements. However, the dc-flashover problem encountered in the course of testing is, in our judgment, a

source of serious concern. The present design of the header is, at best, marginal at 100-kV levels. Header redesign could alleviate this problem, and if a redesign of the header is undertaken, PI recommends a retest to prove the effectiveness of the new design.

#### B.5 ENERGY STORAGE CAPACITOR INDUCTANCE AND EQUIVALENT SERIES RESISTANCE MEASUREMENT DESCRIPTION AND RESULTS

This section describes the method commonly employed at PI to determine the internal inductance and equivalent series resistance of energy-storage pulse-discharge capacitors.

The approach assumes that the circuit shown in Figure 147 is an adequate representation of the general capacitor. The degree to which the circuit of Figure 147 actually represents the capacitor under test needs to be assessed for every capacitor tested. Indeed, in some cases, this equivalent circuit is not representative.

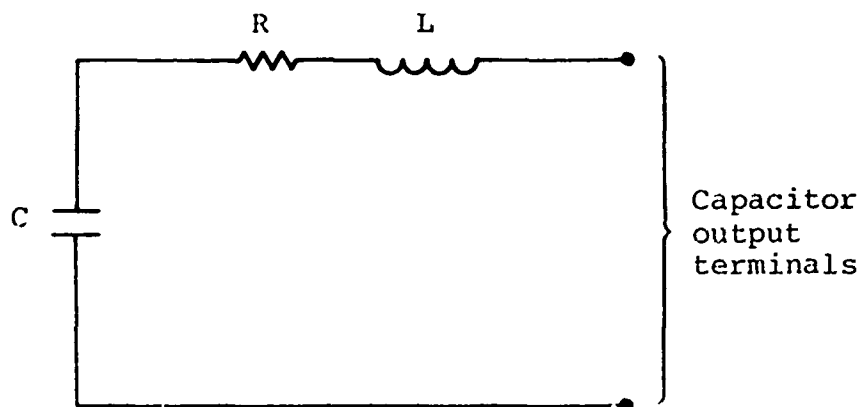


Figure 147 Equivalent circuit representation of capacitor showing internal parameters.

Before beginning a discussion of the measurement technique, a few comments with regard to the lumped element representation of Figure 146 are in order.

The capacity shown in Figure 147 is self-explanatory and is simply the capacity of the unit under test. The value of this capacity is generally determined with a standard capacitance bridge available from a number of manufacturers. Most bridges operate in a frequency range of up to 1 kHz with voltages ranging up to 1 kV, although voltages on the order of tens of volts or less are more common. For some types of capacitors, for example, high voltage ceramics, the capacity at rated stress may differ substantially from that measured at low voltage due to piezo-electric effects.

Standard energy storage capacitors of the paper-oil or film type may also exhibit capacity variations as a function of applied voltage due to small changes of effective foil spacing. In general though, with these types of capacitors, the capacity variations are very small.

A second aspect of the capacity represented by the lumped element of Figure 147 is that the actual capacity is distributed within some volume of space and as a result a finite time is required to communicate with all parts of the windings. This time, while generally short (on the order of tens of nanoseconds or less), can in some cases, depending upon how the capacitor is made, be as much as several hundred nanoseconds.

The implication here is that the rate at which energy can be drawn from a capacitor may be limited by this transit-time effect. An example of this type of performance will be discussed later.

Similar to the distributed nature of the capacity, the inductance represented by the lumped element of Figure 147 is also in part distributed throughout the windings although in most low-inductance discharge capacitors, the greater fraction of inductance is associated with internal connections within the capacitors and external connections at the circuit, and is therefore to a large degree lumped.

The manner in which connections are made to the capacitor for test purposes is important since the "internal" capacitor inductance has meaning only if the total current path is specified. As a convention at PI, capacitor inductance measurements are made with a conductor configuration that yields the lowest inductance

possible. For example, consider a tubular plastic encased capacitor with terminals at each end, as shown in Figure 148. In this example, a close fitting conducting sheath would be installed and electrically connected to one terminal. The resulting configuration is coaxial with the terminals at one end of the capacitor formed by the axial terminal and nearby conducting cylinder (Figure 149). No attempt would be made to assign an inductance to the cylindrical sheath since the "internal" inductance has significance only with the sheath installed.

The resistance represented by the lumped element in Figure 147 is associated with the distributed resistance of the metal foil from which the capacitor is made and lumped resistance associated with connections within the capacitor. This resistance may be frequency dependent due to skin effects. In general, however, foil thickness is small compared with skin depth at frequencies less than 8 and thus the equivalent series resistance is largely independent of frequency in this range.

**B.5.1 Description of Measurement Approach.** To the degree that the circuit of Figure 147 represents the equivalent circuit of a capacitor, the terminals may be short circuited and the current that subsequently flows in the closed circuit due to an initial charge on the capacitor may be calculated providing that the circuit parameters are known. Likewise, for a measured waveform and known capacity, the inductance and series resistance can be determined. The circuit of Figure 147, when short circuited, is the familiar series R-L-C circuit for which there are three types of current waveforms depending upon circuit parameters: underdamped, critically damped, and overdamped waveforms. The characteristic equations for each of these waveforms are:



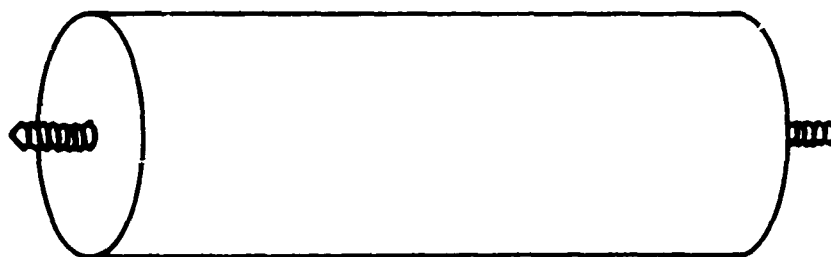


Figure 148 Tubular capacitor with end connections.

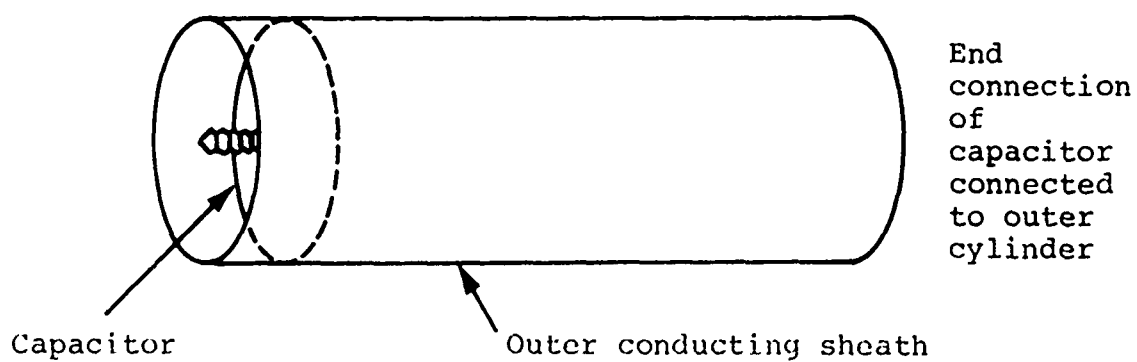


Figure 149 Conducting cylinder surrounding tubular capacitor.

By knowing the value of C by direct measurement and the value of  $\omega$  also by measurement, capacitor inductance L can be determined. In addition, the waveform is damped by the factor  $e^{-\alpha t}$ . From measurement of the decay envelope and the previously determined value for L, the equivalent series resistance can be determined since

$$\alpha = \frac{R}{2L}$$

The following section of this appendix describes the way in which the measurements are actually made in practice.

**B.5.2 Test Description.** A capacitor of well known capacitance is connected to a low-inductance shorted transmission line whose geometry is compatible with the configuration of the electrode connections of the capacitor. The purpose of such a transmission line is to provide an external inductance across which the oscillatory voltage waveform may be monitored and to complete the circuit shown in Figure 147. In practice the shorted transmission line should be of smaller inductance than the expected inductance of the capacitor and should also be theoretically calculable with reasonable accuracy. By using a very low-inductance transmission line with a value much less than that associated with the capacitor, slight errors in the calculated inductance will have little influence upon the total inductance of the circuit. The external inductance must not be so small, however, that the inductive voltage division of the circuit produces an undetectable signal.

Figure 150a and b shows the installation of a shorted stripline (parallel plate) transmission line on a capacitor under test. Note the voltage signal tapped from the transmission line.

In Figure 151, the equivalent circuit is shown indicating the effective inductance across which the voltage waveform is monitored.

The voltage across the load inductance produced by switching the dc charged capacitor into the load is given by

$$V_L = L_{\text{ext}} di/dt$$

The monitor signal is tapped off a fraction of the external load inductance and thus the monitor waveform is

$$V_M \approx V_C \frac{L_p}{L'} \cos \omega t$$

In this case,  $L_p$  is monitor inductance,  $L'$  is total circuit inductance, and  $V_C$  is capacitor initial charge voltage. The angular frequency of oscillation (low loss circuit)  $\omega$  is given approximately by

$$\omega = \left( \frac{1}{L'C} \right)^{\frac{1}{2}}$$

or in terms of the period

$$T = 2\pi(L'C)^{\frac{1}{2}}$$

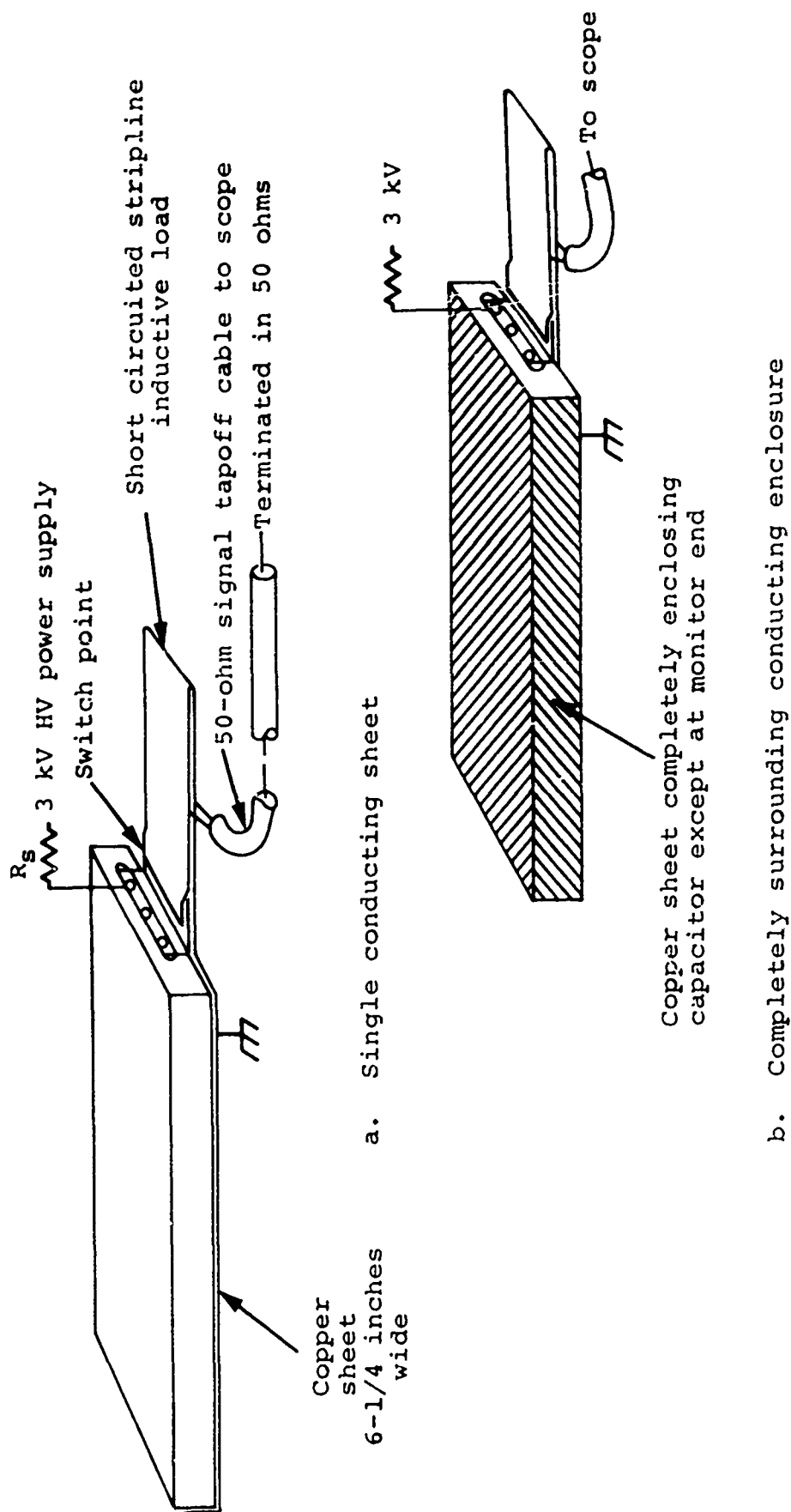


Figure 150 Capacitor test configurations.

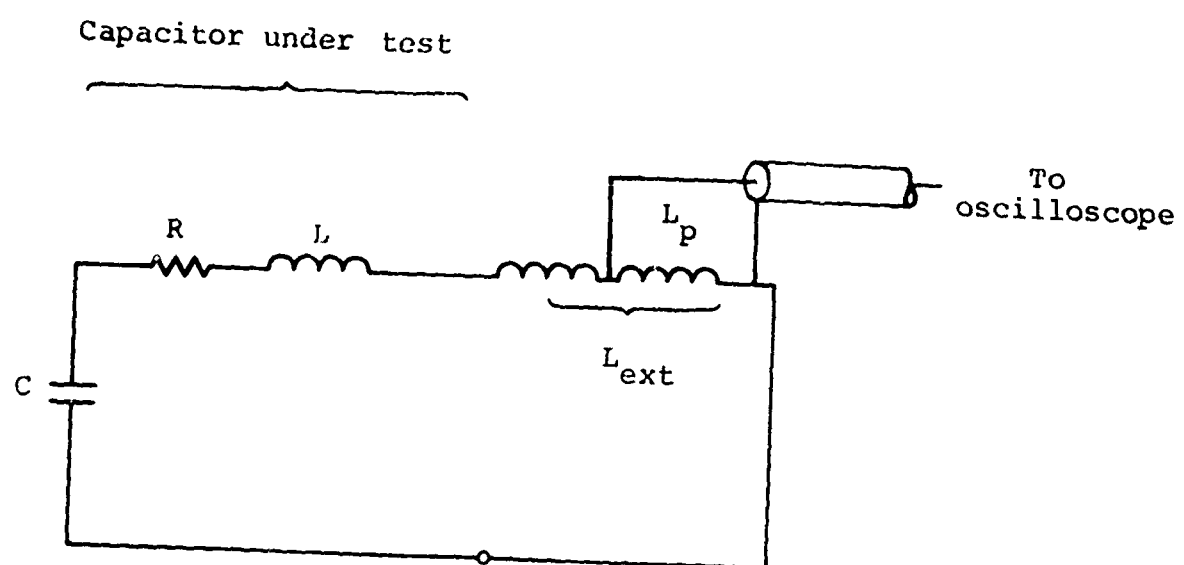


Figure 151 Capacitor and load circuit.

(a) Underdamped  $\omega^2 > \alpha^2$

$$i(t) = \frac{V_0}{j\beta L} e^{-\alpha t} \sin j\beta t$$

where

$$\alpha = \frac{R}{2L}$$

$$\omega = \frac{1}{\sqrt{LC}}$$

$$\beta = \sqrt{\alpha^2 - \omega^2}$$

(b) Critically damped  $\alpha^2 = \omega^2$

$$i(t) = \frac{V_0}{L} t e^{-\alpha t}$$

(c) Overdamped  $\omega^2 < \alpha^2$

$$i(t) = \frac{V_0}{2L\beta} \left[ e^{-(\alpha-\beta)t} - e^{-(\alpha+\beta)t} \right]$$

Of these characteristic equations the underdamped case is the most frequently encountered when dealing with pulse discharge capacitors, since the equivalent series resistance is generally quite small.

For the case, then,  $R$  is small,  $\alpha^2 \ll \omega^2$  and the circuit is oscillatory with angular frequency

$$\omega = \frac{1}{\sqrt{LC}}$$

Figure 152 illustrates a typical waveform using the measurement and monitoring circuit technique described above.

In Figure 152, a high frequency oscillation is superimposed upon the capacitor discharge oscillation in early pulse times. This hf "hash" is due to multiple wave reflections within the shorted transmission line inductive current monitor.

#### B.5.2 Departure From Lumped Circuit Representations.

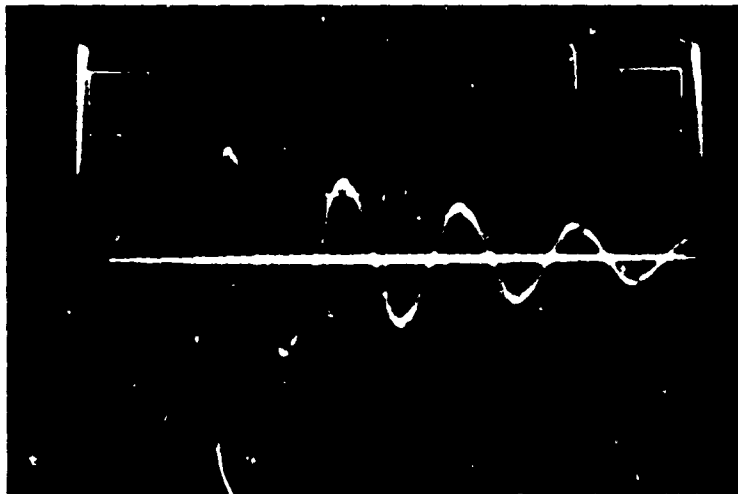
Using the previously discussed measurement technique often yields output waveforms which deviate substantially from a pure damped cosinusoid, depending upon the way in which the capacitor under test is constructed. A typical example is illustrated in Figure 153 where the waveform is characteristic of a stripline discharge into a load inductance. The initial waveform decay  $\tau_d$  is given by

$$\tau_d = \frac{L}{Z_0}$$

where  $L$  is the sum of internal and external lumped inductance and  $Z_0$  is the effective characteristic impedance of the capacitor viewed as a stripline. The double transit time of the capacitor, as illustrated by the waveform of Figure 153, is clearly evident by the "break" in the initial waveform decay.

The capacitance of the unit, in conjunction with the effective one-way transit time through the unit, permits calculations of the effective wave impedance  $Z_c$  and equivalent transmission line distributed inductance, i.e.

$$Z_c = \frac{\tau}{C}$$



Vertical: 0.5 V/division  
20/1 attenuation

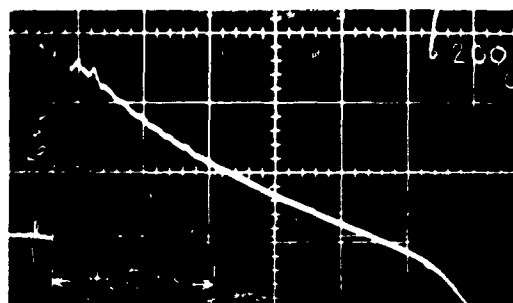
Horizontal: 500 nsec/division

$V_{dc} \approx 3 \text{ kV}$

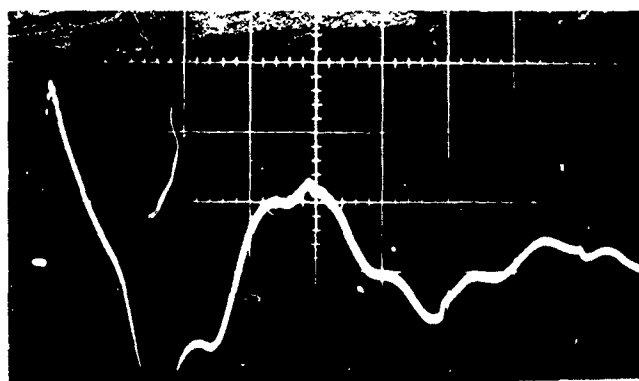
$L_p \approx 1 \text{ nH}$

Figure 152 Capacitor inductance measurement monitor output waveform.





Time Scale: 0.2  $\mu\text{sec}/\text{cm}$



Time Scale: 1  $\mu\text{sec}/\text{cm}$

Figure 153 Output waveform,  $L_m = 29 \text{ nH}$ .

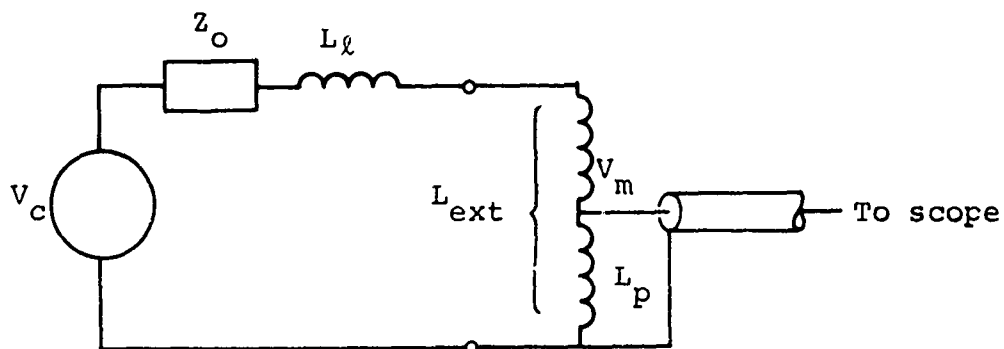
and

$$L_t = \frac{\tau^2}{C}$$

To the transmission line inductance,  $L_t$  above, must be added the internal lumped inductance to determine total capacitor inductance. Lumped inductance  $L_\ell$  may be determined from the expression

$$L_\ell = \frac{V_c}{V_m} (L_p - L_{ext})$$

where  $V_c$  is initial capacitor charge voltage,  $L_p$  is inductive load monitor inductance, and  $L_{ext}$  is the total external load inductance (Figure 154).



$$L_x = \frac{V_c}{V_m} L_p - L_{ext}$$

Figure 154 Stripline capacitor equivalent circuit.

B.5.3 Internal Inductance Determination. For a capacitor, which may be represented by the equivalent lumped circuit of Figure 154, the total circuit inductance can be calculated from the measured period of oscillation, i.e.,

$$L' = \frac{T^2}{4\pi^2 C}$$

Since this value  $L'$  is the sum of internal external capacitor inductance, the total external inductance in the circuit must be subtracted from  $L'$  to obtain the equivalent series inductance present within the capacitor.

The equivalent series resistance may be determined by measuring the e-fold decay time of the oscillatory envelope of the waveform and applying the formula

$$\tau(\text{e-fold}) = 2L'/R \text{ where } L'$$

is again the total circuit inductance.

The stripline transmission line monitors used for the previously described measurements are generally constructed of copper sheet folded over at one end to provide the shorted end of the transmission line. Solid dielectric sheet is used to space the conductors and the capacitors are generally dc charged to 2 to 3 kV and switched by way of a "thumb-tack" or equivalent switch. Charge voltages of this magnitude are required since the arc formed at the switch is reasonably "hot" and does not, under these conditions, contribute significantly to the total equivalent series resistance.

The expected waveform from a discharging stripline of impedance  $Z_0$  is shown in Figure 153 with the equivalent circuit shown.

In every case, the distinct later-time oscillations should be used for the determination of the inductance.

As indicated previously, the total circuit inductance can be calculated from the period of oscillation, that is,

$$L' = \frac{T^2}{4\pi^2 C}$$

Since this value  $L'$  represents both the internal-capacitor external-transmission-line inductance of the circuit, the total external inductance in the circuit must be subtracted from  $L'$  to obtain the equivalent series inductance present within the capacitor.

The equivalent series resistance may be determined by measuring the e-fold decay time of the oscillatory envelope of the waveform and applying the formula

$$\tau(\text{e-fold}) = 2L'/R$$

where  $L'$  is again the total circuit inductance.

The stripline geometries used in this experiment were constructed of copper sheet folded over at one end to provide the shorted end of the transmission line. Mylar sheets separated the stripline. Minor modifications were required to accommodate the capacitor samples under test and any additional connections were included in the external inductance estimates. The capacitors were dc-charged to 2 to 3 kV and switched by a low-inductance mechanical switch.

Voltages of this magnitude must be used to produce a sufficiently hot arc across the switch, thus reducing equivalent series arc resistance in the circuit. Between the stripline top plate and connecting strip from the capacitor electrode was a small overlap separated by one 1 mil of Mylar, with a very small air gap of compatible length existing between the two strips. A hole had been cut through this Mylar, and to discharge the capacitor this air gap was closed by pressing the two overlapping strips together. The inductance of the closing arc was insignificant and neglected. The waveform produced was recorded by a Tektronix 454 scope.

B.5.3 Results. By using the method of this experiment to measure inductance and resistance of a capacitor, the following values were found.

<u>Manufacturer</u>	<u>Type capacitor (<math>\mu</math>F)</u>	<u>Internal L (nH)</u>	<u>Series R (m<math>\Omega</math>)</u>
Maxwell Laboratories	Catalog No. 31179 0.01	26	140
Condenser Products	0.2	19	42

APPENDIX C

PROTOTYPE MARX GENERATOR SWITCH EVALUATION

## C.1 PURPOSE

The purpose of this experimental program was to design, construct, and test prototype Marx generator switches to evaluate voltage variability characteristics using pressurized  $N_2$  and  $SF_6$  gases, and to determine switch self-fire characteristics.

The use of pressurized gas Marx switches with high electric fields within the spark gaps was proposed (Reference 1) to speed Marx erection and reduce timing jitter, if this could be done without increasing self-fire probability.  $SF_6$  gas was proposed to obtain high electric fields with minimum pressure. The maximum safe operating pressure, found by measurement, would be used for the maximum operating voltage of the Marxes, and this would determine the voltage operating range. Output voltage is reduced by lowering both the dc operating voltage and spark gap pressure. At some point, further reduction in voltage leads to excessive Marx erection timing jitter. Experience with SIEGE II showed that changing from  $SF_6$  to  $N_2$  in the switches extends the low jitter range of the Marx, and it is estimated that this operation could supply a 3/1 total voltage range for TEMPS.

The experimental work described here is preliminary to construction and test of a prototype Marx generator, where, in addition to other test objectives, Marx erection delay and timing jitter will be evaluated. The experimental work described here had as its primary objectives, the determination of the design of prototype Marx switches that satisfy voltage range requirements, to assess and minimize spark gap self-fire probability, and to assess switch reliability and life.

Rail type sparks were investigated since these are most compatible with the low-inductance Marx generator configuration.

Each switch is equipped with a midplane trigger electrode which, in the Marx, were resistively coupled to earlier stages of the Marx to help speed Marx erection and reduce timing jitter.

Each switch operates a maximum dc voltage of 100 kV and passes a peak current of approximately 45 kA, although infrequent fault currents of approximately 90 kA may be experienced. In addition, for normal conditions, each switch passes about 18 mCb of charge.

## C.2 DESCRIPTION OF APPROACH

Experience has shown that the switch characteristics are dependent upon total charge passing through a switch besides the peak current and voltage. It becomes apparent that a mere evaluation of a switch's characteristics does not suffice unless actual operating conditions exist such that total charge, current, and voltage are comparable to those that will be experienced in the full system. It is the intention of this experiment to best evaluate each prototype switch under these conditions.

The requirements placed upon the full system dictated the requirements to be met by each Marx switch which can be determined by statistical extrapolation. Theoretical statistical extensions from 1 to n switches were formulated by studying over a great many shots the performance of a single switch.

The Marx was to have 70 gaps and as a start a normal Gaussian distribution was assumed for the self-fire voltage  $V_i$  of a gap with standard deviation  $\sigma_i$  at fixed pressure  $P_i$  (Figure 155).



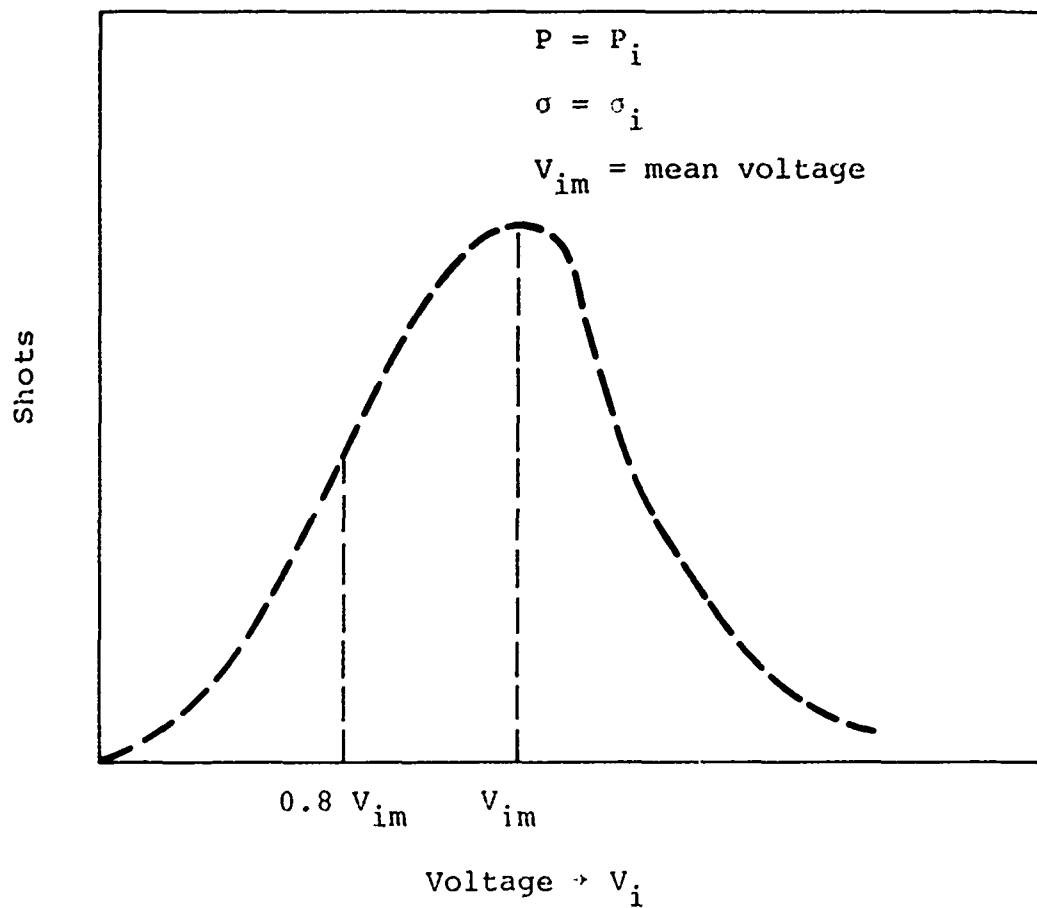


Figure 155 Statistical curve for a single switch.

Assume 80 percent of self-fire operation at fixed pressure  $P_i$ , and that the probability of a self-fire of the 70 switches [ $P_{70}$  (SF)] in series is to be arbitrarily 0.01. If the probability of command fire of a single switch is found to be  $P_1$  (cf), which is that ratio of shots occurring above  $0.8 V_i$  to the total shots taken at fixed pressure  $P_i$ , statistically one finds that

$$P_{70}(\text{SF}) = 1 - [P_1(\text{cf})]^{70} = 0.01$$

or

$$P_1[\text{cf}] = 0.9998$$

that is, > 9998 out of 10000 shots for a single switch must fall above  $0.8 V_i$  at fixed pressure  $P_i$  in order to meet the < 1 percent self-fire specification set upon the full system.

Now, by knowing that 99.98 percent of the shots of a single gap must fall above  $0.8 V_i$  we know that within the range of  $3.615 \sigma_i$ , 99.98 percent of the shots occur. Therefore,

$$0.2 V_i = 3.72 \sigma_i$$

or

$$\frac{0.2}{3.72} = \sigma_i/V_i = 0.0536$$

A great many shots are planned for each switch under test since the difference between having a 1 percent self-fire probability and a 5 percent self-fire probability for the full system can only be resolved over a large sampling. A 1 percent self-fire occurrence would show  $P_1(\text{cf}) = 0.9998$  while a 5 percent self-fire occurrence would show  $P_1(\text{cf}) = 0.9992$ . Therefore, at least a few thousand shots would be required for statistical resolution.

The problem of simply extending the outcome of one switch to that of  $n$  switches may be solved to a good approximation on a purely statistical basis. However, a more tangible method appears to be based on a comparative study of Marx switch performance using the SIEGE switches and the prototype TEMPS switch. Many data are available concerning SIEGE Marx operation, including the self-fire voltage versus pressure for each Marx utilizing 17 such switches. In addition, the number of prefire occurrences for the entire SIEGE Marx has been recorded. With the characteristics of a single SIEGE switch and a TEMPS prototype switch and the data obtained from a 17-switch SIEGE Marx, much useful information can be obtained as to the relative performance of a 70-stage TEMPS Marx.

The TEMPS prototype rail switch used throughout this test is shown in Figure 156a. The outside dimensions of the Lucite envelope are  $2\frac{1}{2}$  inches x  $2\frac{1}{2}$  inches x 18 inches. Each end has threaded end plugs which are O-ring sealed and the switch is rated at a maximum working pressure of 30 psig. Within its 1.850 inch bore are two brass  $11/16$ -inch-diameter electrodes spaced 0.500 inch apart with an effective gap spacing of 1.05 cm due to the field enhancement of 1.21.

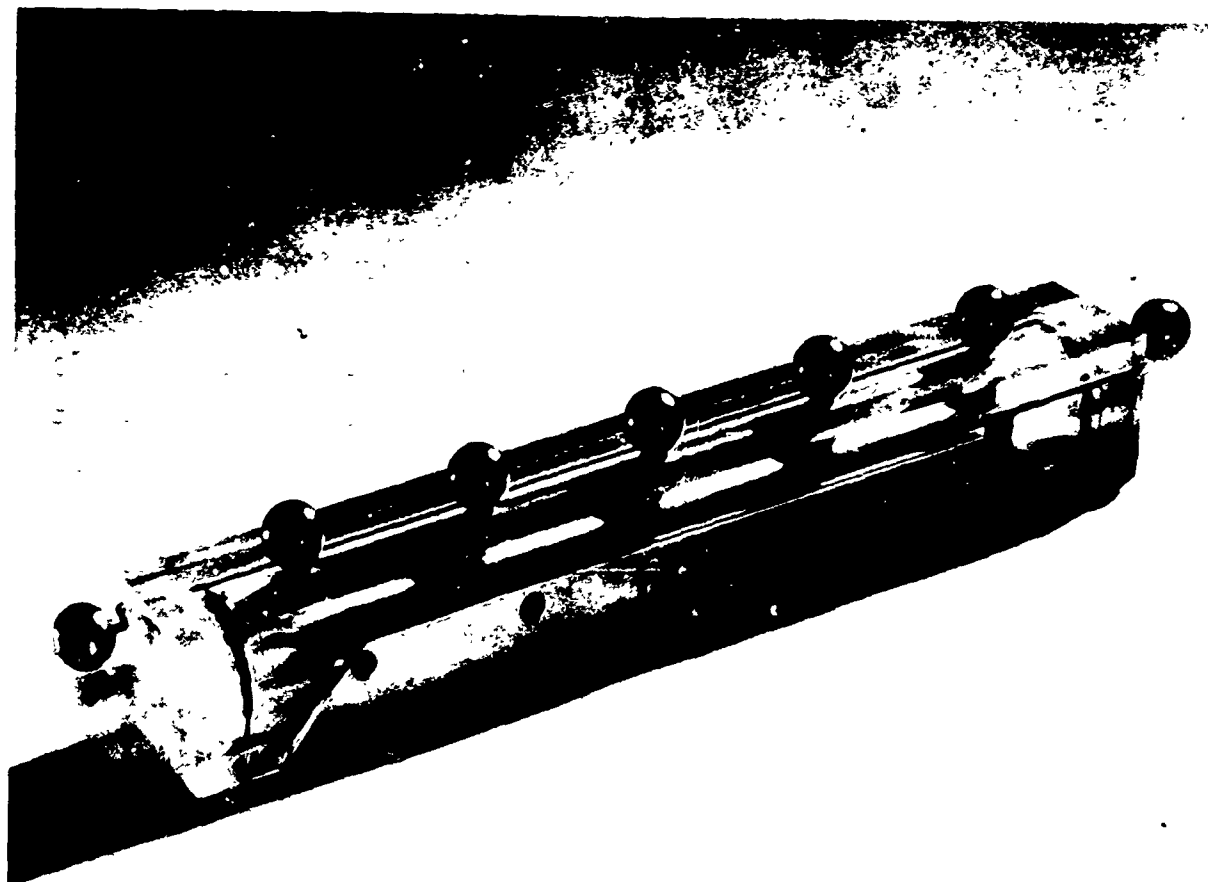


Figure 156a Prototype Marx switch.

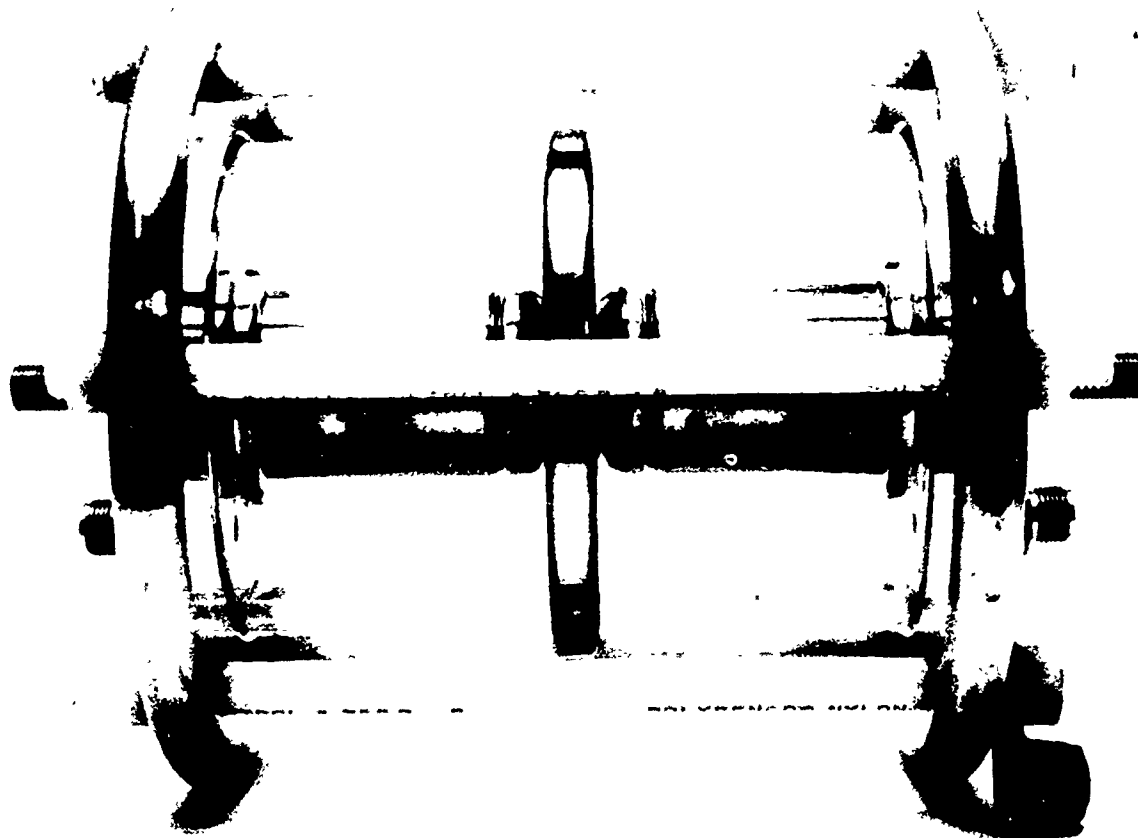


Figure 156b Prototype SIEGE switch.

Connection is made to the capacitors by means of two parallel copper sheets which are contoured to the outside dimensions of the switch envelope and form two contacting surfaces which are pressed onto banana plug capacitor connections. A Lucite fence insulates the two switch connectors from each other.

A SIEGE switch is shown in Figure 156b. Its gap spacing is 1.25 cm and is equipped with a midplane.

### C.3 DESCRIPTION OF EXPERIMENT

Each switch prototype is to be placed on a low-inductance test stand shown in Figure 157. The capacitors are 0.4  $\mu\text{F}$  at 50 kV and are arranged to give 0.2  $\mu\text{F}$  circuit capacitance. The estimated circuit inductance is approximately 300 nH and a load of 2 ohms, which is nearly the critical resistance for the test circuit, is used.

The expected currents which pass through the circuit are expected to be somewhat lower than the required 50 kA due to the relatively high series inductance. The types of capacitors used have a great deal of inductance associated with the bushing type connectors; however, the availability of these capacitors required their usage.

Assuming a critically damped circuit, the peak currents were expected to be on the order of 37 kA or 74 percent of that current,  $V/R$ , produced in a purely RC circuit. Peak voltage applied to the gap is approximately 100 kV ( $\pm 50$  kV) and the total charge passing through a prototype switch is, for a

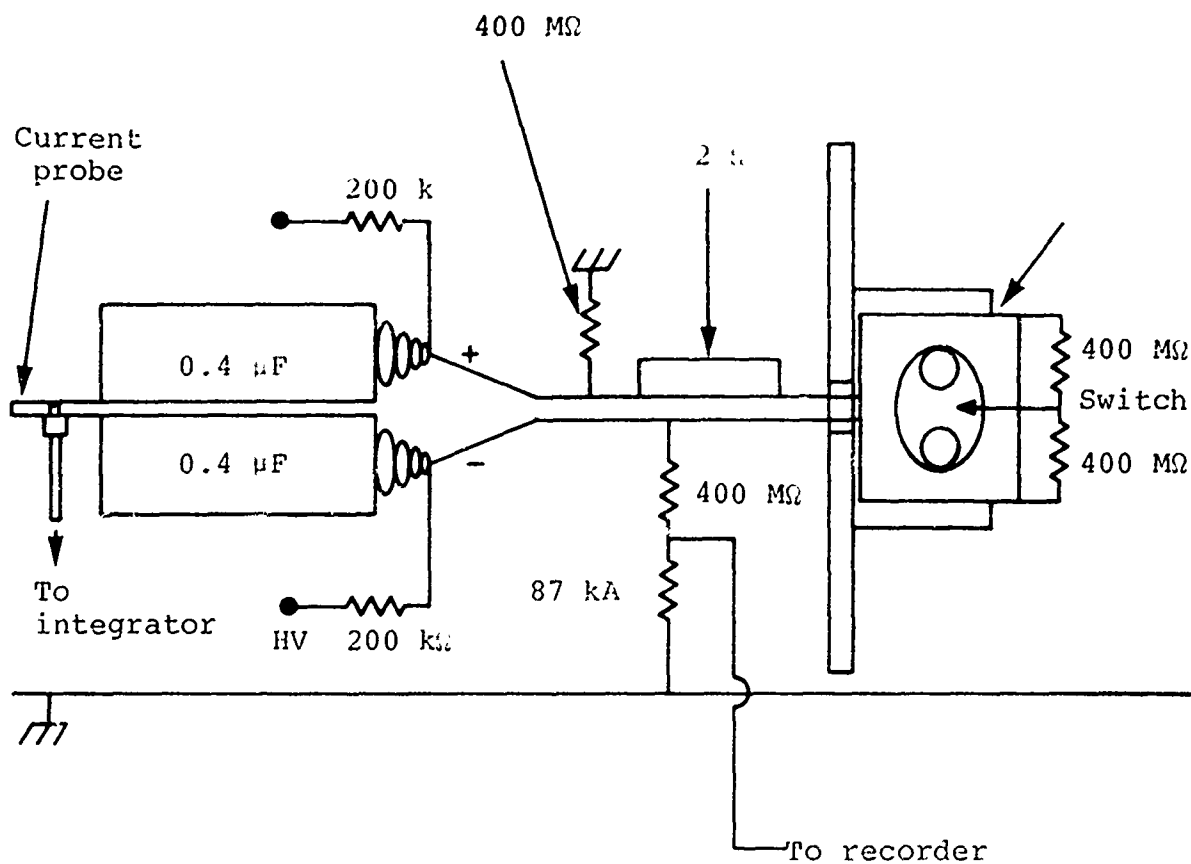

$$\text{total } C = 0.2 \mu F$$
$$L = 300 \text{ nH}$$
$$R = 2 \text{ ohms}$$
$$R_{\text{CRIT}} = 2.4 \text{ ohms}$$

Figure 157 Test stand.

critically overdamped circuit,  $V_0 C$  or

$$(100 \times 10^3)(0.2 \times 10^{-6}) = 20 \times 10^{-3} \text{ Cb}$$

per shot, comparable to that expected in the TEMPS system.

The currents produced by the circuit were monitored by means of a current loop probe that was placed in series with the circuit.

The signal yielded by such a probe is due to the inductive voltage drop across and is related to the  $di/dt$  of the circuit. This signal is integrated by means of a 40  $\mu$ sec integrator and displayed on an oscilloscope screen. The voltage  $V(t)$  recorded is related to the current flow in the circuit by the relation

$$i(t) = \frac{L_p}{RC} V(t)$$

where  $L_p$  is the inductance of the probe across which the voltage is monitored and  $RC$  is the time constant of the integrator.

The self-break voltages for each shot were recorded by means of a strip chart recorder which monitored every charge cycle. Each charge cycle was adjusted so as to be in keeping with the proposed charge time of the TEMPS system which is close to 20 to 30 seconds.



Some triggering of the prototype rail switch will be done in order to evaluate its performance with regard to the consistency of self-break voltage.

The possibility that the relative smoothness of the midplane knife edge influences self-fire behavior was evaluated since, by triggering the gap, the midplane was expected to become burned and its surface smoothness degraded. Triggered shots at a given gas pressure  $P_0$ , taken alternatively with self-break shots at the same pressure, were taken. Over a great many shots, any inconsistency in the self-break voltage was observed.

#### C.4 EXPERIMENTAL RESULTS

Towards the end of the SIEGE testing program a great deal of prefires occurred in the SIEGE Marxes. Prefiring became more prevalent as higher peak currents and more charge flow were achieved by charging to higher voltages. On occasions, prefire occurred up to 20 percent of the time, especially after continued high-voltage operation or more specifically after a fault condition in which peak currents much greater than normal were produced.

When tested for its self-fire voltage versus spark gap pressure, the SIEGE Marxes appeared to have standard deviations on the order of 5 percent which, when extrapolated statistically, would be expected to produce a much lower prefire probability. Some account can be made for the small percent standard deviations. The basis for such figures were a sample size of 10 to 20 shots. One or two of these shots fell much below the mean self-break voltage, but were thrown out on the basis that they would lower the mean

value by too great an extent. Some shots that were thrown out fell below that percentage of the mean self-break voltage and would have been considered prefires had the system been normally charged for a command fire. Extrapolating these figures to a thousand or more shots and applying the probability theory discussed in the preceding section, a higher prefire rate would have been expected. Nevertheless, prefire was a definite problem at higher spark gap pressures of 20 psig or more where standard deviations tended to be the greatest.

A random sample of used SIEGE switches was tested, taking each switch separately. The results showed behavior quite surprising since erratic behavior of the system was thought to have originated from that of each switch. In general, out of the six SIEGE switches, five produced self-fire voltages very consistent with standard deviations on the order of 1 percent or less over hundreds of shots. On the other hand, one gap showed quite erratic behavior, although at no time during the hundreds of shots taken did a self-break occur below 86 percent of the mean self-break voltage at that given pressure. Figure 158 shows the frequency versus self-break voltage obtained from 150 shots at 15 psig  $N_2$ . This is an intermediate value above which standard deviations for the SIEGE Marx became relatively large and below which it was quite small. The standard deviation for this sample was 3.5 percent.

The TEMPS rail switch self-break voltages are shown in Figure 159 for  $N_2$ ,  $SF_6$ , and a 14 percent  $SF_6$ /86 percent  $N_2$  mixture. Since the overlap in breakdown voltages of  $SF_6$  and  $N_2$  occurs at 30 psig  $N_2$ , the gas mixture was intended to provide a midrange that would limit the maximum gap pressure to 15 psig  $N_2$  in the event the higher pressures produce a larger than normal scatter in the self-break voltages.

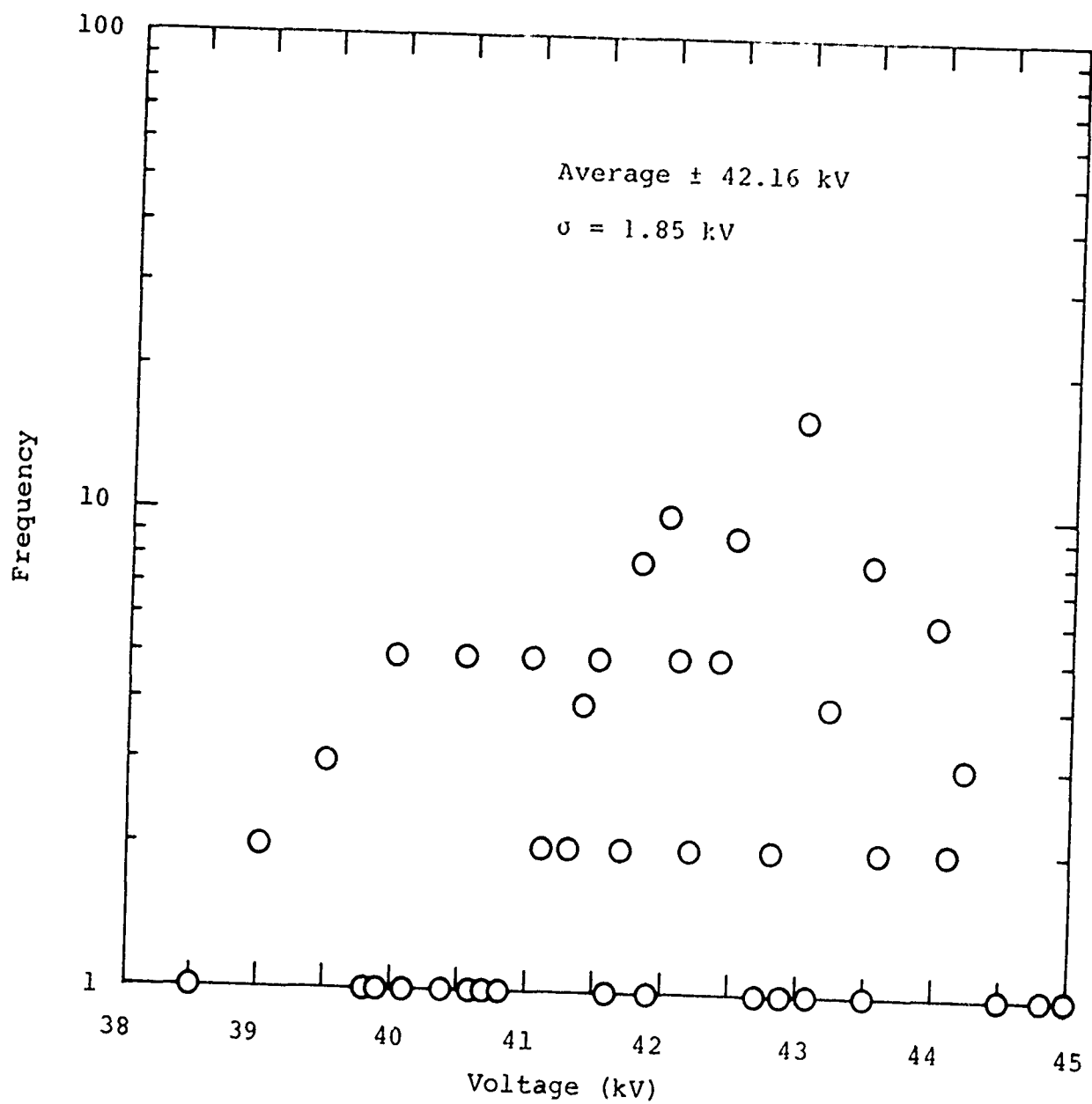


Figure 158 SIEGE gap (used), S194, 15 psig  $N_2$ , ~ 150 shots.

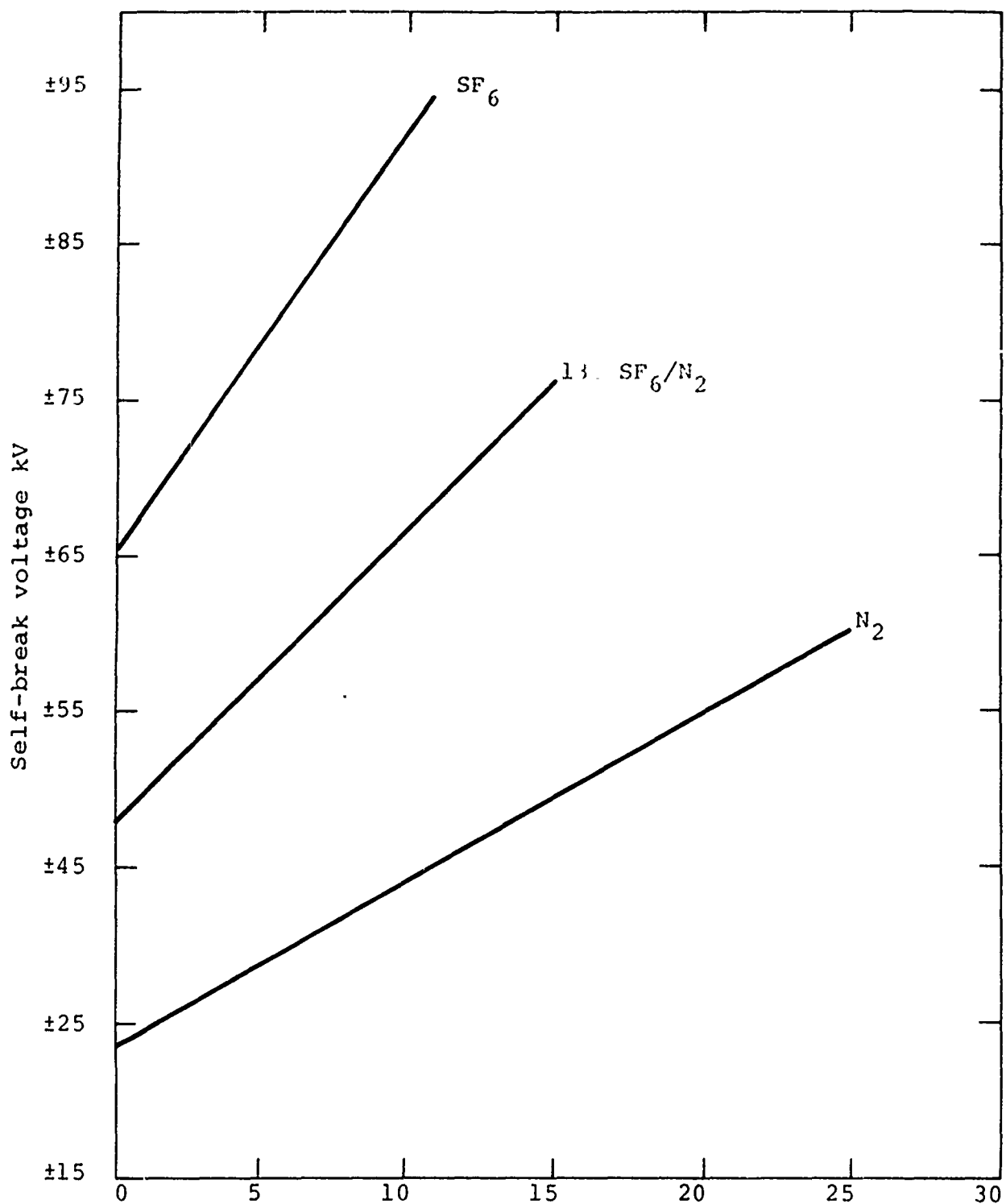


Figure 159 TEMPS Marx switch self-break voltage versus pressure.

Typical frequency versus self-break voltage charts are shown in Figures 160 through 162 for the TEMPS switch operated at 15 psig and 25 psig  $N_2$ . For the lower pressures, the standard deviations were insignificant over hundreds of shots and not calculated.

Probably the most interesting observation is the comparative performance of a SIEGE switch at 15 psig  $N_2$  to the TEMPS switch under identical conditions. The consistency of the TEMPS switch is remarkably better even with over 2500 shots accumulated on the switches and having had for at least 1000 shots passed peak currents of 28 kA as recorded by the current probe. The waveform of the current is shown in Figure 163.

The tendency of the TEMPS switch at 25 psig  $N_2$  pressure to have a larger statistical scatter may justify the use of the gas mixture; however, the performance at 25 psig  $N_2$  appears tolerable since no shots in approximately 1600 fell below 83 percent of the mean.

An additional 500 shots were taken with the TEMPS switch at 25 psig  $N_2$ . In an alternating sequence 250 shots were allowed to self-break while every other shot was triggered as the voltage came within 5 kV or its self-break voltage. A 70 kV pulse triggered the midplane.

The results of the latter test are shown in Figure 164 where one notes a slight increase in the standard deviation from previous iterations at the same pressure. One shot noted fell at 83 percent of the mean voltage, unchanged from the previous statistical results.

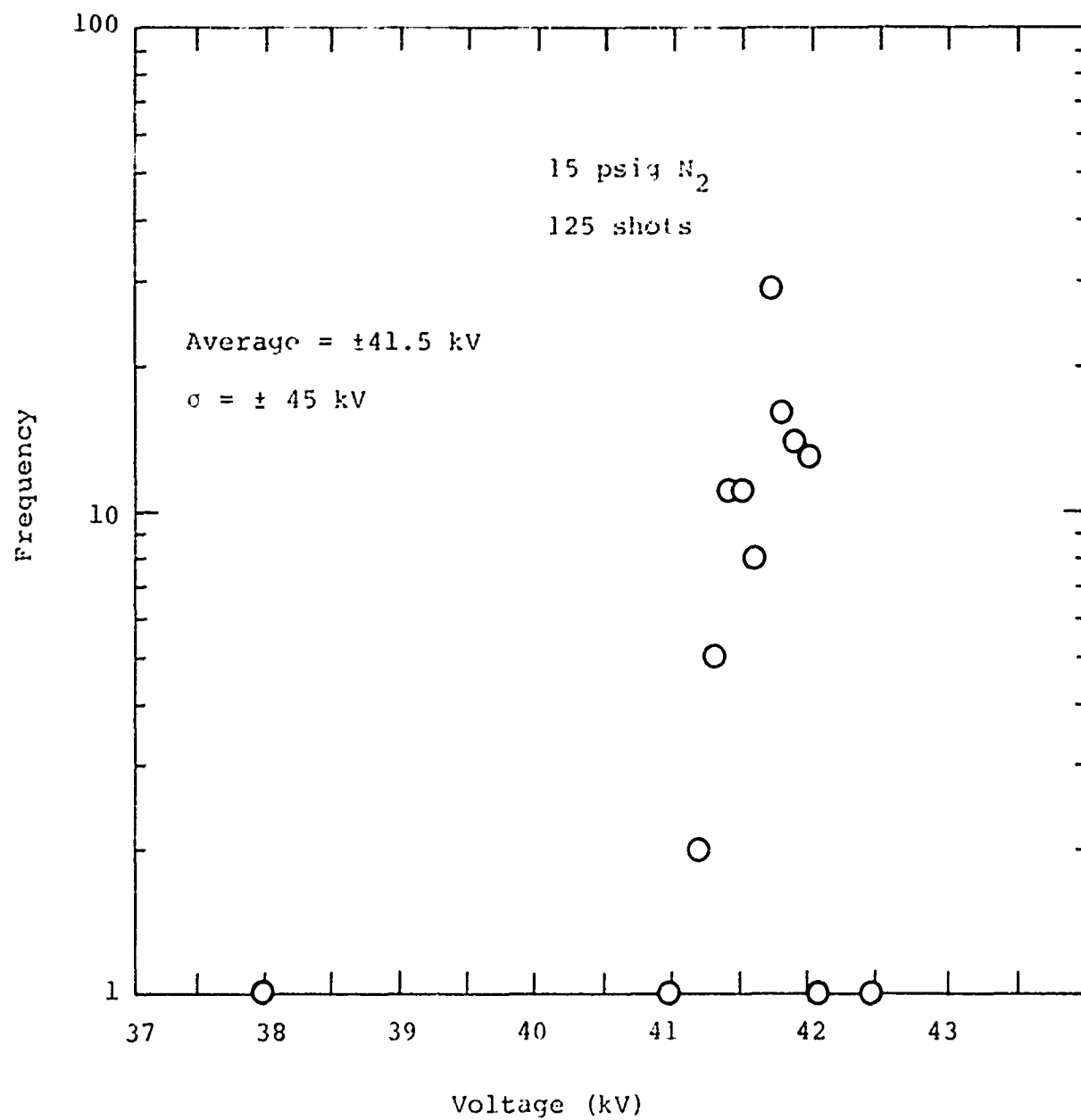


Figure 160 TEMPS prototype.

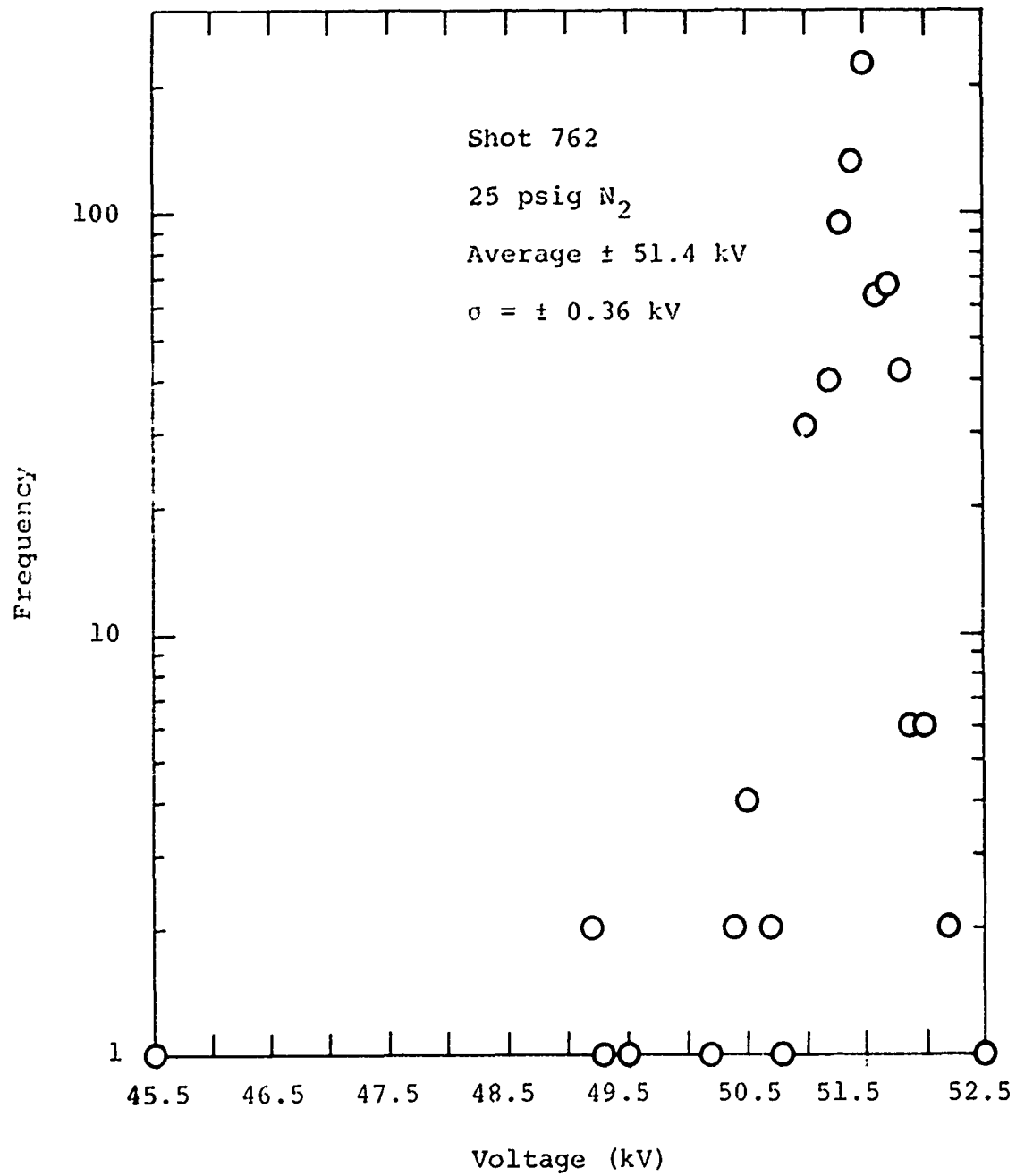


Figure 161 TEMPS prototype.

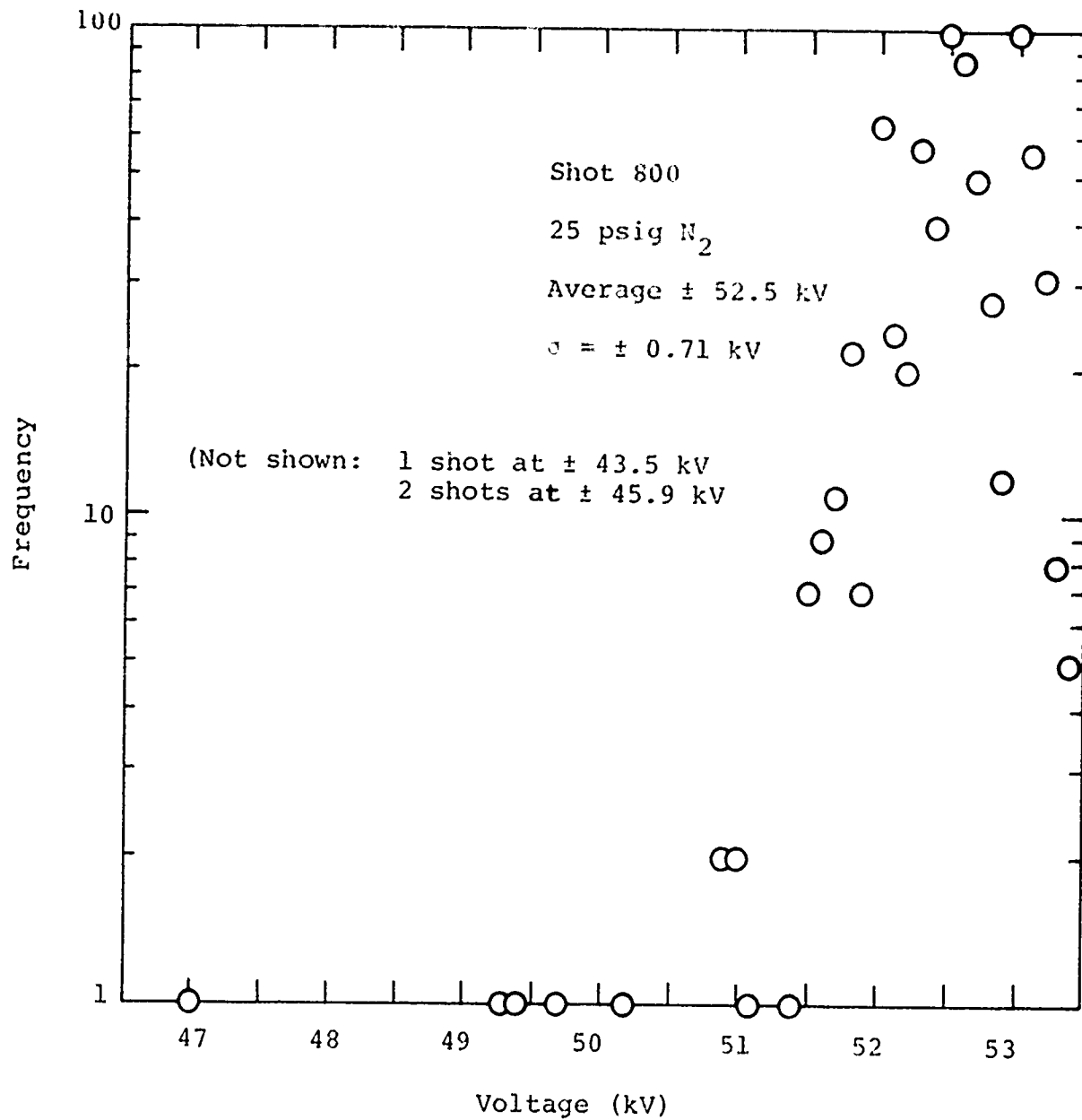


Figure 162 TEMPS prototype.



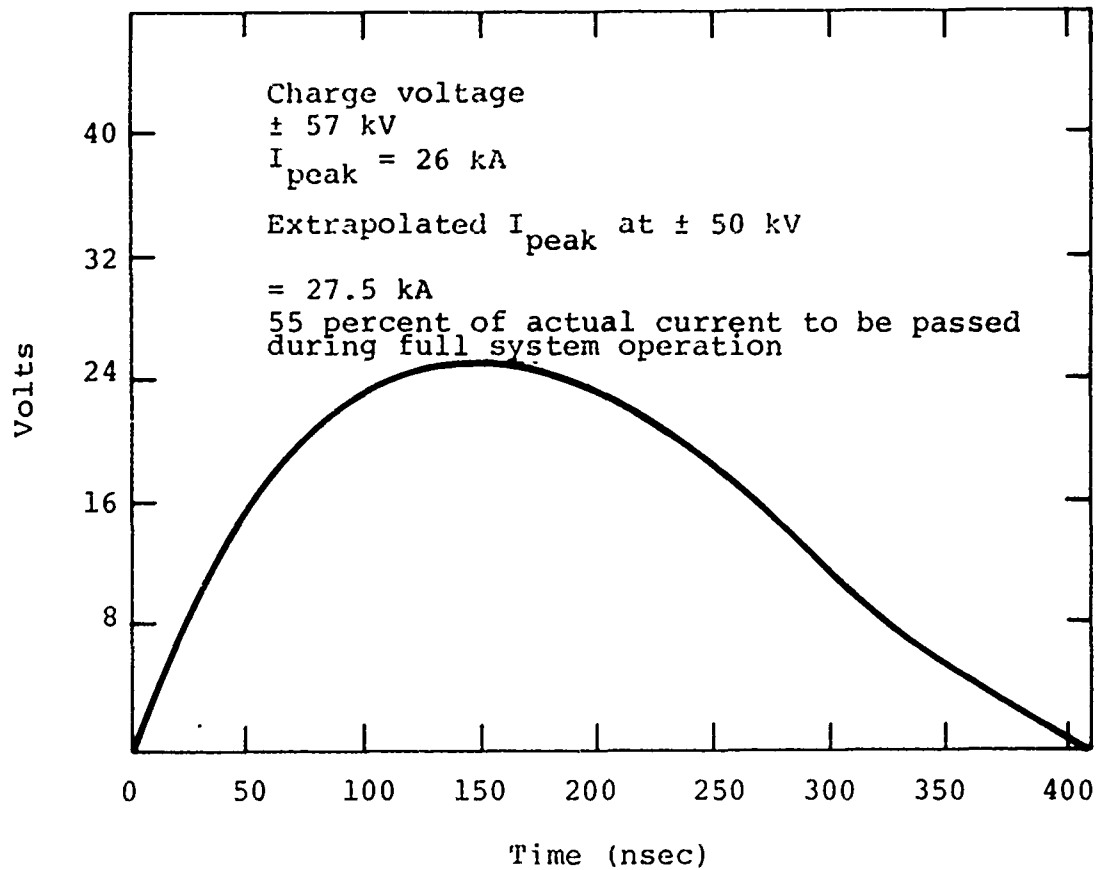


Figure 163 Rail switch test stand current waveform.

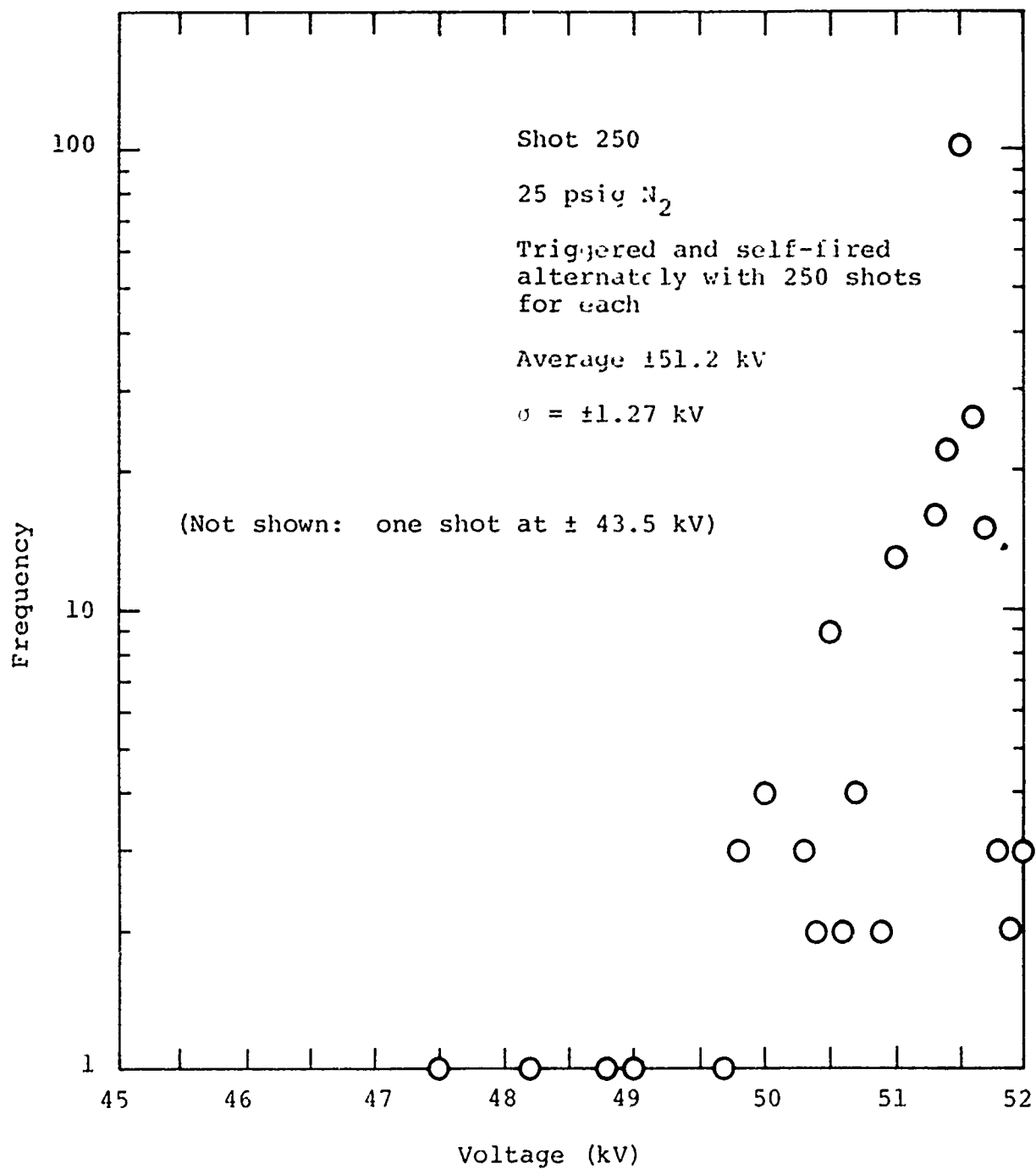


Figure 164 TEMPS prototype.

To develop an understanding concerning the midplane degradation effect upon switch reliability, a midplane taken from one of the consistent SIEGE switches was scraped with a file. The result was somewhat surprising since the switch remained as consistent as it had been except for the first 10 to 15 shots which apparently were needed to burn off the initial highly enhanced spots. The only indication that the midplane had been changed was that one shot out of approximately 100 shots fell at 40 percent of the mean self-break voltage at 25 psig  $N_2$ . This was the first recorded voltage at this low a percentage of the mean voltage. By removing the midplane entirely and using a one piece envelope, the consistency of the switch was regained.

#### C.5 CONCLUSIONS

There were strong indications that the TEMPS switches would perform in accordance with the specifications set forth for the full system at the beginning of this report. As a precautionary measure, it was suggested that each switch be pretested at peak voltage at 20 to 25 psig  $N_2$  to ensure consistent performance. If a single abnormal switch yielded a prefire rate above that, as it seems happened in the SIEGE Marxes, that could be tolerated. As described earlier, only one out of six randomly sampled SIEGE gaps performed abnormally, with the remaining five as consistent as the TEMPS prototype. Several SIEGE switches exhibiting similar behavior may have accounted for the troublesome behavior of the full Marx.

The continued degrading of the rail switch midplane due to triggering undoubtedly existed but appeared to be slow. There was no appreciable evidence that the scatter worsened after

many shots during the triggering iteration. The position of the midplane knife edge and the electrode enhancement may be the underlying factor causing erratic behavior. The TEMPS switch midplane edge was placed at 82 percent of the existing mean field between the electrodes. The SIEGE switch geometry does not lend itself to be calculated easily, but it appears that the nearly uniform field in the locality of the sharpened midplane edge is close to 100 percent of the mean field between the electrodes. The greater relative enhancement of the rail switch can be confirmed by the fact that, for both the SIEGE and TEMPS switches having equivalent gap spacings, the TEMPS switch has a lower breakdown voltage. At 10 psig  $N_2$  it is lower by 14 percent.

Because of the nearly uniform SIEGE switch geometry, the maximum field strengths that essentially govern the breakdown voltage for the switch are nearly equal to the mean field strengths. The slightest enhancement of the midplane could raise field strengths beyond that which can be withstood at the given gas pressure, hence causing a prefire.

On the other hand, the greatest field strengths that determine the breakdown voltage for the TEMPS switch are located at the electrode surfaces where fields are 25 percent higher than the mean field between the electrodes. The midplane knife edge is in a field strength region that is approximately 65 percent of the maximum field strength existing in the switch.

Fields in the locality of the knife edge could be enhanced by a factor of 1.5, due to triggering degradation, before affecting to any great extent the breakdown voltage of the switch.

APPENDIX D

SWITCH ACCEPTANCE TESTING

## D.1 PURPOSE

This section describes the systematic procedure for the assembly and acceptance testing of each Marx switch that was installed into the Marx generator. Each switch was checked for proper dimensions upon assembly followed by a self-fire consistency evaluation.

Unless the switches met the rigid standards set forth, they were rejected. This process assured operation of the Marx within the system reliability specification.

## D.2 APPROACH

Fairly rigid standards must be met by a single Marx switch if the entire system (which uses 70 switches) is to function reliably. Appendix C discusses the theoretical extrapolated self-fire probability of a single switch if the full system is to have a less than 1 percent self-fire occurrence. This means that no more than 2 shots out of 10,000 shots could self-fire for any one given switch. In other words, if a switch were pressurized and charged until it self-broke for 10,000 times, only 2 shots would be allowed to fall equal to or less than the percentage of the mean self-break voltage at this pressure, the pressure to which one intended to dc charge the full system. Normally, a system is set up so that one charges to only 80 percent of the mean self-break voltage for any given pressure setting. If this were the case, any shot occurring below 80 percent of the mean self-break voltage of the switch would be considered to have been a potential self-fire of the full system.

The later discussion serves as the basis for the consistency evaluation of each switch.

Each switch will be individually tested by charging and allowing to self-break while the voltage of each charge cycle is recorded by means of a chart recorder. At least 200 shots will be taken at a level of 80 to 100 kV across the switch at 20 to 25 psig  $N_2$  since the higher switch pressures produce the worst self-break voltage scatter. Consistency will be evaluated only after the switch appears to have broken in. Normally break-in takes 50 to 100 shots, after which no apparent deviation from the mean self-break is observed. Complete break-in and consistency require that no shots in 100 or more consecutive shots fall below 83 percent of the mean self-break voltage at a fixed pressure between 20 and 25 psig  $N_2$ .

An absolute mean self-break voltage comparison must also be made to determine if all switches come within 5 percent of one another for a given switch pressure.

### D.3 DESCRIPTION OF EXPERIMENT

Immediately upon manufacturing, each electrode, midplane, and switch body will be identified by a standard coding. Each component will be logged and a brief history will be kept of each electrode and midplane. In addition, all assembled switches will be identified and logged by the switch body identification number. All references will be made to such numbers. Sample log sheets are shown in Figures 165 through 167.

After each switch is found dimensionally acceptable, it will be installed into the test stand shown in Figure 168. The

MIDPLANE

NO. \_\_\_\_\_



Identification No. \_\_\_\_\_

BOW \_\_\_\_\_

HEIGHT A \_\_\_\_\_

Date of Manufacture \_\_\_\_\_

B \_\_\_\_\_

STATUS:

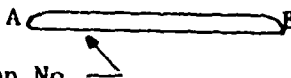
MAINTENANCE RECORD:

Figure 165 Sample log sheet--midplane.



ELECTRODE

NO. \_\_\_\_\_

Identification No. 

DIAMETER A \_\_\_\_\_  
\_\_\_\_\_

DIAMETER B \_\_\_\_\_  
\_\_\_\_\_

DATE OF MANUFACTURE \_\_\_\_\_

STATUS:

MAINTENANCE RECORD:

Figure 166 Sample log sheet--electrode.

SWITCH

NO. \_\_\_\_\_

BODY BORE: IDENTIFICATION END: \_\_\_\_\_ (GAP)  
\_\_\_\_\_OTHER END: \_\_\_\_\_ (GAP)  
\_\_\_\_\_

ELECTRODE NO'S. \_\_\_\_\_ GAP 1 \_\_\_\_\_

\_\_\_\_\_ 0 \_\_\_\_\_

MIDPLANE NO. \_\_\_\_\_ ALIGNMENT \_\_\_\_\_

\* Acceptance Test Data: DATE \_\_\_\_\_

Chart record number \_\_\_\_\_

Number of shots to break in \_\_\_\_\_

Mean self break voltage \_\_\_\_\_

At standard pressure \_\_\_\_\_ N<sub>2</sub>

Consistency factor \_\_\_\_\_

STATUS:

MAINTENANCE RECORD:

Figure 167 Sample log sheet--switch.

\* New sheet to be filled out if switch is reassembled or retested.



Figure 168 Marx switch test bed.

test stand is essentially a 0.2- $\mu$ F capacitor discharge circuit equipped with a 2-ohm series resistance and having approximately 100 nH of stray series inductance. A typical discharge waveform is shown in Figure 169. Peak currents produced at a 90 kV charge approach 37 kA.

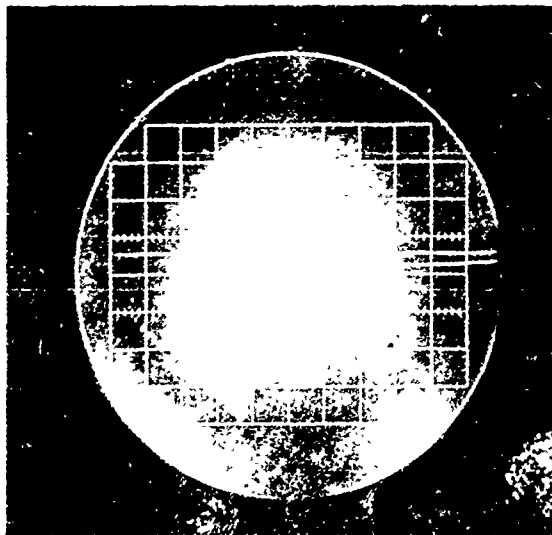
This value is felt to be close enough to the actual current that will be seen by each switch during actual operation and therefore constitutes a fair test of operational consistency while providing sufficient current for switch break-in.

Statistically, switch self-break voltages have a greater scatter at higher gas pressures. Twenty psig nitrogen has been set as the standard pressure for switch break-in and consistency testing. At this level, a self-break voltage of 92 kV  $\pm$ 2 per cent can be expected.

With a switch oriented in a given position in the test stand, approximately 50 shots are taken in one polarity while an additional 50 shots or so are taken in the reverse polarity as applied to the electrodes. The polarity may be changed after the first 50 shots even though the switch behavior still remain erratic. Quite often only one electrode breaks in by using a single polarity while the other electrode will only break in by reversing the electrode polarity.

If a break-in period of longer than 150 shots is observed, the switch should be rejected. Additional etching and bead blasting of the electrodes may be required.

Each charge cycle is monitored by a strip chart recorder. One charge cycle consists of charging the capacitor in approximately 15 to 20 seconds until the switch self-breaks. Immediately following this occurrence the capacitor is again charged and the process repeated until termination of the test.



100 nsec/division

1 V/division x

5/1 attenuation

Figure 169 Marx switch current derived from i-dot monitor and integrated (10  $\mu$ sec).

#### D.4 EXPERIMENT RESULTS

One hundred to one hundred fifty shots will be required for complete break-in of each switch. An additional hundred shots will determine the switches' relative consistency.

During the 100 or more consistency test shots, no self-break voltage may occur below 83 percent of the mean value which must be  $\pm 41.5$  kV  $\pm 2$  percent for each switch at 20 psig  $N_2$ . If a shot should occur below 83 percent of the mean, this may indicate an insufficient break-in period. The 100 shot series then should resume at this low shot with the number of break-in shots counted from the beginning of the test to the last recorded shot below 83 percent. If this condition occurs more than once, the switch must be rejected. Normally only 3 to 5 percent of the self-breaks will fall below 90 percent of the mean following sufficient break-in.

Any switch that does not meet the above standards must be rejected and inspected for obvious defects that would require reassembly.

#### D.5 CONCLUSIONS

The switches are expected to remain in service for at least 5000 shots and therefore should require no maintenance until that time. The 5000 shot figure is based upon past operation of similar switches operating at full voltage and current. Over the full spectrum of voltages during actual operation, a somewhat longer maintenance period may be sufficient.

Maintenance procedures will involve disassembly of each switch and cleaning and inspection of the body and bore. Electrodes and midplanes will be bead blasted and acid etched and each switch reassembled and the switch acceptance procedure repeated.

APPENDIX E

SOLID RESISTOR DEVELOPMENT



## E.1 INTRODUCTION

This report details the methods and results of a resistor test program. The resistors were tested for functional stability during the application of a series of high voltage pulses. The purpose of the test was to determine the suitability of these particular resistors and the encapsulating method for service within the Vertical Dipole RES project. The results of this test were quite favorable with respect to the anticipated usage.

## E.2 SCOPE OF TEST

The resistors tested were Dale NS-10, 10 Watts, low inductance, wire wound, with and without the standard manufacturer's overcoating. They were to be pulsed at increasing voltages until the pulse voltage was found at which a service life of at least 1000 pulses could reasonably be expected. The upper limit of voltage was determined beforehand to be  $10^5$  volts and the lower limit was likewise determined to be about  $2 \times 10^4$  volts.

A secondary objective was to determine a suitable scheme for encapsulating the resistors. Encapsulation was required to prevent end-to-end flashover, provide mechanical support for the resistors, and to protect the resistors from surface damage and weather effects.

E.2.1 Test Methods. Initially the test setup was as given in Figure 170a. This was used to test the 50-ohm and 180-ohm resistors through 60 kV. The poor internal connections of the ceramic capacitors (Sprague 2.7 nF, 40 kV) gave an exceptionally noisy leading edge to the pulses obtained. Availability dictated their use. The internal arcing reduced the energy deposition in the resistors but probably by not more than 2 percent to 5 percent.

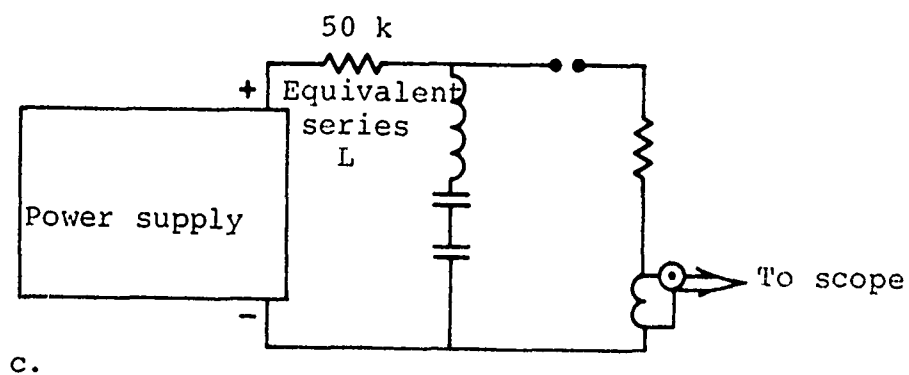
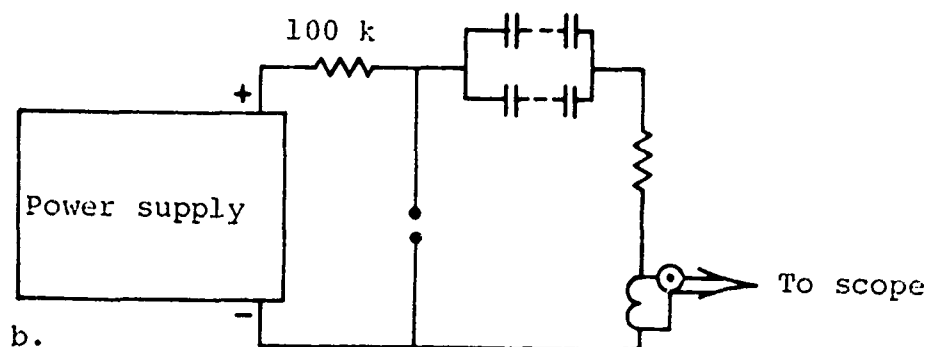
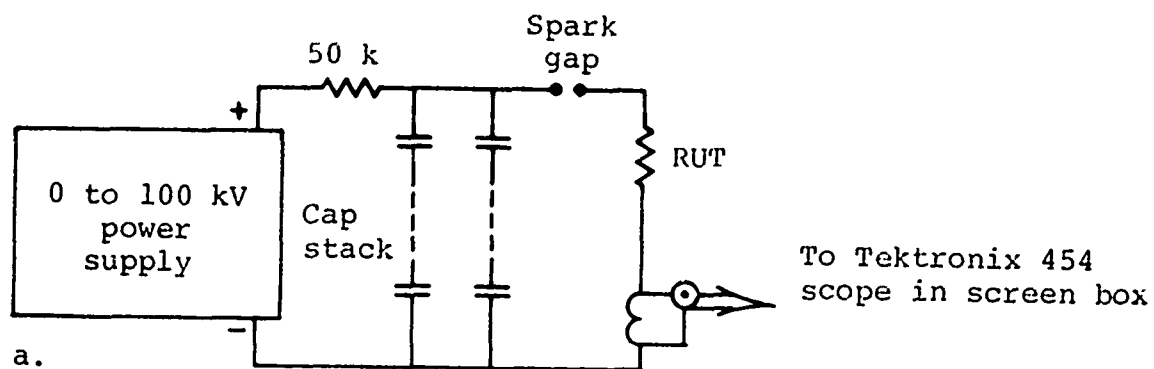


Figure 170 Test setups.

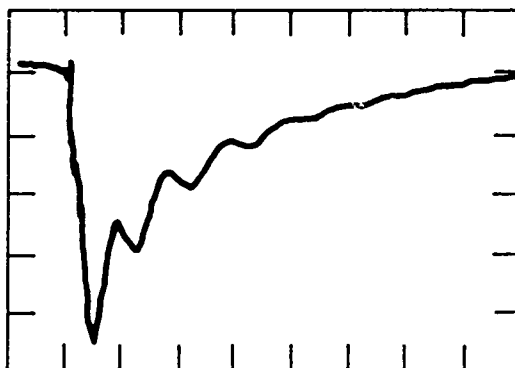
The current probe's sensitivity, when used with a 50-ohm system, was 200 A/V output. The equivalent capacitance used with the 180-ohm resistors was 2.7 nF and for the 50-ohm resistors 5.4 nF was used.

For the 80 and 199 kV pulses Figure 170b illustrates the test setup. This was done mostly for mechanical reasons to make it possible to enclose the gap and capacitor stack with a gas bag to reduce corona problems.

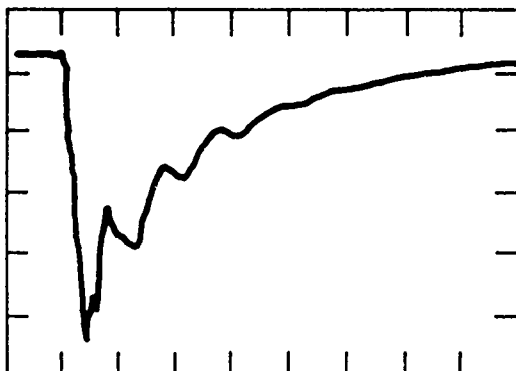
Testing the 5-ohm resistors was confined to the "uncoated" variety and was done with a different setup. Figure 170c illustrates that method. The equivalent capacitance used was 260 nF with all 5 resistors tested at once. When the sample lot was reduced to 3 resistors, a second capacitor was added, reducing the equivalent value to 130 nF. In both cases LC ringing dominated the produced waveform. Circuit inductance is estimated to be about 0.5  $\mu$ H based on mechanical dimensions of the current loop.

The resistors were to be pulsed 25 times at each 20-kV interval between 20 kV and 100 kV. The resistors were then to be pulsed 1000 times at both 80 kV and 100 kV. There were some modifications to this scheme, determined largely by resistor performance to any given point in the test.

The pulse voltage was taken from the dc charging voltage at the time of spark gap breakdown. That this was a suitable method was verified by monitoring the pulse current with a probe and scope and calculating the voltage given the value of resistance. The two voltage values were quite consistent; so the simpler method was used for general monitoring of the pulse voltage during the test runs. Two typical pulse current waveforms are given in Figure 171.



Resistor #5  
 40 kV pulse test  
 (nominal); calculated  
 voltage 46 kV  
 Horizontal 100 nsec/division  
 Vertical 1 volt/division



Resistor #3  
 20 kV pulse test  
 (nominal); calculated  
 voltage 23 kV  
 Horizontal 100 nsec/division  
 Vertical 0.5 volt/division

Figure 171 Typical pulse current waveforms.

## OUTLINE OF ACTUAL TESTS PERFORMED

<u>Resistor Number</u>	<u>Nominal Value (ohms)</u>	
1 → 5	50	Uncoated: No observable change for 25 pulses at each voltage through 100 kV. All pulsed an additional 1000 pulses at 80 kV with no observed changes. R#1 pulsed 296 times at 100 kV, produced discoloration of windings and some visual arcing. No measured changes in electrical values.
6 → 10	5	Uncoated: Pulsed 5 times at 100 kV in setup (Figure 170b) no change after 2 pulses; all permanently damaged after 5 pulses.
11 → 15	180	Uncoated: All unchanged after 25 pulses at each voltage to 100 kV. Pulsed additional 1000 pulses at 80 kV and 100 kV. No changes except #12, which had visual arcing after pulse 455 at 100 kV. No change in electrical value noted.
16 → 20	180	Coated: Ok after 25 pulses at 80 and 100 kV. No. 16 failed after pulse 625 at 80 kV. No. 17 after pulse 800, No. 18 after pulse 942. No. 19 was found to have one open winding after 1000 pulses, no arcing was seen. No. 20 was ok after 1000 pulses at 80 kV but opened on pulse 347 at 100 kV.
21 → 25	50	Coated: Pulsed 25 pulses at each voltage to 100 kV; no changes noted.
26 → 30	5	Coated: Not numbered or tested.
31 → 35	5	Uncoated: Started at 26 kV (lowest voltage available); 25 pulses, no change noted. Pulsed 25 times at 40 kV; no change. Pulsed additional 250 times at 40 kV. Slight decrease in resistance but measured warm. Pulsed 25 times at 60 kV. No. 35 had visual arcs and an open after pulse 18. Remaining 4 resistors were then pulsed at 30 kV until end of test. No. 35 opened after 846 pulses; test of remaining 3 resistors was terminated at 1286 pulses. Two resistors arcing but no change was found in resistance or inductance.

E.2.2 Failure Mode Observations. Particularly for the higher value resistors, a combination of joule heating and mechanical impulse appeared to cause the manufacturer's supplied coating material to allow electrical breakdown between adjacent turns of the resistance winding. Typical appearance of this fault was fine irregular cracks in the coating through which one could, occasionally, see the inner core. Additionally, there appeared to be a delamination of the Epoxylite encapsulant and the manufacturer's coating with the small voids presumably filled with gaseous decomposition products.

All values showed a second failure mechanism that was most obvious in the case of the 5-ohm resistors. The resistance element where it joined the end-cap would begin to tear radially outward from the resistor body starting from the inside, or acute angle, and going towards the obtuse angle made by the wire or ribbon as it lapped up on the end-cap. Arcing was observed across the tear if it was more than about 15 percent to 20 percent of the width of the wire. Once arcing was visible, the winding usually opened up at that spot within a few pulses. Then when the winding was open, or perhaps on the penultimate pulse before this, rapidly enlarging tensile failure cracks would propagate outward through the encapsulant.

E.2.3 Encapsulating Procedure. These resistors were potted in Epoxylite 2156 resin. This resin was selected for its good (and stable) electrical properties, low viscosity when uncured, good adhesion and low shrinkage, and excellent moisture and chemical resistance when cured. Additionally, it is optically clear in moderate thicknesses, serviceable to 300°F, and a semi-rigid compound.

The resistors were washed in a clean technical grade Acetone, warmed to at least 150°F, and vacuum cycled to remove traces of solvent and water. Care was taken in washing and all subsequent handling to avoid touching the body of the resistors with bare hands.

The resistors were then inserted, with rubber stoppers for mold closures, into 5/8 inch i.d. x 1/8 inch wall thickness Tygon tubing. This tubing was also washed and dried in the same manner as the resistors. The molds were then half filled with properly mixed and de-gassed encapsulating resin. The partially filled mold was heated to about 150°F for a few minutes and vacuum cycled for a few more minutes. The molds were then filled and the entire heating and vacuum cycle process repeated.

The resistors then were cured by heating to 145°F for at least 16 hours and 200°F for at least an additional 20 hours. The tubing was slit open to remove the encapsulated resistor.

E.2.4 Results. The testing of several resistors to determine suitability for service in the Vertical Dipole RES has been completed. The results are briefly as follows:

a. There are two principal failure modes:

- I. Tearing of the resistance ribbon where it joins the end-cap of the resistor
- II. Outgassing and mechanical decomposition of the manufacturers supplied coating allowing interturn arcing

In either case once arcing has started, the Epoxylite encapsulant begins to receive a sufficiently large mechanical impulse that it tears and shatters and eventually develops carbon tracks.

- b. The preferred resistor is of "uncoated" construction, i.e., without the manufacturer's ordinarily supplied outer coating.
- c. The 50-ohm and 180-ohm resistors appear capable of withstanding at least a few thousand pulses at 80 kV peak pulse amplitude with 150 to 250 nsec fall times. The 5-ohm resistors, however, will not survive reliably for more than a few tens, or at best hundreds, of pulses at anything above 40 kV.
- d. Testing the 5-ohm resistors required a different equipment setup and this may have something to do with the apparently different performance of these resistors. The waveform was a 3-cycle exponentially damped sine wave of about 6  $\mu$ sec period. Due to the large inductance and consequent generator impedance the energy deposited in the resistors was about 1/3 that calculated on an ideal capacitor discharging onto an ideal resistor.

### E.3 RECOMMENDATIONS

Subsequent to the initiation of the testing it was discovered that the minimum value of resistance was to be 10 ohms. It was felt that there should be no difficulty in using this value of resistor in the antenna design.

It was recommended that the uncoated variety of resistor be used, at least for all values of resistance less than 200 ohms. These resistors should be potted in strings of ten resistors per section as a single assembly. The higher values of resistance will require special care and attention in handling to avoid damaging the fine resistance wire windings. The overcoated variety of resistor (i.e., manufacturer's standard product) is recommended for resistance values above 200 ohms because of the difficulty in handling. The peak current values will also be much less so that the effect of the coating upon service life will be less important.



APPENDIX F  
SOLID-DIELECTRIC GAS-GRADED PEAKING CAPACITOR

## F.1 PURPOSE

The purpose of this experiment was to investigate the feasibility of using a solid-dielectric peaking capacitor in TEMPS.

To best evaluate the performance of such a capacitor, one section of the anticipated peaking capacitor was put under test. The TEMPS peaking capacitor design calls for a sectional construction where each section is approximately 4 nF in value and is subjected to 100 kV. The design of the test geometry was in keeping with these specifications and a self-breaking point-point switch was installed so as to simulate the actual peaking circuit type of operation.

## F.2 APPARATUS DESCRIPTION

F.2.1 Electrical Circuit. Figure 172 shows the test circuit used. The 0.2- $\mu$ F capacitor was dc charged to a given voltage and switch S1 was closed and the voltage applied to the test geometry. Switch S2 was adjusted to break at the proper voltage which had been anticipated to be the extrapolated peak of the exponentially decaying tail of the output pulse.

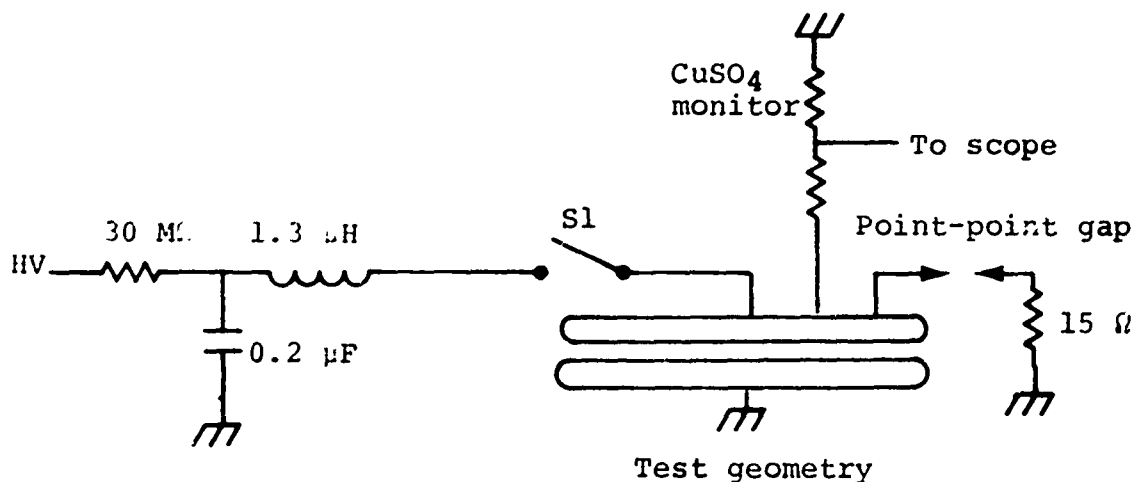


Figure 172 Test circuit.

The 15-ohm load resistance provided the proper decay time and the voltage was monitored by the  $\text{CuSO}_4$  voltage divider.

**F.2.2 Capacitor Section.** The construction of the solid peaking capacitor section under test consisted of two large 36-inch-diameter parallel plates shown in Figure 173. At the center of each large plate was a smaller aluminum electrode which was separated from the other electrodes by means of the given dielectric material. The predominant capacitance of the test section was governed by the spacing and area of the smaller aluminum electrodes.

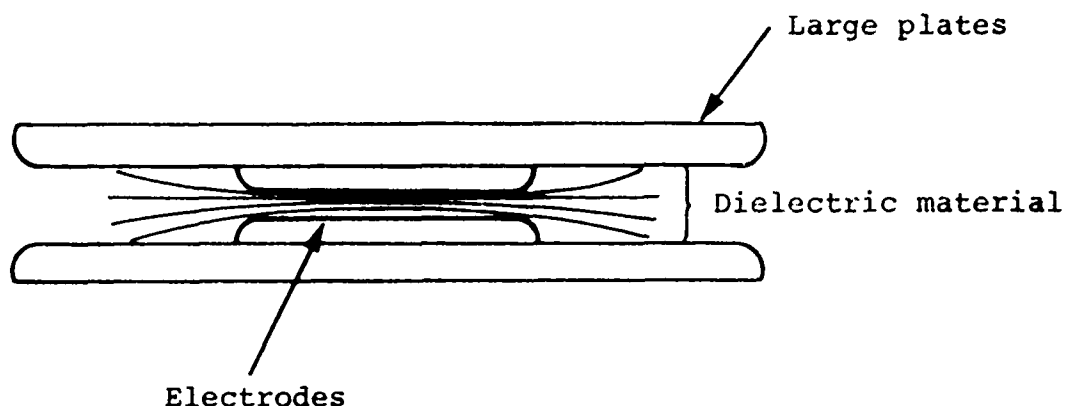


Figure 173 Parallel plate capacitor section.

The entire test section was placed within a wooden enclosure which was filled with atmospheric pressure Freon-12 gas. It was estimated to be an approximately 70 percent Freon/30 percent air mixture, possessing twice the voltage holding capability of air alone.

**F.2.3 Point-Point Gap Output Switch.** The point-point gap had sharpened 1/4-inch-diameter electrodes spaced 1 cm apart. Nitrogen gas was used and gas pressure was varied over a range of 0 to 40 psig to obtain the best possible output waveform.

**F.2.4 Voltage Source.** The voltage source was a 125 kV, 0.2  $\mu$ F capacitor submerged in an oil tank for insulation. A mechanical drop ball type switch dumped the dc charged capacitor into the test geometry.

**F.2.5 Monitoring.** The voltage applied to the capacitor test section was monitored by a 700-ohm  $\text{CuSO}_4$  voltage divider with the attenuated pulse displayed on an oscilloscope.

### F.3 MEASUREMENTS

F.3.1 Inductance. The test geometry stray inductance was measured by shorting the parallel plates with a low inductance short and allowing the circuit to ring. In this way, the overall circuit inductance was found to be  $1.3 \times 10^{-6}$  H.

F.3.2 Capacitance. By removing the 15 ohm load from the test geometry and allowing the circuit to ring out, the capacitance of each test geometry was determined. This value ranged from 2 nF to 4 nF depending upon the thickness of solid dielectric material being tested.

F.3.3 Pulse Charge Time. The pulse charge time of the test capacitor geometry was on the order of 200 nsec (for output switch closure at  $t_p \approx \pi/2\omega$ ).

### F.4 PROCEDURE

Each test iteration consisted of varying the following parameters:

- a. Number of dielectric sheets between the electrodes
- b. Thickness of each sheet
- c. Types of dielectric material used
- d. Use of paper and Mylar
- e. Diameter of the dielectric sheets
- f. Electrode edge contour

For each fixed configuration, the test capacitor was pulse charged with varying voltages until breakdown occurred. Approximately two to three shots were taken at each voltage.

The general configuration for each iteration is shown in Figure 174. The dielectric and paper sheets were cut into circles of about 20-inch diameter and stacked in such a way that their surfaces would be along the equipotential lines. In this manner the field lines are perpendicular to the sheets and lessen the chance of tracking around the edges.

The polyethylene spacers in Figure 174 were used to separate the sheets. This method proved to be best since it kept the sheets almost parallel without any buckling.

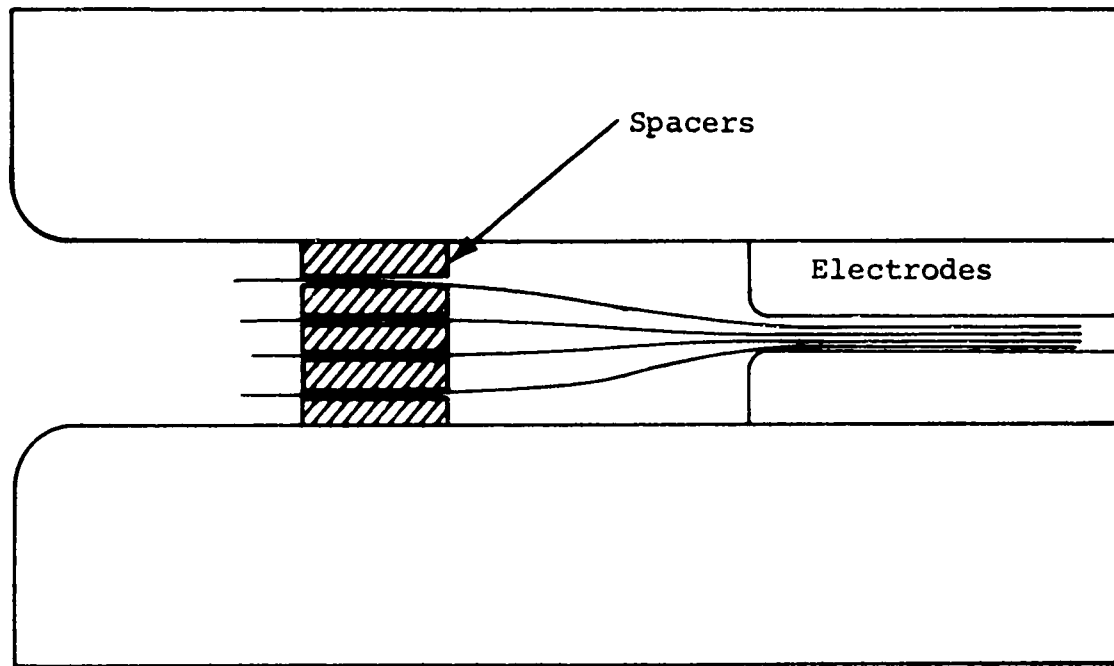
#### G.5 DATA INTERPRETATION

Table XX summarizes the results of the test iterations.

The recorded electrode gap spacing is the total thickness of dielectric sheets and paper (if used) for each iteration.

The capacitances cited are those which were found experimentally by the method previously discussed.

Peak voltage is that which was recorded by the voltage monitor and the peak field strengths are the peak voltages divided by the electrode gap spacing.



Spacer  
shape



Top view of spacer position

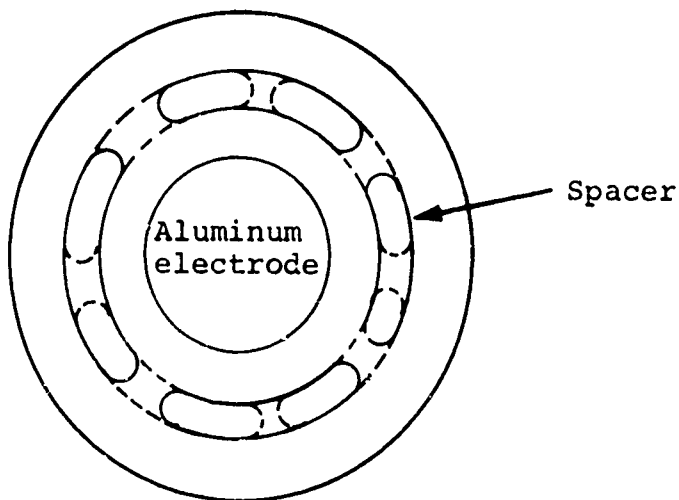


Figure 174 General test configuration for capacitor section.

TABLE XX  
TEST RESULTS

Iteration	Electrode Diameter (inches)	Electrode Edge Radius	Electrode Spacing (inches)	Capacitance (nF)	Peak Voltage (kV)	Peak Fields (MV/cm)	Comments
1	14-1/2	large	0.020	3.82	81.5-83	1.60-1.63	Four sheets 0.005-inch Mylar, 20-inch diameter. Broke down on pulse rise at electrode edge.
2	14-1/2	large	0.021	3.55	88.5	1.65	16 sheets 1.30 mil polyethylene, 20-inch diameter, stacked in 4 groups. Broke down on pulse rise at electrode radius.
3	14-1/2	tapered with tin foil	0.020	-	95.5	1.7-1.9	Four sheets 0.005-inch Mylar, 20-inch diameter, tracked around Mylar. Arc closed 1.5 $\mu$ sec from peak.
4	14-1/2	tapered with tin foil	0.020	-	115	2.0	Four sheets, 0.005-inch Mylar, 24-inch diameter, tracked around Mylar. Arc closed after 1.5 $\mu$ sec from peak.
5	12.80	0.020	0.020	3.7	98	1.93	Four sheets, 0.005-inch Mylar, 20-inch diameter. Arc punctured Mylar at electrode edge on rising pulse.
6	12.80	0.020	0.040	1.98	114-116	1.13	Four sheets Mylar, 4 sheets paper, all 0.005 inch in alternate positions. Twenty inch diameter, breakdown occurred across large plates, not electrode plates.
7	12.80	0.020	0.040	2.20	100	0.98	Eight sheets 0.005-inch Mylar, stacked in pairs, 20-inch diameter, tracked around sheets after 1.15 sec.
8	12.80	0.020	0.020	4.10	78	1.15	Two sheets 0.010-inch Mylar, 20-inch diameter, broke after 1.35 $\mu$ sec. Punctured Mylar at electrode edge.
9	12.80	0.020	0.040	2.12	110	1.08	Four sheets Mylar, 4 sheets paper, 0.005 inch each, stacked alternatively in groups of two. Twenty-inch diameter, breakdown occurred across large plates.



## F.6 DATA ANALYSIS AND RESULTS

The iteration parameters in Table XX are self explanatory except in the case of numbers 3 and 4. In these cases, 20 inch tin foil disks were draped over the electrode plates in an effort to relieve the fields more slowly than previously with the "large radius" electrode edge. The side view of the plate contour is shown in Figure 175.

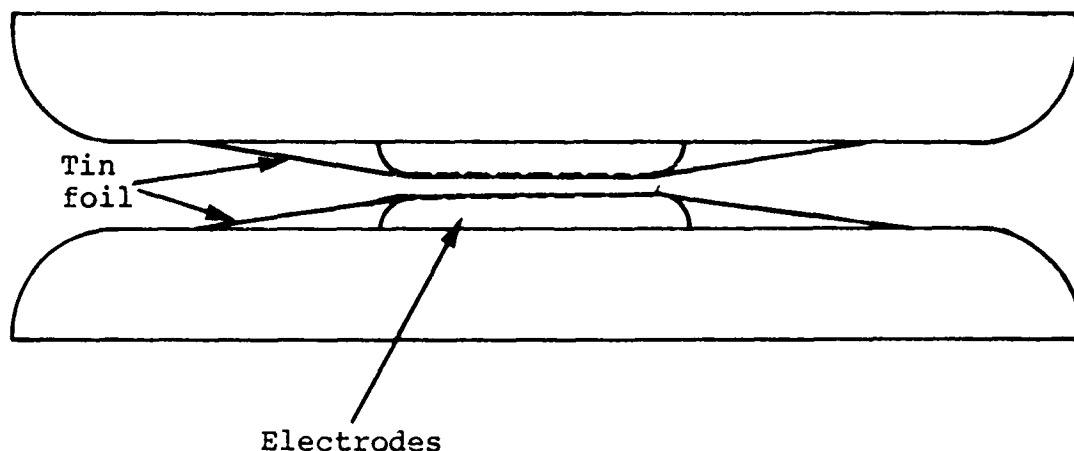


Figure 175 Tin foil contour.

In iterations 6 and 9, no breakdown occurred across the test capacitor; instead breakdown occurred across the large plates near the edges. Assuming a 70 percent Freon content within the enclosure, this gives a breakdown field strength of approximately twice that of air or about 90 kV/cm. For a rod-rod approximation, the 1/2 inch radius plate edges spaced 3/4 inch apart (surface to surface) give an enhancement factor of 1.4. Since breakdowns occurred at peak voltages of 120 kV, this equates to a peak field strength of between 80 to 90 kV/cm in agreement with the measured value.

In iterations 6 and 9, there was evidence of the paper failing since tiny pinhole arc punctures could be seen. Likewise small pinholes could be seen in the Mylar sheets that lay against the paper. Apparently arcs formed in the paper with enough energy to puncture the Mylar. However, in either of the two above cases, no breakdown was observed since the arcs continued no further than a single sheet of paper on a single layer of Mylar.

In all cases, breakdown occurred (tracking or direct puncture at field strength levels substantially below the "intrinsic" strength of the plastic dielectric material. Breakdowns, as expected, are due to our ionization and streamer development at the edges of the test electrodes with subsequent arc puncture or tracking of the dielectric material. Breakdown voltage was, to the first order, constant and independent of solid dielectric thickness or electrode edge radius.

As a recommendation for further experimental work, the thickness of solid dielectric material could possibly be reduced with associated increase of stress within the solid dielectric material, keeping the electrode separation in gas constant.

APPENDIX G  
SINGLE-MODULE PEAKING CAPACITOR TESTS

## G.1 PURPOSE

Single-module peaking capacitor prototypes are tested to expose and define problem areas in each of several tentative designs and to determine how to design the full-scale peaking capacitor in regard to such problem areas. Primary areas of concern are: dielectric breakdown within the high-stress regions between electrodes of a single module, breakdown at the electrode edges where the electric field must be graded to its Freon-plastic interface value, and surface tracking or envelope flashover at the Freon-plastic interface on the outside of each peaking capacitor stack.

Single module testing also includes collecting comparative data to facilitate evaluation of tradeoffs between alternative design parameters. Such data must be considered in deciding which dielectric medium to use in the final design and what type of edge grading is best for each alternative. These data will also help point out otherwise unforeseeable difficulties with respect to the assembly and maintenance of each prototype. Assessment of difficulties involved in de-gassing, de-ionizing, and sealing against leakage in the case of a liquid dielectric is one example. Another is determining problems of assembling multilayer film stacks under liquids.

Determining reliability is also an integral part of single module testing. Repetitive stressing of prototypes with voltage waveforms simulating those predicted for the ultimate design will enable statistical inference of reliability to be made. Such testing will be made a part of all phases of peaking-capacitor development.

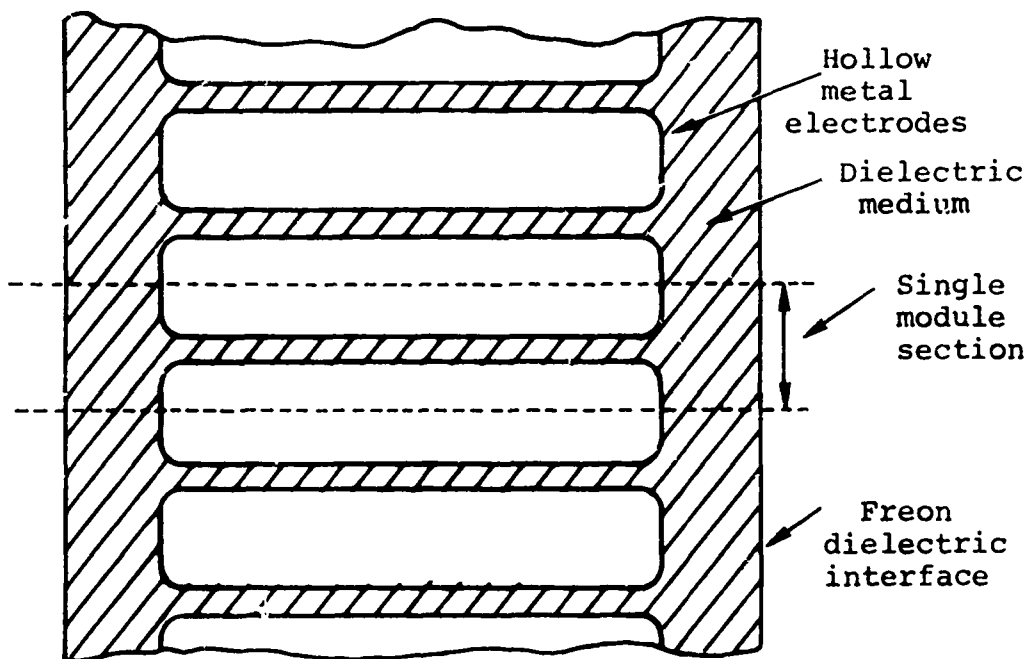
## G.2 TECHNICAL APPROACH

A single module is defined as shown in Figure 176. No prototype design was assumed in Figure 176. However, the basic peaking capacitor design concept is shown of stacking 35 single modules in series to yield a single, 3.5-MV unit, eight of which will be placed in parallel to comprise the peaking capacitor for each half-generator.

Prior to the launching of the high-frequency pulse from the bicone, the dotted lines of Figure 176 will lie approximately on an equipotential plane of the peaking capacitor. This condition suggests using the test configuration of Figure 177, in which half-thickness metal electrodes are attached to conducting plates designed to produce a uniform electric field parallel to the module axis. The magnitude of such a field should approximate that which will appear across the Freon-dielectric interface during charge of the peaking capacitor, thus enabling the interface to be tested for flashover in the Freon environment at the same time reliability is being determined within the high-stress region of the center.

The basic testing approach will be to develop single module prototypes and stress them with a pulsed waveform simulating the one to which the final peaking capacitor will be subjected. A basic description of probable prototype iterations may be found in Reference 1; actual prototype descriptions will be presented in this report along with associated test data.

The limitations of single module testing preclude investigating the effects of side fields, perturbation of equipotentials near the end of capacitor stacks, and the volume



NOTE:

Single module is defined as typical to that shown between dotted lines which bisect electrodes.

Figure 176 Single module of peaking capacitor.

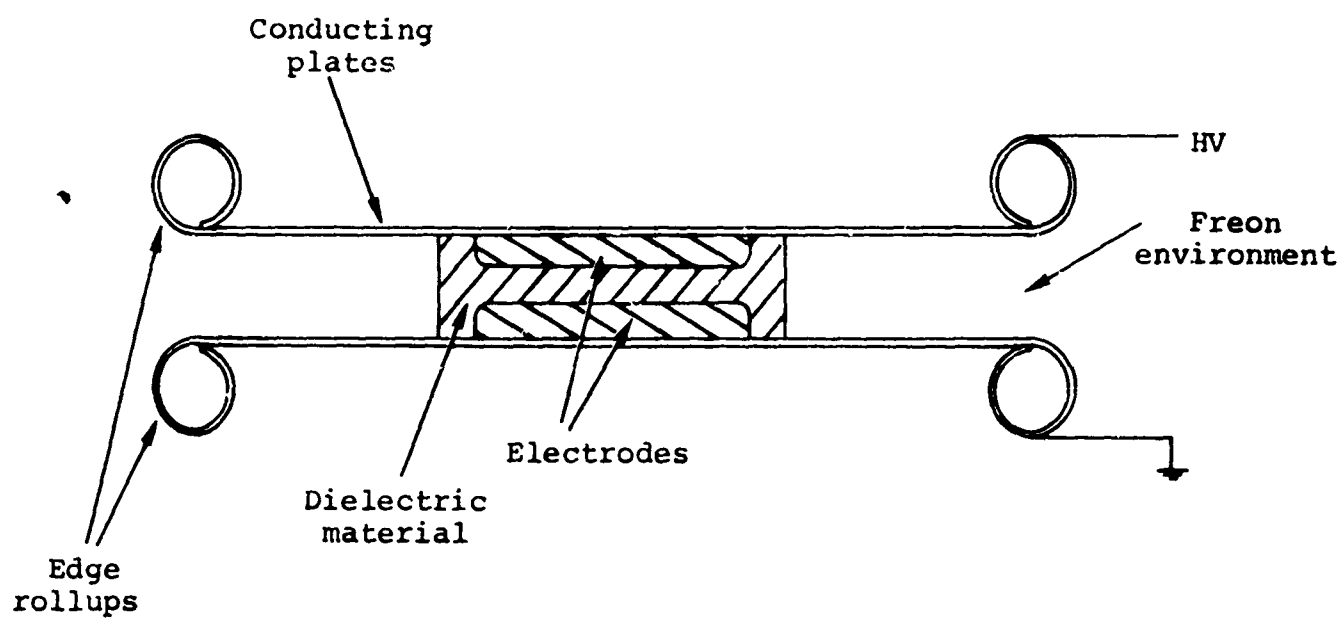


Figure 177 Basic test apparatus.

dependency of voltage breakdown in plastics. Side fields and end effects will be investigated in the ten-module and full-scale tests; so it is not necessary to consider them here. The volume dependency of solids, however, should be considered in the single module tests because of the way it compares to the dependency of Freon-plastic interface breakdown upon envelope length. As shown previously (Reference G-1), the mean breakdown strength of the entire assembly can be expected to decrease as the number of modules is increased. Such an effect is not expected with regards to envelope flashover. The mean breakdown strength for the Freon-plastic interface should be relatively insensitive to overall envelope length because, presumably, the breakdown mechanism of the interface is different from that which governs solids. If  $\bar{V}_E$  is the mean voltage that will induce interface flashover when placed across a single module and  $\bar{V}_B$  is the mean voltage required to break the main body of the dielectric, then the ratio  $\bar{V}_B/\bar{V}_E$  should be somewhat greater than unity for single module testing in order to account for its reduction as the number of modules is increased. Using a treatment similar to the one given in Reference G-1, it can be shown that the ratio should be around 2.2 for single module tests if one assumes it is equal to unity in the full generator case. As a result, the single module test configuration shown in Figure F-1 should not allow testing for the maximum breakdown strength of the main dielectric because interface flashover will dominate for any reasonable solid-dielectric prototype. Maximum breakdown strengths will be determined in subsequent testing phases.



## G.3 DESCRIPTION OF EXPERIMENT

The experimental apparatus is shown in Figures 178 and 179; the electrical circuit is shown in Figure 180. With properly chosen values for the circuit parameters of Figure 180, the waveform across the test module will simulate the one expected for TEMPS with respect to both voltage and waveshape. For the case of zero series losses in the charging circuit of Figure 180, the voltage across the peaking capacitor prior to switching takes the form

$$V_p(t) = V_o (1 - \cos \omega t) \quad (G-1)$$

where  $V_o$  is the initial charge voltage,  $\omega$  is the angular frequency of the circuit in radians per second, and the assumption  $C_c \gg C_p$  is made. This waveform is shown in Figure 181a where the values of  $t$  are those resulting from the expected value of  $\omega \approx 1.6 \times 10^7$  radians/sec for the TEMPS circuit.

In the limiting case where the charging capacitor  $C_c$  is replaced by a battery (Reference 7), if the circuit is switched into the load at

$$t_s = \frac{\pi}{2\omega} \quad (G-2)$$

and the relation

$$R_L = \frac{L_s}{C_p} \quad (G-3)$$

PIFR-372

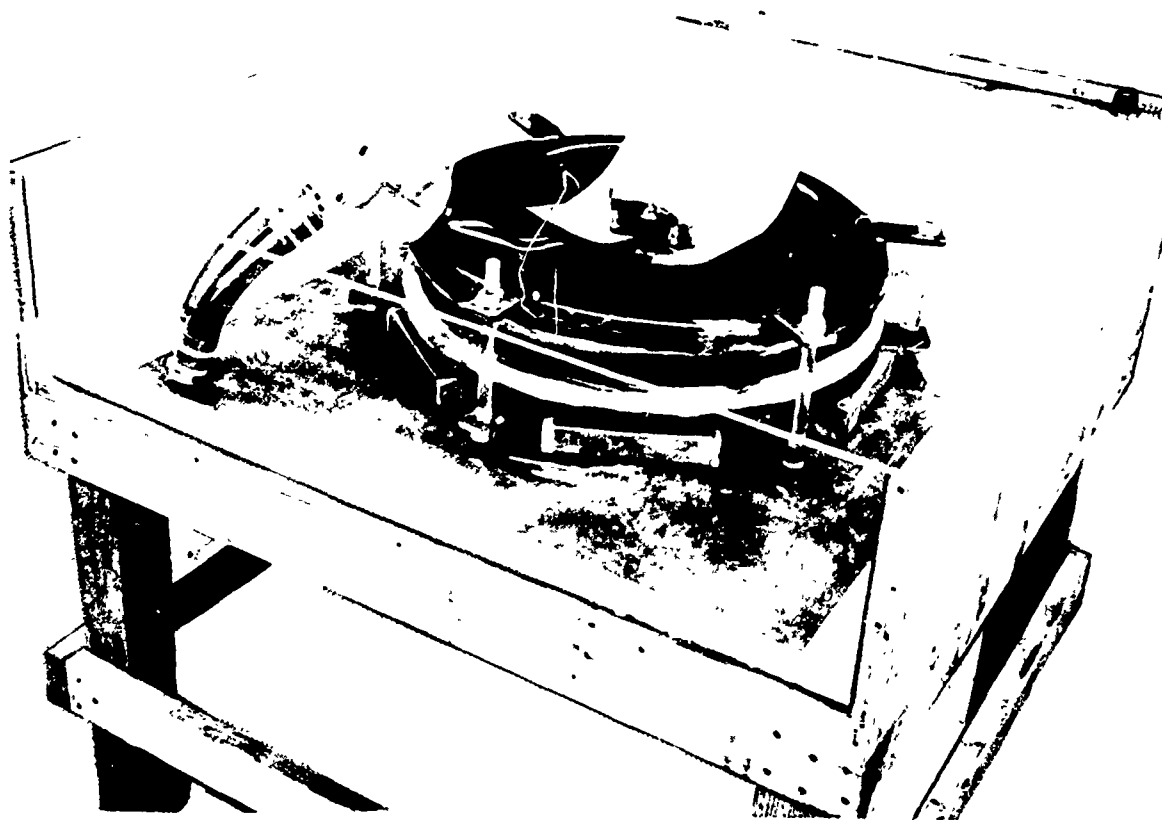


Figure 178 Test apparatus.

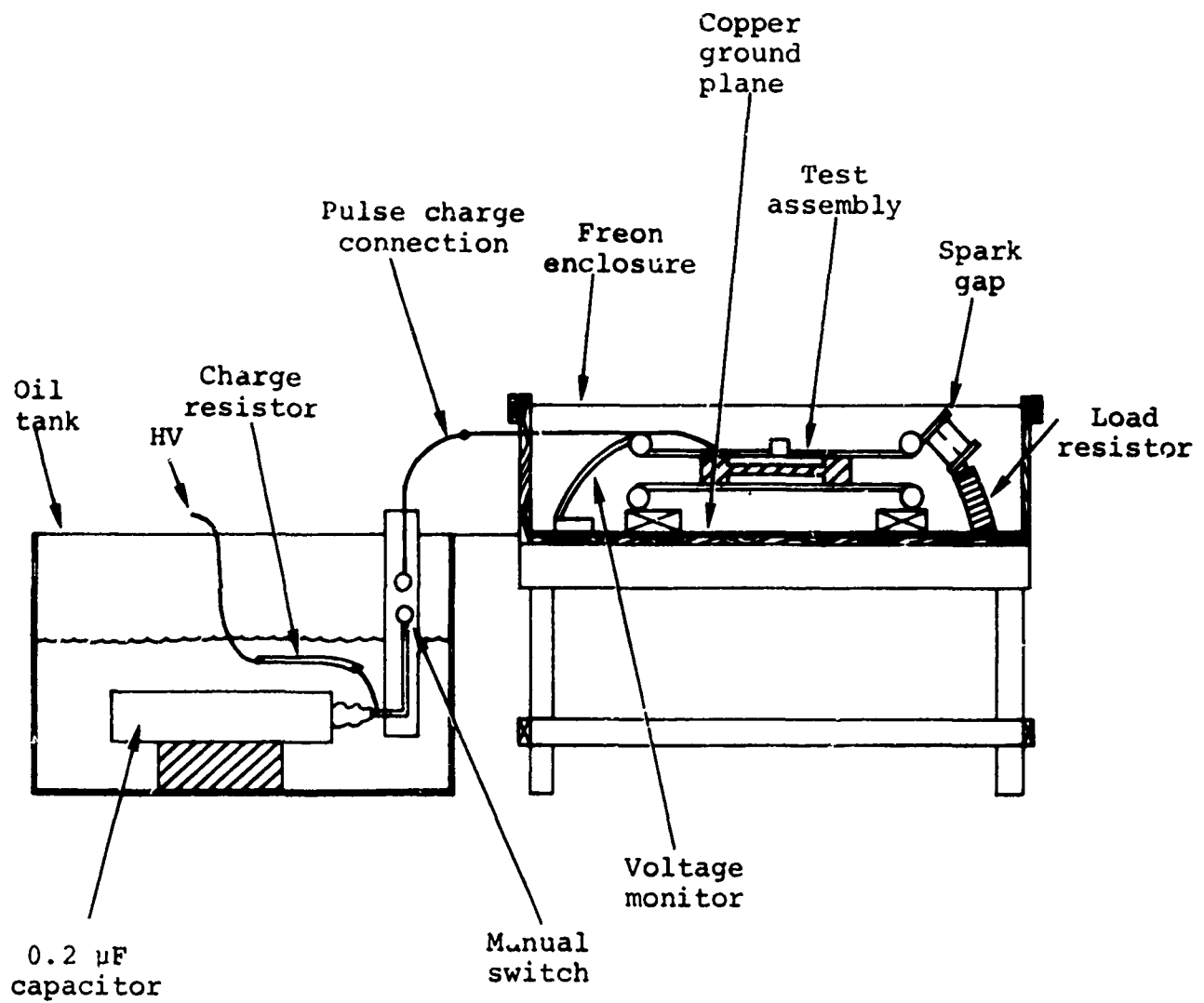
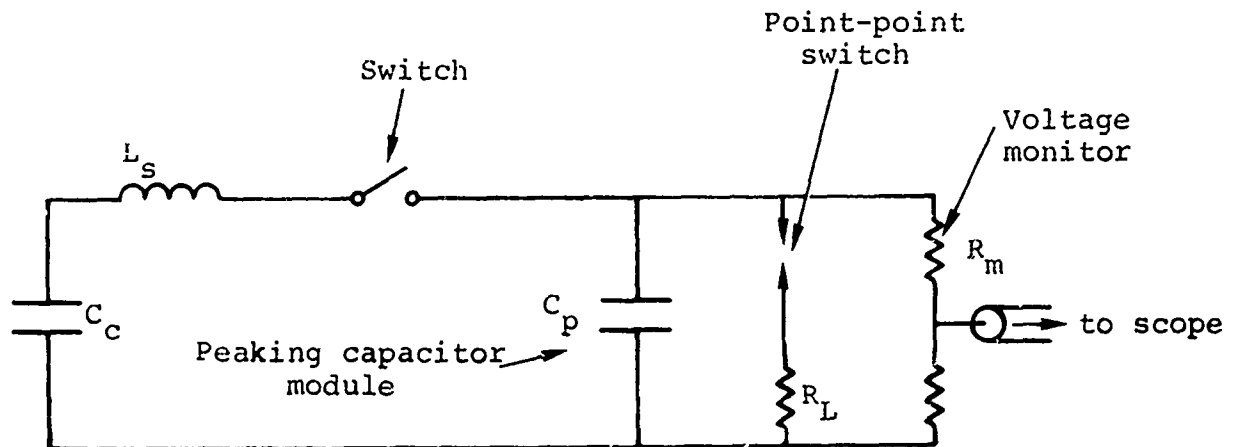


Figure 179 Basic testing fixture.



- $C_c$   $\equiv$  charging capacitance  $\gg C_p$   
 $C_p$  . peaking capacitor module capacitance  
 $L_s$  . stray inductance of circuit  
 $R_L$  . load resistance  
 $R_m$  . monitor resistance  $\gg R_L$

Figure 180 Test circuit.

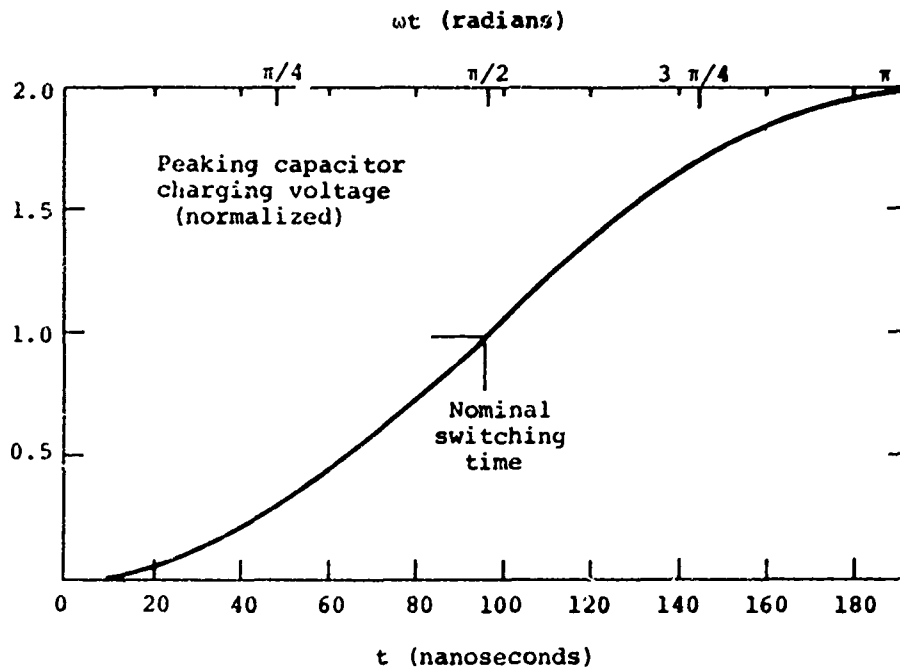


Figure 181a Idealized charging waveform when switch remains open.

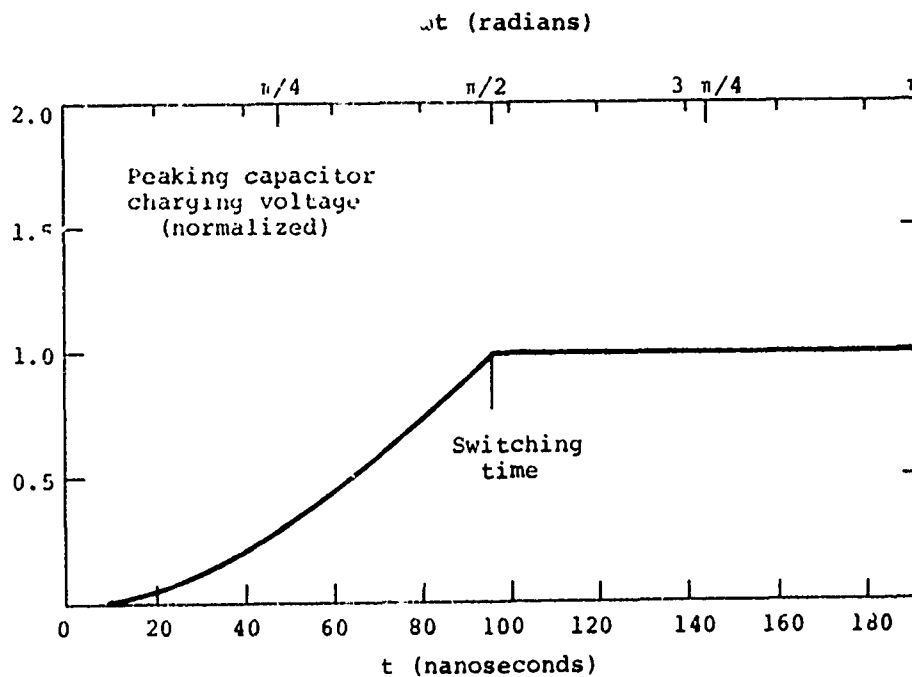


Figure 131b Idealized charging waveform when switch closes at  $t = \pi/2\omega$  (battery limit).

obtains, then the waveform of Figure 181b appears across the peaking capacitor. This can be expressed by

$$V_p(t) = V_o (1 - \cos \omega t); t < \frac{\pi}{2\omega} \quad (G-4)$$

$$V_p(t) = V_o; t > \frac{\pi}{2\omega} \quad (G-5)$$

In the real circuit for TEMPS and the test circuit shown in Figure 180 expression (F-5) assumes the approximate form of

$$V_p(t) = V_o e^{-\alpha t} \quad t > \frac{\pi}{2\omega} \quad (G-6)$$

where  $\alpha$  is the decay constant for the circuit. For the test circuit

$$1/\alpha \cong R_L C_L \quad (G-7)$$

For TEMPS  $1/\alpha$  may be on the order of 300 to 500 nsec.

The experimental procedure is to design a prototype single module, stress it to the maximum voltage allowed by the test apparatus, and, if it survives the maximum voltage test, subject it to repeated pulses of the maximum design voltage to determine reliability.

#### G.4 EXPERIMENTAL PARAMETERS AND HARDWARE

The apparatus of Figures 179 and 180 was constructed using a 0.2- $\mu$ F Aerovox type PX480D42 storage capacitor rated at 125 kV dc maximum with 80 percent reversal. A Universal Voltronics dc power supply with maximum output of 130 kV is used to supply high voltage.

Once the apparatus was constructed, circuit inductance was measured by switching the charged capacitor into a short circuit through the test apparatus and measuring the resulting frequency of oscillation. The measured value of  $L_s$  was approximately 1.5  $\mu\text{H}$ . Using Equation (G-3), the proper load resistance was determined to be 21 ohms. A  $\text{CuSO}_4$  resistor with this value was placed in series with a point-point spark gap which was chosen to obtain consistency in switching. The switch was provided with a pressurized nitrogen supply.

Fortuitously, the stray circuit inductance provided a value for  $\omega$  of around  $1.5 \times 10^7 \text{ rad-sec}^{-1}$  so that  $\pi/2\omega \cong 100 \text{ nsec}$  as in the TEMPS circuit. Thus, expression (G-4) is well simulated.

For the test circuit, the value of  $1/\alpha$  from Equation (G-7) is approximately 4.2  $\mu\text{sec}$ . The e-fold decay of the experimental pulse is therefore an order of magnitude greater than that expected for TEMPS. This should allow for somewhat of an over-test with respect to voltage holding capabilities.

A  $\text{CuSO}_4$  voltage monitor was placed across the test apparatus and connected to a shielded Tektronix 454 oscilloscope via RG-217 coaxial cable.

The conducting steel plates shown in Figures 177 and 178 are used to produce a uniform field area for the test modules. The plates are approximately 28 inches in diameter and have 2-inch rollups. The entire assembly is placed in the Freon box for testing.

## G.5 EXPERIMENTAL RESULTS

The prototypes tested to date are arranged in three basic categories: single sheet solid dielectric, multi-layer solid dielectric, and liquid dielectric. These represent three of the basic design alternatives listed in Reference G-1 and are described in detail in Sections G.6 through G.9.

## G.6 EXPERIMENTAL WAVEFORM

Prior to actual testing, the test circuit performance was verified. Prototype I, described below, was installed and its capacitance measured. Then a series of low voltage shots were fired in which charge voltage and switch gap pressure were varied to vary the switch point. The results are presented in Figure 182 and the time of switching is given in units of  $\beta$  where  $\beta$

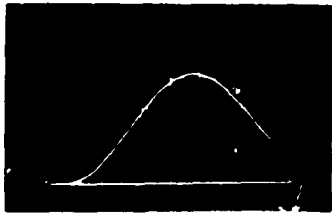
$$\beta = \frac{2 \omega t}{\pi} \quad (G-8)$$

was determined by combining Equations (F-1) and (F-8) to give

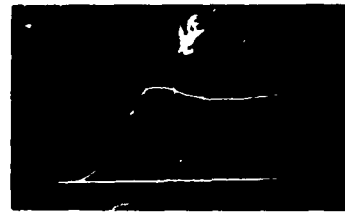
$$\beta = \frac{2}{\pi} \cos^{-1} (1 - V_s/V_o) \quad (G-9)$$

where  $V_s$  is the peak voltage measured at the switch point from oscilloscope traces and multiplied by a normalizing factor to compensate for losses; the charge voltage is  $V_o$ . As can be seen, late switching induces oscillations which are not present when switching near  $\beta = 1$  (where  $\omega t = \pi/2$ ). Figure 182a corresponds to the switch remaining open and compares to Figure 181a. Figure 182g is in good agreement with Figure 181b for switching at  $\beta = 1$ .

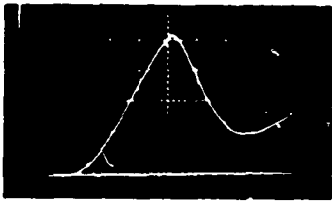




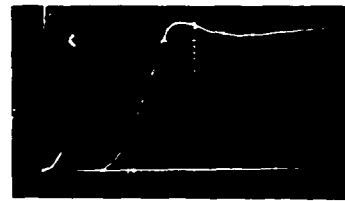
a) 5.2 kV/cm  
 $V_0 = 10 \text{ kV}$   $\beta \rightarrow \infty$



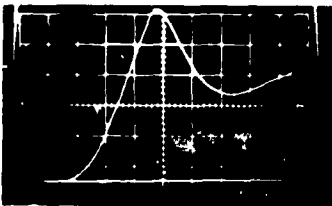
d) 13 kV/cm  
 $V_0 = 40 \text{ kV}$   $\beta = 1.05$



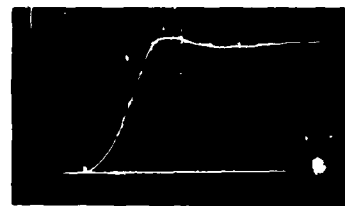
b) 7.4 kV/cm  
 $V_0 = 20 \text{ kV}$   $\beta = 1.67$



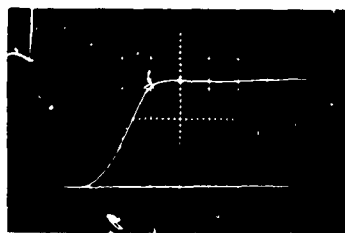
e) 13 kV/cm  
 $V_0 = 65 \text{ kV}$   $\beta = 1.04$



c) 7.4 kV/cm  
 $V_0 = 30 \text{ kV}$   $\beta = 1.34$



f) 13 kV/cm  
 $V_0 = 60 \text{ kV}$   $\beta = 1.03$



g) 13 kV/cm  
 $V_0 = 50 \text{ kV}$   $\beta = 1.00$

All sweep speeds are 50 nanoseconds/division. Switching times given in units of  $\beta = 2\omega t/\pi$   $V_0$  is charge voltage.

Figure 182 Experimental waveforms for various switching points.

It should be noted that the experimental circuit has a larger  $C_c/C_p$  ratio than TEMPS, approximately 6.3 as opposed to a predicted 4.5 for TEMPS. This is one reason for the longer decay constant  $1/\alpha$ ; it also shows the battery approximation to be quite accurate when  $C_c \gg C_p$ .

#### G.7 SINGLE-SHEET SOLID-DIELECTRIC TESTS

The test module is shown in Figure 183a. A single disk of standard grade, nonoriented polypropylene extruded to a thickness of 0.020 inch and manufactured by General Tire and Rubber Company was tried first (Figure 183b). The module was assembled under water into the configuration shown in Figure 177 and placed into the test apparatus of Figure 179.

After verifying the module capacitance (approximately 3.3 nF), voltage pulses of increasing magnitude were placed across it until a failure occurred. Three samples were tested this way; each time, failure occurred at about 1.3 MV/cm. All failures occurred within the main body of dielectric rather than at the edges. An enlargement of a typical failure is shown in Figure 184. Actual size of the hole was approximately 1 mm x 2 mm.

After the third consecutive failure at 1.3 MV/cm, testing of single sheets was discontinued.

#### G.8 MULTI-LAYERED SOLID DIELECTRIC TESTS

Initially, multilayered tests were performed by simply replacing the solid dielectric sheet shown in Figure 183a with twenty layers of 0.001-inch, balanced biaxially oriented

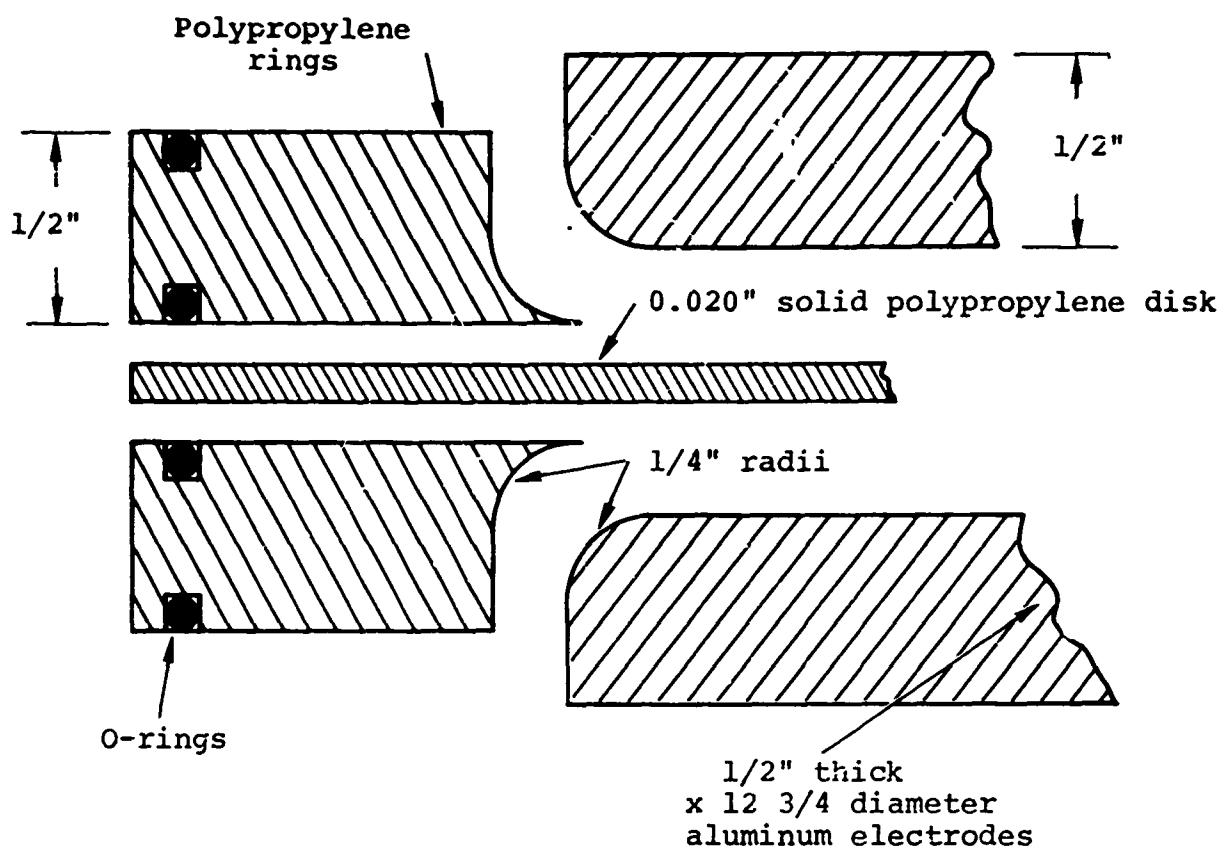


Figure 179a Single sheet solid dielectric test module exploded view of section.



Figure 183b Polypropylene ring for single sheet test.



Figure 184 Single sheet solid dielectric failure.

polypropylene film, type EK 500, manufactured by Hercules, Incorporated. The dielectric material successfully withstood 2.1 MV/cm, but further increases in stress level were hindered by an envelope flashover problem. The problem was associated with the difficulty of trimming film layers close enough to the outside edge of the envelope. Water on the gas/plastic interface was another contributing factor.

The flashover problem was corrected by redesigning the polypropylene rings as shown in Figure 185. The actual assembly parts are shown in Figure 186. The outside edges were radiused to increase the surface path length between uniform field plates. O-ring locations were moved radially inward to ensure that the edges of the polypropylene sheets did not extend beyond the outside of the rings. This modification allowed stressing the sample to the limit of the test apparatus. No failures were encountered up to a level of 2.8 MV/cm.

After maximum voltage tests, life testing at an average stress level of 2.0 MV/cm, the maximum design voltage, was begun. After 1000 shots at this stress, the module was disassembled and inspected. No failures had occurred but close inspection of the polypropylene sheets revealed a gradual degradation in the form of small dendrites on the outside sheets. Figure 187 is a photograph of these small dendrites against a black background. It appears that they form at the point where the 1/2 inch polypropylene rings shown in Figure 186 mate with the top and bottom sheets of the stack of 0.001-inch polypropylene disks and grow radially outward for around 5 to 7 mm. The cause of these dendrites apparently stems from the prototype edge-grading geometry. A detailed discussion of this will be postponed until data from other prototype tests and from electrostatic field plots are available.

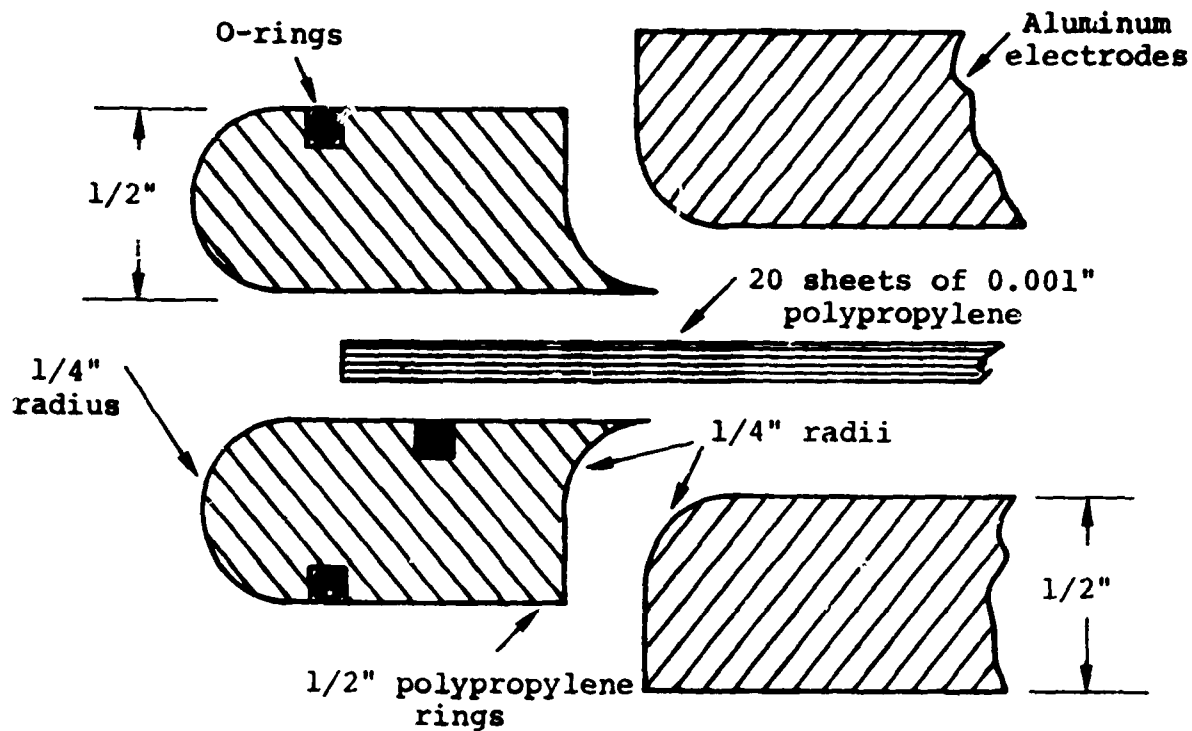


Figure 185a Multi-layer solid dielectric test module type "A"-  
exploded section view.

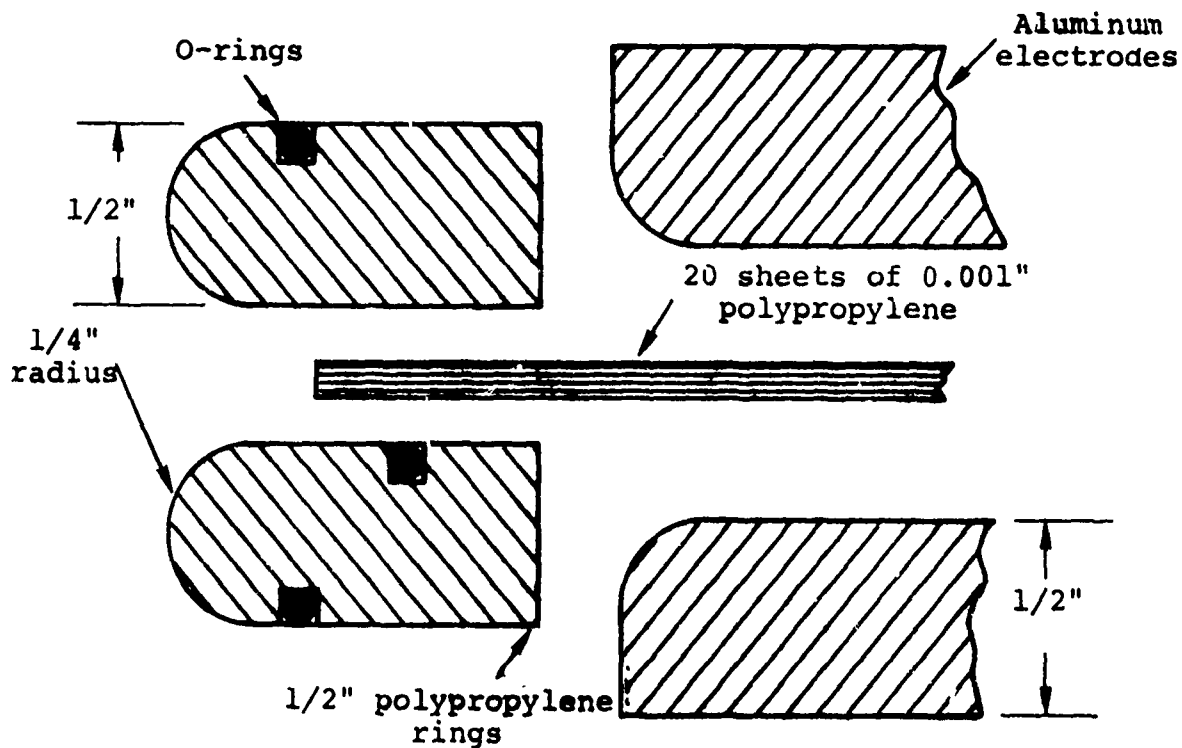


Figure 185b Multi-layer solid dielectric test module type "B"-  
exploded section view.

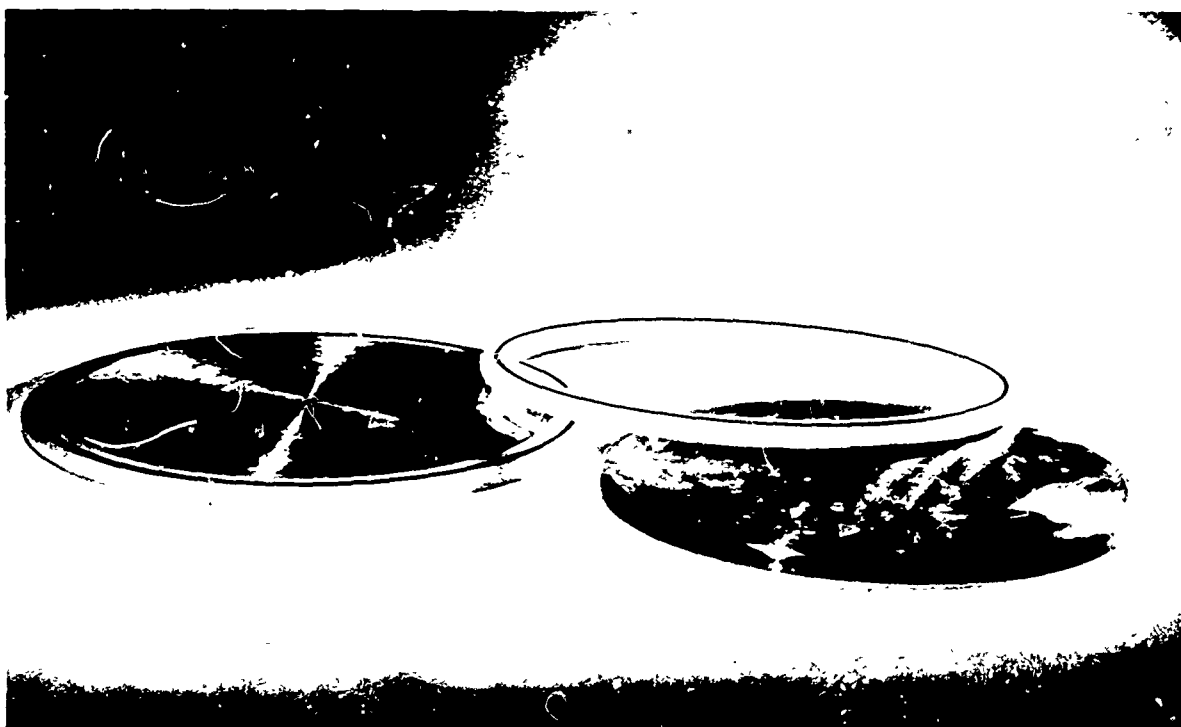


Figure 186 Polypropylene rings and aluminum electrodes.

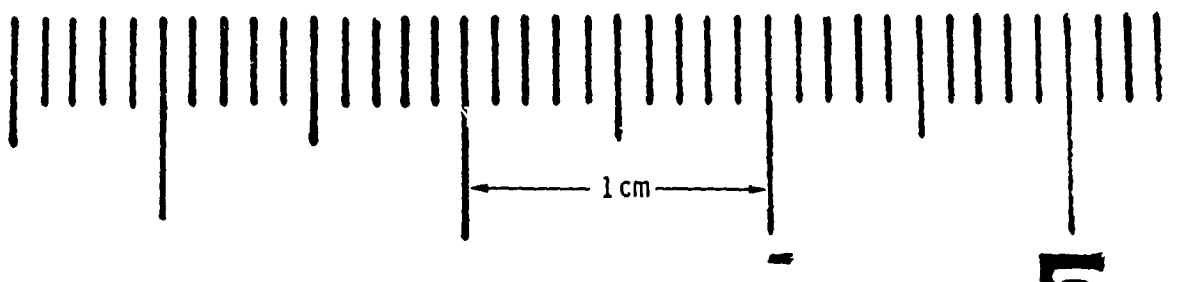


Figure 187 Life test dendriting of polypropylene (20 sheets;  
0.001 in each).



Next, the polypropylene ring geometry was changed to that shown in Figure 185b. The configuration of Figure 185b (Type B) offers production advantages over that of 185a (Type A); so its ability to perform as well as Type A would be an advantage to TEMPS. The Type A tests were repeated and the results were almost identical. No failures occurred in over 1000 shots but similar surface degradation was observed.

#### G.9 LIQUID DIELECTRIC TESTS

Tests were effected of a single-module, liquid-dielectric capacitor using a water medium. The test module is shown in Figure 188. As stated in the proposal (Reference 1), a larger electrode spacing must be used with liquid dielectric as opposed to solids to compensate for their lower breakdown strengths. The spacing of 1 cm was chosen for water by referring to available data regarding its pulse breakdown characteristics (Reference G-2). The envelope diameter and, hence, electrode surface area were predicated upon availability of parts from a previous test. Brass was chosen as the electrode material because of its compatibility with de-ionized water, and de-ionized but un-degassed water was procured for assembly of the test apparatus.

Initially, the evolution of dissolved gases presented a problem. Breakdowns occurred at 100 kV/cm or less and quite often visible bubbles would collect on electrode surfaces of the assembly before it could be put into the test fixture. The problem was corrected by installing a degassing system. This being accomplished, a level of 138 kV/cm was reached without failure. Afterward, a short life test was performed to check for degradation effects; none were observed.

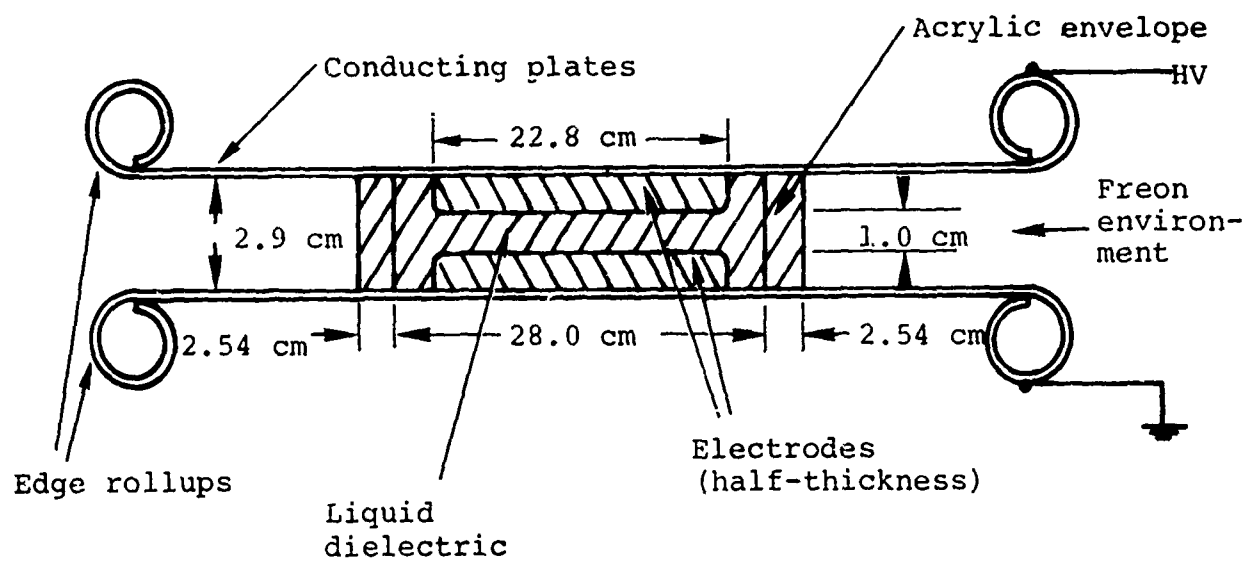


Figure 188 Single module liquid dielectric test apparatus.

## G.10 CONCLUSIONS

Results of the single-sheet solid-dielectric tests clearly indicate the design to be unacceptable from a breakdown standpoint. A better grade of polypropylene could conceivably improve the reliability of the design somewhat but all data available at this time indicate that maximum strength can only be realized with thin films such as the balanced, oriented polypropylene used in these tests.

The fact that balanced, biaxially oriented polypropylene film was used unquestionably contributed to the success of the multilayered solid dielectric design over the single sheet design. Balanced orientation results when the film is distended equally along two mutually perpendicular axes (machine and transverse directions) during the manufacturing process. The orientation tends to line up crystalline and amorphous regions<sup>\*</sup> within the polymer. Although its primary purpose is to optimize mechanical properties of the film<sup>\*\*</sup>, it has been shown to improve electrical breakdown characteristics as well. The manufacturer, Hercules, Inc., has verified this fact by comparing the breakdown characteristic of oriented versus nonoriented films under both ac and dc conditions. The results show the oriented films are intrinsically stronger.

---

<sup>\*</sup> EK-500 polypropylene film has a molecular structure consisting of approximately 94 percent isotactic polymer, 55 to 60 percent of which is crystalline, and 6 percent atactic polymer, all of which is amorphous (noncrystalline).

<sup>\*\*</sup> For example, the low temperature usefulness is dropped from 0°C for nonoriented polypropylene to -60°C for balanced polypropylene.

Liquid dielectric capacitor test results indicate that such a design remains a viable alternative but, as pointed out in Reference 1, presents certain structural disadvantages. The tests also indicate that, to obtain a safety margin comparable to a stacked film solid dielectric, a design more conservative than the one tested must be used. This would further complicate structural problems by increasing the size and weight of the assemblies.

In summary, single module test results indicate that a solid-dielectric, liquid-graded design using thin, stacked sheets of balanced, biaxially oriented polypropylene or perhaps capacitor grade Mylar should be pursued as a primary alternative with a liquid dielectric design as the backup choice. Testing will continue in order to optimize grading geometry and solve such problems as the surface degradation observed in single module testing.

## REFERENCES TO APPENDIX G

- G.1. George Frazier, Volume Effect for Solid Peaking Capacitor Designs, TEMPS Design Note No. 7, October 1971.
- G.2. J. C. Martin, Comparison of Breakdown Voltages for Various Liquids Under One Set of Conditions, Report SSWA/SCM/1105/8, AWRE, Alderwaston, U.K.